Design and Fabrication of Single-mode Tunable Lasers for Regrowth-free Monolithically Integrated Photonic Circuits

Ludovic Caro

Thesis submitted for the degree of Doctor of Philosophy

NATIONAL UNIVERSITY OF IRELAND, CORK

SCHOOL OF SCIENCE

DEPARTMENT OF PHYSICS

March 2019

Head of Department: Prof. John McInerney

Supervisors: Prof. Frank Peters

Contents

List of Figures . . . iii
Abstract . . . xi
Acknowledgements . . . xii
List of Publications . . . xiii
List of Acronyms . . . xvi

1 Lasers in Photonic Integrated Circuits 1
1.1 Motivation . . . 1
1.2 Thesis outline . . . 2

2 Optical communications 3
2.1 Situation overview . . . 3
2.1.1 A connected world . . . 3
2.2 Satisfying increasing bandwidth requirements . . . 5
2.2.1 Increasing the data density . . . 8
2.2.2 Exploring additional regions of the spectrum . . . 9
2.2.3 Selecting the right light source . . . 9
2.3 Providing more and more communication devices . . . 10

3 Semiconductor lasers: design, devices, processes 13
3.1 Mathematical tools for the study of photonic devices . . . 13
3.2 Semiconductor laser diodes . . . 16
3.3 Overview of the solutions currently in use . . . 17
3.3.1 Why single-mode, tunable lasers are needed . . . 17
3.3.2 The Fabry-Perot laser . . . 18
3.3.3 Single mode lasers . . . 19
3.3.4 Advantages and limitations of the current solutions . . . 27
3.4 Towards a large-scale production of photonic circuits . . . 28
3.5 Fabrication techniques for photonic integrated circuits . . . 29
3.6 Typical DC fabrication process . . . 32
3.7 Typical characterisation process . . . 48
3.7.1 Characterisation setup . . . 48
3.7.2 Device characterisation . . . 50
3.8 Summary of the proposed methodology . . . 55

4 First generation of lasers 57
4.1 Design and purpose . . . 57
4.2 The multimode interference coupler . . . 60
4.3 Device simulation . . . 62
4.4 Device characterisation . . . 67

5 Second generation of lasers 74
5.1 Design and purpose . . . 74
5.2 Device characterisation . . . 76

6 Third generation of lasers **80**
6.1 Design and purpose 80
6.2 Device simulation 81
6.3 Device characterisation 83
6.3.1 2-by-2 laser characterisation 83
6.3.2 1-by-3 laser characterisation 86

7 Fourth generation of lasers **92**
7.1 Design and purpose 92
7.2 Device simulation 93
7.3 Characterisation results 95

8 Fifth generation of lasers **100**
8.1 Design and purpose 100
8.2 Difficulties during fabrication procedure 103
8.3 Characterisation results 108

9 Sixth generation of lasers **113**
9.1 Design and purpose 113
9.2 Further improvements to the fabrication procedure 115
9.3 Characterisation results 119

10 Conclusion and further works **124**
10.1 Summary of the work done 124
10.1.1 Simple fabrication methods 124
10.1.2 Improved fabrication practices 125
10.1.3 Single-mode tunable facetless lasers 126
10.1.4 Integrated EMLs and comb sources 127
10.2 Proposals for further development 128

A Epitaxial structure of the laser material used for this work **136**
A.1 section 136

List of Figures

2.1 Cisco estimation and forecast of the traffic mix by type of device showing a growth of the total internet traffic, powered notably by the smartphones 4
2.2 Schematic map of the submarine communication cables 5
2.3 Cisco estimation and forecast of the mix of connected devices with a growth powered notably by the M2M communication development - numbers in parentheses indicate the 2016 and 2021 shares 6
2.4 Cisco estimation and forecast of the annual internet traffic - although on short term the evolution appears linear, in longer term it follows an exponential trend 7

3.1 Simulated Fabry-Perot cavity reflection profile - the maxima correspond to the wavelengths that can be sustained in the cavity . 19
3.2 Simulated reflection profile of a DBR mirror including 1000 grating periods designed for a reflection at 1550nm, with refractive indices of 3.52 and 3.515 21
3.3 Simulated SG-DBR mirror reflection profile for 30 sampling periods, each containing 40 grating periods with indices 3.52 and 3.515 23
3.4 SEM picture of a slotted ridge - the T shape helps pushing away imperfections at the angles, for a flat interface 25
3.5 Microscope image of lithography resolution verification structures after photoresist development - the numbers correspond to the size of the nearby features in μm 31
3.6 SEM image of a ridge after semiconductor etch - the chamfer shape at the corners (it should be a right angle) justifies the T shape for the slots to ensure a flat interface 32
3.7 Schematic of the alignment marks used throughout the process 33
3.8 Microscope image of waveguide patterns etched in silicon oxide 34
3.9 Wafer profile schematic after nitride deposition - depth indications refer to the target etch depth 34
3.10 Microscope image of nitride openings around pits on ridges . . 35
3.11 Wafer profile schematic after deep etch 35
3.12 Wafer profile schematic after nitride removal and semiconductor etch 35
3.13 Microscope image of a future 1-by-3 MMI-based modulated laser after the nitride removal and semiconductor etch 36
3.14 Microscope image of a future looped 1-by-3 MMI-based laser showing the oxide opening on top of the ridges 37
3.15 Microscope image of undercut photoresist on contact pads - the undercut is visible as the double line on the edges of the opening 38
3.16 Microscope image of a sample after metal evaporation 39
3.17 Schematic of the metal lift-off resist layout 40

3.18 Microscope image of a sample after metal lift-off 40
3.19 SEM picture of an undercut reflective feature showing the different selectivity of the etchant between the different layers 42
3.20 EPD reflection graph showing different epitaxial regions, with indications of points of interest for the operator 43
3.21 SEM picture of a ridge damaged by excessive current density . . 45
3.22 SEM picture of a ridge showing metal redeposition after combined oxide and metal etches 46
3.23 SEM picture of a ridge with a smooth side wall and no metal redeposition in the case of a thinner metal layer 47
3.24 Characterisation setup including a central chuck, contact probes, microscope camera, current sources and a power meter 49
3.25 Photograph of a chip on the chuck, with probes and a lensed fibre. €0.01 coin for scale. 49
3.26 Detail of a device under test with probes and a coupling fibre . 50
3.27 Example of laser emission spectrum graph 52
3.28 Graph of the FFT analysis of a laser emission spectrum, showing peaks at lengths corresponding to the resonating cavities present in the device 53
3.29 Superimposed laser emission spectra from a single device for different combinations of injected currents 53
3.30 ESA data used to determine the laser linewidth - the linewidth corresponds to half the width of the curve at 3dB below maximum 54

4.1 One-reflector structure schematic for validating the MMI dimensions - the ridges and MMI sections are in blue, the metal in orange and the deeply etched sections in red 58
4.2 Two-reflectors structure schematic for validating the MIRs to create a cavity 58
4.3 Three-reflectors structure schematic for an early attempt at a dual cavity MMI laser 59
4.4 Device schematics for alternative contact configurations to facilitate the powering of the laser 59
4.5 Simulated signal propagation through a 696μm long and 14 μm wide MMI coupler at 1550nm illustrating the self-imaging properties of an MMI, and points of interest along the path. 60
4.6 Simulated signal propagation through a 696μm by 14.28μm MMI coupler at 1550nm illustrating the sensitivity of MMIs to width variation. 61
4.7 Simulated signal propagation through a 709.9μm by 14μm MMI coupler at 1550nm illustrating the robustness of MMIs to length variation. 62
4.8 Simulated signal propagation through a 696μm by 14.14μm MMI coupler at 1550nm for realistic fabrication uncertainty. 63
4.9 Schematic structure studied consisting in a 2x2 coupler and four arms, arm 3 being the input port in this study 63

4.10 SMM-simulated reflection spectrum for the first generation device with 3 reflectors and a cleaved facet showing an expected mode spacing of 1.5nm and a super-mode spacing of 3.5nm . . 67
4.11 Microscope image of fabricated and cleaved devices from the first generation 67
4.12 Emission spectrum below threshold of the 1-reflector structure with shallow isolation slots 68
4.13 Fourier analysis of the emission spectrum of the 1-reflector structure with shallow isolation slots - the low peaks at 500μm show the limited impact of shallow isolation slots on the reflection profile 69
4.14 Fourier analysis of the emission spectrum of the 1-reflector structure with deep isolation slots - the larger peaks at 500μm show the increased effect of deeply etched slots on the reflection profile 69
4.15 Emission spectrum of the 2-reflectors structure with shallow isolation slots showing single-mode operation and the envelope typical of a dual-cavity system 70
4.16 Fourier analysis of the emission spectrum of the structure with two reflectors and shallow isolation slots - the peaks at 1.6mm and 1.7mm match the lengths of the different cavities defined by the cleaved facet and MIRs and the 0.1mm peak corresponds to the length difference between the two cavities, with no visible effect of the slots on the spectrum 70
4.17 Superimposed emission spectra showing both Vernier-like and fine tuning achieved for the 2-reflectors structure with shallow isolation slots 70
4.18 Fourier analysis of the emission spectrum of the structure with two reflectors and deep isolation slots - although the 0.1, 1.6 and 1.7mm peaks match the cavity dimensions, the 0.6mm peak suggests the deep slots cause strong interference 71
4.19 Superimposed emission spectra showing the fine tuning of the 3-reflectors structure with shallow isolation slots 71
4.20 Emission spectrum for the 3-reflectors structure with deep isolation slots 71
4.21 Emission spectrum for the three reflective sections electrically connected - the lack of flexibility for the different sections makes it difficult to achieve single-mode lasing 72
4.22 Emission spectrum for the two right hand side sections electrically connected - the lack of flexibility for the different sections makes it difficult to achieve single-mode lasing 72

5.1 Schematic of a second generation 2x2 MMI laser - the output is angled relative to the cleave place to avoid reflections, so that the cavities are defined only by the MIRs 75
5.2 SMM-simulated second generation 2x2 MMI laser reflection profile 75

5.3 Schematic of a second generation 2x2 MMI slotted laser with $\Delta L = 25\mu$m and $k = 1$ - the slot is placed on the output arm to increase feedback and to modify the reflection profile 76
5.4 SMM-simulated second generation 2x2 MMI slotted laser reflection spectrum illustrating how the addition of the slot modifies the envelope shape 76
5.5 Emission spectrum and corresponding Fourier analysis of an unsuccessful Second Generation MMI laser where no lasing was achieved but dual-cavity behavior can be noticed with the supermode envelope and the two peaks in the Fourier analysis 77
5.6 SEM image of a ridge showing a porous passivation layer, compromising the electrical isolation 78
5.7 Superimposed emission spectra of a 2x2 MMI/MIR laser for different configurations of injected currents showing limited tuning capability for this laser 79
5.8 Superimposed emission spectrum and SMM-simulated reflection profile showing good agreement for the super-mode spacing - the simulated profile was vertically offset for clarity 79

6.1 Third generation 1x3 MMI laser schematic - the 1x3 design reduces the power that is lost for feedback and in this design, a deep slot is used to increase feedback and MEFs are used as an alternative to MIRs to assess their performance as a reflector . . 81
6.2 BPM simulation of the Splitter operation of the 3x3 MMI coupler 82
6.3 1x3MMI laser schematic with the names of the transfer functions used in the calculations 82
6.4 1x3 MMI laser SMM-simulated reflection spectrum showing a 3nm super-mode spacing 83
6.5 2x2 MMI/MEF devices under test 84
6.6 Superimposed emission spectra of a 2x2 MMI/MEF laser showing a 24nm discrete tuning range and SMSR levels above 25dB . . 84
6.7 Superimposed emission spectra of a 2x2 MMI/MEF laser showing a 1.5nm continuous tuning range 85
6.8 Emission spectrum of a 2x2 MMI/MEF laser (blue) and simulated reflection profile (red) showing good agreement between the simulation and measured data 86
6.9 Self-interference profile of a 2x2 MMI/MEF laser showing a full width at half maximum of 1.2MHz, for a 600kHz linewidth, obtained using a self-heterodyne technique 86
6.10 1x3 MMI/MEF devices on the characterisation setup 87
6.11 Emission spectrum of a 1x3 MMI/MEF laser showing single mode behavior with a 30dB SMSR and a super-mode spacing of approximately 3nm, matching the simulated reflection profile . . 87

6.12 Fourier analysis of a 1x3 MMI/MEF laser emission spectrum, showing two main cavity lengths and additional parasitic reflections, suggesting imperfect MMI dimensions but satisfying operation of the MEFs 88
6.13 Superimposed emission spectra of a 1x3 MMI/MEF laser showing a 47nm discrete tuning range and SMSR levels above 30dB . . 89
6.14 Superimposed emission spectra of a 1x3 MMI/MEF laser showing continuous tuning over a 3nm range 90
6.15 Self-interference profile of a 1x3 MMI/MEF laser showing a full width at half maximum of 1.6MHz, for a 800kHz linewidth . . 90

7.1 SEM image of a deeply etched pit in a waveguide 93
7.2 Fourth generation 2x2 "Gamma" laser schematic 93
7.3 Fourth generation 1x3 "Phi" laser schematic 94
7.4 Gamma laser SMM-simulated reflection profile predicting an approximately 3nm super mode spacing 95
7.5 Phi laser SMM-simulated reflection profile predicting an approximately 3nm super mode spacing 95
7.6 Microscope image of a fabricated Gamma laser 96
7.7 Emission spectrum of a Gamma laser showing dual-cavity behavior but no evidence of lasing 96
7.8 Microscope image of a fabricated Phi laser 97
7.9 Superimposed emission spectra of a Phi laser showing a 36nm discrete tuning range and SMSR levels up to 30dB 97
7.10 Fourier analysis of a Phi laser emission spectrum showing two main cavities but no evidence of an effect from the pit positioned at 25μm 98
7.11 Superimposed emission spectra showing thermal tuning of a Phi laser over a 3nm range 98
7.12 Superimposed emission spectrum of a Phi laser and corresponding SMM-simulated reflection profile showing a match in terms of super-mode spacing 99

8.1 Schematic of the Gamma geometry with a variant of the curve optimised to reduce bend loss 100
8.2 Schematic of the Phi geometry with a variant of the curve optimised to reduce bend loss 101
8.3 Schematic of a proposed intra-cavity reflector of width 1.35μm 102
8.4 Schematic of a 1x3 MMI EML 102
8.5 I-V scan of a waveguide section showing high resistivity and failure at 36mA while it should have sustained at least 50mA before failure 103
8.6 Microscope image of a waveguide showing damage at specific points along the section suggesting a local high current density heating up the device to the point of damaging it 105

8.7 Microscope image of a chip with blistered oxide - those cracks in the passivation layer can compromise the isolation and cause leaks, reducing the current reaching the ridge 105
8.8 SEM image of a processed chip with shadowing of the metal along the wall and damage to the ridge after an attempt at probing it directly. One can also observe that the metal layer does not appear as smooth and thick as would be expected, suggesting a general malfunction of the metal evaporator 107
8.9 SEM image of a metal-first process test chip showing slight wall roughness and negligible metal redeposition 108
8.10 FFT analysis of a new Phi laser emission showing one main cavity and residual additional reflections 109
8.11 Fourier analysis of a Fabry-Perot laser with a slot showing the full cavity length and the two subcavities 110
8.12 Fourier analysis of a Fabry-Perot laser with a 1.1μm T-bar showing the main cavity and no reflection from the T-bar 110
8.13 Fourier analysis of a Fabry-Perot laser with a 1.35μm T-bar showing the main cavity and no reflection from the T-bar 110
8.14 SEM image of a "T-Bar" showing an offset of the oxide opening and a shadowing effect caused by the ridge during metal deposition, compromising electrical connection 111
8.15 Superimposed laser emission spectra of a 1x3 MMI EML for different EAM biases showing an extinction of 10dB at -1.5V bias, relatively to the 0V bias 112

9.1 Schematic of a 1x3 MMI laser integrated with an EAM section - the multiple circular top-side N contact are here to accommodate high-speed probes coming from different directions to facilitate the probing of the pads 114
9.2 Schematic of a 1x3 MMI laser integrated with a comb generation section 114
9.3 Schematic of a 1x3 MMI laser - MCP variant 115
9.4 Schematic of a 1x3 MMI EML - MCP variant 115
9.5 Oxide opening alignment verification structure schematic for visual inspection after lithography 116
9.6 Microscope image of oxide open alignment verification structures after complete fabrication, here showing satisfying alignment in both X and Y directions 117
9.7 SEM image of a ridge with shallow and deep etch depths showing smooth side walls, no noticeable metal redeposition, and partial etch of the metal cap on the ridge in the deeply etched area . . 118
9.8 EPD reflection profile of the sample over time for a semiconductor etch past the quantum wells, obtained by recording the reflected power of a laser aimed at the surface of the sample . . . 120
9.9 Emission spectra showing SMSR levels of up to 35dB and 51nm tuning range for a 1x3 MMI laser with pits - MCP variant 120

9.10 Detail of a 4GHz comb generated with a 1x3 MMI laser integrated with a gain-switched comb generation section 121
9.11 Emission spectra of a 4GHz comb source integrated with a 1x3 MMI tunable laser showing a 28nm discrete tuning range and SMSR levels from 25dB to above 30dB 122
9.12 Laser emission spectra of a 1x3 MMI EML with pits, for different EAM biases showing a static absorption of up to 19.5dB at -2.5V bias 122
9.13 Laser emission spectra of a 1x3 MMI EML with pits for different wavelengths and EAM biases 123

10.1 Microscope image of a "Phi" laser 126
10.2 Microscope image of a 1x3 MMI Laser 126
10.3 Microscope image of a 1x3 MMI Laser integrated with an EML section 127
10.4 Microscope image of a 1x3 MMI laser integrated with a comb generation section 127
10.5 Schematic of a monolithically integrated regrowth-free photonic circuit including a tunable laser source, a comb generation section, and ring filters for 4 channels that are then equalised, modulated and recombined 128

A.1 Epitaxial structure of the laser material used for this work . . . 136

I, Ludovic Caro, certify that this thesis is my own work and has not been submitted for another degree at University College Cork or elsewhere.

Ludovic Caro

Abstract

In this communication age, the bandwidth requirements are increasing exponentially with the development of more and more data-intensive services, from high-definition video streaming and cloud-based computing to the Internet of Things and machine-to-machine communication. This rapid expansion is powered by a rapidly growing fibre-based optical communication network. This growth, both in geographical extension and density of terminals, results in a large-scale need for the photonic components that are at the core of the optical communication network. In order to satisfy the demand, photonics industries need to increase their production capabilities and adopt more efficient fabrication processes. Streamlining the fabrication implies the removal of slow or costly processes. In the case of the photonics fabrication, epitaxial regrowth and advanced lithography steps are slow and expensive parts of the fabrication, and are one of the first targets for streamlining the process. In addition to reducing the cost of the fabrication itself, the integrated electronics approach can be a source of inspiration with the monolithic integration of multiple photonic components fabricated at the same time to create highly complex circuits while limiting the fabrication complexity.

Focusing on a component at the core of photonic circuits: the tunable single-mode laser, this work is a contribution to the development of components that can be fabricated without requiring any regrowth or advanced lithography. Based on multi-cavity geometri s enabled by multimode interference couplers and on a cleave-free approach to facilitate integration, a portfolio of tunable lasers is presented, showing tuning ranges of up to 51nm in the C and L optical windows, and side-mode suppression ratio levels of up to 35dB. Inspired by integrated electronics, proofs of concept for monolithically integrated electro-absorption modulated lasers and comb sources are presented, showing up to 19.5dB static absorption ratios for the modulated lasers, and a 4GHz optical comb tuned over a 28nm discrete tuning range. These results validate the proposed lasers as suitable candidates for the development of monolithically integrated photonic circuits where the fabrication complexity was kept minimal, making them attractive devices for the large-scale, streamlined production processes necessary to meet the increasing need for photonic components.

Acknowledgements

I would like to thank my supervisor Frank Peters for giving me the opportunity to discover the field of photonics. For his support over the course of this work, I am grateful.

I would also like to thank Niall Kelly who taught me everything I know on semiconductor processing, for his support and his patience. I would like to give a special mention to Mohamad Dernaika and Francesco Azzarello, for their friendship and their support all along the way, whether it was in the cleanroom or facing a pack of sleepy first-year students.

I am grateful to all the IPG team and the Tyndall community for their friendship over the years.

I would also like to thank my friends in Ireland and beyond for their patience and support, and to mention the SRSC team for the fantastic Tuesdays, Damien for teaching me how to count to seven, and Jim for the amazing playlists. I am particularly grateful to Nicolas Braneyre, science teacher, who once set a car battery on fire and by doing so, gave me the passion for science.

Thanks a million to my family for supporting me and giving me the strength to accomplish all this.

List of Publications

Journal Articles

1. **L. Caro**, N. P. Kelly, M. Dernaika, M. Shayesteh, P. E. Morrissey, J. K. Alexander and F. H. Peters, "A Facetless Regrowth-free Single Mode Laser based on MMI Couplers," *Optics & Laser Technology*, vol. 94, pp. 159 - 164, 2017.

2. **L. Caro**, M. Dernaika, N. P. Kelly, P. E. Morrissey, J. K. Alexander and F. H. Peters, "An Integration-Friendly Regrowth-Free Tunable Laser," *IEEE Photonics Technology Letters*, vol. 30, pp. 270 - 272, 2018.

3. M. Dernaika, **L. Caro**, N. P. Kelly, J. K. Alexander, F. Dubois, P. E. Morrissey and F. H. Peters, "Deeply Etched Inner Cavity Pit Reflector," *IEEE Photonics Journal*, vol. 9, no. 1, pp. 1 - 8, 2017.

4. M. Dernaika, **L. Caro**, N. P. Kelly and F. H. Peters, "Single Facet Semiconductor Laser with Deep Etched V-notch Reflectors Integrated with an Active Multimode Interference Reflector," *Journal of Modern Optics*, vol. 64, no. 19, pp. 1941 - 1946, 2017.

5. N. P. Kelly, **L. Caro**, M. Dernaika and F. H. Peters, "Regrowth-free Integration of Injection Locked Slotted Laser with an Electroabsorption Modulator," *Optics Express*, vol. 25, no. 4, pp. 4054 - 4060, 2017.

6. J. K. Alexander, P. E. Morrissey, **L. Caro**, M. Dernaika, N. P. Kelly and F. H. Peters, "On-chip Investigation of Phase Noise in Monolithically Integrated Gain-switched Lasers," *IEEE Photonics Technology Letters*, vol. 29, no. 9, pp. 731 - 734, 2017.

7. M. Dernaika, N. P. Kelly, **L. Caro**, K. Shortiss and F. H. Peters, "Regrowth-free Single-mode Semiconductor Laser Suitable for Monolithic Integration based on Pits Mirror," *Optical Engineering*, vol. 65, no. 8, 2017.

8. N. P. Kelly, M. Dernaika, **L. Caro**, P. E. Morrissey, A. H. Perrott, J. K. Alexander and F. H. Peters, "Regrowth-free Single Mode Laser based on Dual Port Multimode Interference Reflector," *IEEE Photonics Technology Letters*, vol. 29, no. 3, pp. 279 - 282, 2017.

9. N. P. Kelly, M. Dernaika, **L. Caro**, P. E. Morrissey and F. H. Peters, "Monolithic Integration of Photonic Devices for use in a Regrowth-free CoWDM

Transmitter," *IEEE Photonics Technology Letters*, vol. 29, no. 12, pp. 941 - 944, 2017.

10. P. E. Morrissey, N. Kelly, M. Dernaika, **L. Caro**, H. Yang and F. H. Peters, "Coupled Cavity Single-mode Laser Based on Regrowth-free Integrated MMI Reflectors," *IEEE Photonics Technology Letters*, vol. 28, no. 12, pp. 1313 - 1316, 2016.

Conference Proceedings

1. **L. Caro**, M. Dernaika, N. P. Kelly, P. Morrissey, H. Yang and F. Peters, "A Facetless Regrowth-free Single Mode Laser Based on Multimode Interference Couplers and Reflectors", *Photon16*, Leeds, United Kingdom, 2016.
2. **L. Caro**, N. P. Kelly, M. Dernaika, J. K. Alexander, P. E. Morrissey and F. H. Peters, "Widely Tunable Facetless Regrowth-free Semiconductor Laser", *European Conference on Lasers and Electro-Optics*, Munich, Germany, 2017.
3. **L. Caro**, M. Dernaika and F. H. Peters, "An MMI-based Tunable Laser for Integrated Photonic Circuits", *Conference on Lasers and Electro-Optics*, San Jose, California, United States of America, 2018. W, 2017.
4. A. H. Perrott, **L. Caro**, M. Dernaika, N. P. Kelly, P. E. Morrissey and F. H. Peters, "Mutual Injection Locking of Lasers in a Photonic Integrated Circuit," *European Conference on Integrated Optics 2017*, Eindhoven, The Netherlands, 2017.
5. M. Dernaika, **L. Caro**, H. Yang and F. H. Peters, "A Regrowth-free, Facetless Multiple Quantum Wells AlInGaAs Semiconductor Laser Suitable for Photonic Integration," *Advanced Photonics Congress*, Zurich, Switzerland, 2018.
6. J. K. Alexander, P. E. Morrissey, **L. Caro**, M. Dernaika, N. P. Kelly and F. H. Peters, "Integratable Optical Comb Source for Coherent Communications Systems," *Conference on Lasers and Electro-Optics*, San Jose, California, United States of America, 2017.
7. S. P. Duggan, N. P. Kelly, **L. Caro**, M. Dernaika, M. Shayesteh, J. K. Alexander, H. Yang, P. E. Morrissey, A. Gocalinska, K. K. Thomas, E. Pelucchi and F. H. Peters, "Development of Inverted P-Substrate InP/AlGaInAs Lasers for Vertical Integration with Multiple Passive or Active Intrinsic Regions,"

European Conference on Integrated Optics 2017, Eindhoven, The Netherlands, 2017.

8. N. P. Kelly, M. Dernaika, **L. Caro** and F. H. Peters, "Monolithic CoWDM Transmitter Via Integration of Injection Locked Slotted Laser With Electro-absorption Modulator", *European Conference on Lasers and Electro-Optics 2017*, Munich, Germany, 2017.
9. K. Shortiss, M. Dernaika, **L. Caro**, M. Seifikar and F. H. Peters, "Inverse Scattering Method Design of Regrowth-Free Single-mode Semiconductor Laser for Monolithic Integration," *Advanced Photonics Congress*, Zurich, Switzerland, 2018.
10. M. Dernaika, N. P. Kelly, P. E. Morrissey, **L. Caro**, H. Yang and F. H. Peters, "Single Mode Semiconductor Lasers Based on Offset Waveguides", *Photon16*, Leeds, United Kingdom, 2016.
11. A. Perrott, P. Morrissey, F. Dubois, M. Dernaika, **L. Caro**, N. Kelly and F. H. Peters, "Injection Locking Behaviour of Mutually Coupled Slotted Fabry-Perot Lasers Integrated onto a Single Growth Monolithic Photonic Integrated Circuit", *Photon16*, Leeds, United Kingdom, 2016.

List of Acronyms

AOFS ..... Acoutso-Optical Frequency Shifter

AR ..... Anti-Reflective (coating)

BOE ..... Buffered Oxide Etchant

BPM ..... Beam Propagation Module

CAIBE ..... Chemically Assisted Ion Beam Etching

DFB ..... Distribute FeedBack

DBR ..... Distributed Bragg Reflector

EAM ..... Electro-Absorption Modulator

EF ..... Etched Facet

EML ..... Electro-absorption Modulated Laser

EPD ..... End-Point Detection (system)

ESA ..... Electrical Spectrum Analyser

FBMC ..... Filter Bank MultiCarrier

FTTH ..... Fibre-to-the-Home

FWHM ..... Full Width at Half Maximum

HR ..... High-Reflectivity

ICP ..... Inductively Coupled Plasma

IoT ..... Internet of Things

ITU ..... International Telecommunication Union

LED ..... Light Emitting Diode

LPE ..... Liquid-Phase Epitaxy

M2M ..... Machine-to-Machine

MCP ..... Multi-Contact Probe

MEF ..... Metal-coated Etched Facet

MIR ..... Multimode Interference Reflector

MMI ..... MultiMode Interference

MOCVD ..... Metal-Organic Chemical Vapor Deposition

OSA ..... Optical Spectrum Analyser

PECVD ..... Plasma-Enhanced Chemical Vapor Deposition

PIC ..... Photonic Integrated Circuit

QPSK ..... Quadratic Phase Shift Keying

RIE ..... Reactive Ion Etching

SEM ..... Scanning Electron Microscope

SFP ..... Slotted Fabry-Perot

SG-DBR ..... Sampled Grating Distributed Bragg Reflector

SMA ..... SubMiniature version A (connector)

SMM ..... Scattering Mattering Method

SMSR ..... Side-Mode Suppression Ratio

SOA ..... Semiconductor Optical Amplifier

TEC ..... Thermo-Electric Cooler

UHV ..... Ultra-High Vacuum

UV ..... Ultra-Violet

WDM ..... Wavelength Division Multiplexing

Chapter 1

Lasers in Photonic Integrated Circuits

1.1 Motivation

As humanity becomes more and more connected, to the point that the things it makes are also communicating together, the global optical communication network grows ever larger and more complex. The ever increasing bandwidth demand, and the physical expansion of the networks covering larger and larger portions of the planet, call for efficient solutions to answer our need for the numerous devices that support the communication age we are in.

Finding inspiration in the electronics where large-scale production of devices enabled the digital age, this work explores the development of industrially attractive photonic devices where fabrication time and complexity are reduced as much as possible. In the present work, the focus is on laser sources, and this thesis reports on the findings made in the development of semiconductor lasers that are compatible with the optical communication schemes, while streamlining the fabrication aspect to make them industrially attractive, cost-effective solutions.

1.2 Thesis outline

This thesis is divided in 10 chapters. After the present introductory chapter, an overview of the situation of the optical comminucation network is presented, showing how the exponential growth of digital communication raises technical problems to be overcome.

Chapter 3 is a summary of the techniques and methods used to manufacture photonic devices, along with details on the processes used in fabricating and characterising the devices designed in this work, and with the basic principles of the simulation method chosen to support the design process. It also presents the different lasers currently in use in photonic circuits, and details the constraints applied to this work in an attempt to streamline the device fabrication process.

Chapter 4 presents the first generation of devices designed in this work, aiming at validating the multimode interference coupler and the first geometry as a single mode laser source.

Chapter 5 presents the second generation of devices that aimed at validating the simulation model that was developed, and to confirm the tunability of the investigated geometries.

Chapter 6 presents the third generation of devices, where alternative reflective termination components were used, as well as a variant of the initial geometry.

Chapter 7 presents the fourth generation of devices, where alternative intra-cavity relfective features were tested, as well as looped geometries and waveguide crossings.

Chapter 8 presents the fifth generation of devices, where optimised waveguide bends were tested, along with another variant of intra-cavity reflector. It also reports on the difficulties encountered during the fabrication of the devices.

Chapter 9 presents the sixth and last generation of devices, where the most promising geometries tested so far have been adapted and integrated with additional components.

Finally, Chapter 10 presents a summary of the main points of this thesis and proposes directions to further develop this work.

Chapter 2

Optical communications

2.1 Situation overview

With the development of human intelligence and knowledge, and the need to transmit increasingly complex information, means of transferring data faster and farther have been developed. From speech and hand-written messages to the semaphore, the phone and finally the worldwide web and wireless communication, humans have become able to transmit complex data ever faster, and even beyond the limits of our own planet to reach man-made devices in the solar system and beyond. But while the few probes we sent to outer space don't require high-speed data transmission, humans here want to access more and more digital services in any place, at any time. This requires the development of a considerable infrastructure to improve access to the worldwide web and cloud-based services even from remote areas. While most devices connect wirelessly to local relays, those relays need wired connections in order to provide satisfying data transmission rates to all the users of the service. Such speeds require the use of optical fibre made from silica that guides the modulated light to the receivers.

2.1.1 A connected world

We are surrounded by connected devices. While connected refrigerators that automatically order some milk when the bottle is running low remain rare today, humans have in their pockets a device they use to communicate with each

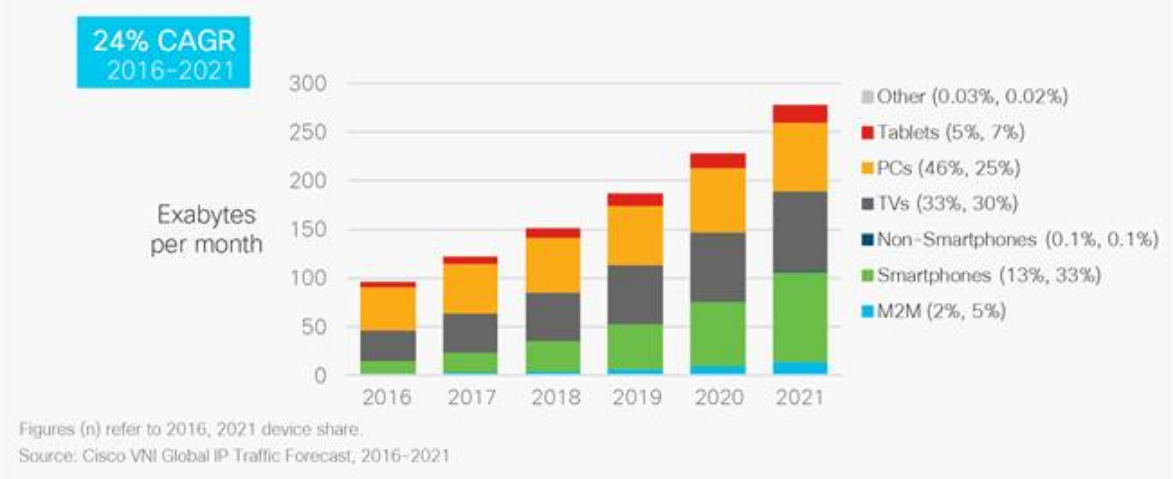

Figure 2.1: Cisco estimation and forecast of the traffic mix by type of device showing a growth of the total internet traffic, powered notably by the smartphones

other, and access data-intensive services such as high-resolution video streaming. A 2017 white-paper published by the network company Cisco [1] suggests that video represented 73% of the global traffic in 2016 and this share is expected to grow to 81% in 2021. According to the same source, in 2016 the global data traffic represented a 1.2 zettabytes (ZB, $10^{21} bytes$) annual load, or 96 exabytes (EB, $10^{18} bytes$) monthly, and is expected to reach 3.3ZB yearly (278EB monthly). As shown in Figure 2.1, one can observe that smartphones and tablets, the two main mobile connection platforms, are representing a growing share of the traffic. This information, combined with the share of data-intensive video streaming in the traffic mix, confirms the idea that we need a global networks infrastructure that will be able to support considerable data rates. One can reasonably consider that the locations of maximal traffic concentration would be the data centers where information is stored and processed, and the wireless relays covering multiple users.

Accessing data stored anywhere on the planet, from a device located anywhere on the planet, requires a worldwide infrastructure of wireless relays and emitters, and optical fibre cables to connect the relays together. In order to connect continents together, submarine optical cables were installed over the years to enable worldwide connections, as shown in Figure 2.2. It seems reasonable to consider that the nodes where the transcontinental cables are connected to the rest of the network are also subjected to high traffic concentration. But optical cables are not limited to transcontinental communications: the vast majority

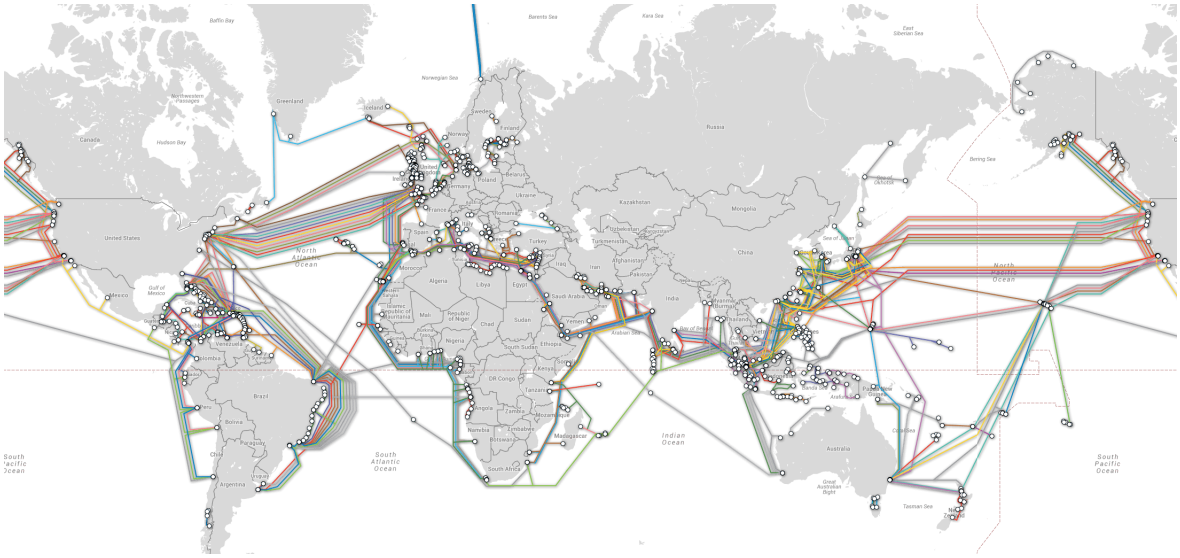

Figure 2.2: Schematic map of the submarine communication cables

of the communication infrastructure is a fibre optic skeleton, and with the development of fibre to the home (FTTH) and the worldwide effort to increase optical broadband coverage, the non-optical portion of the physical network keeps reducing. Thus, the focus on developing fibre optic technologies to support this evolution of the network.

While it is clear that human users represent a considerable share of the data traffic, another category of users cannot be neglected: the devices themselves. From the connected refrigerator that orders fresh milk when the bottle is empty, to the smartphone that uses remote speech recognition solutions to understand spoken commands, the devices themselves represent a growing share of the network users (see Figure 2.3), and machine-to-machine (M2M) communication such as the internet of things (IoT) represents a significant burden to the processing centers that provide cloud-based services. The connectivity of such nodes, as well as local connectivity from one part of a data center to another, are subject to a heavy load and require high-speed data transmission that can be achieved through optical connections.

2.2 Satisfying increasing bandwidth requirements

Fibre-optic communication can be summarised as follows: the signal, usually in an electrical form as it is generated by a digital device, is used to modulate

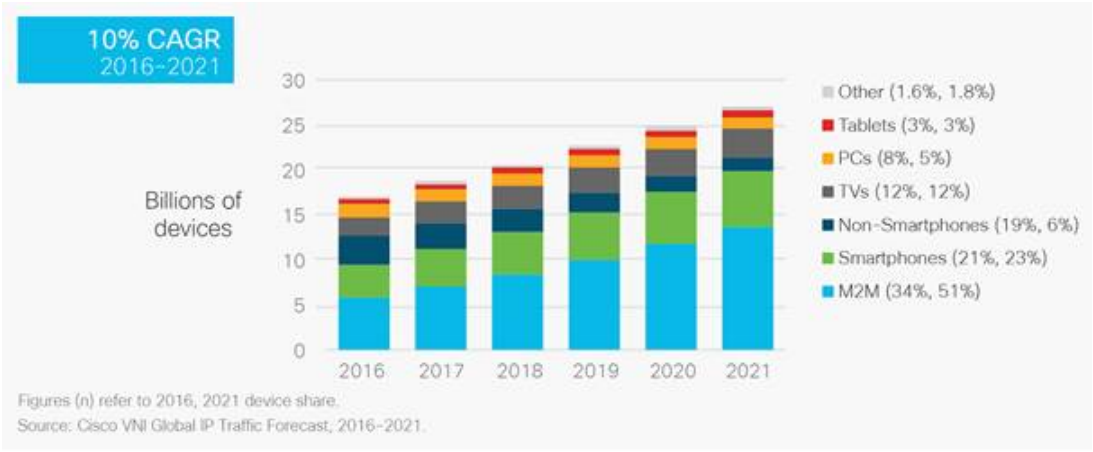

Figure 2.3: Cisco estimation and forecast of the mix of connected devices with a growth powered notably by the M2M communication development - numbers in parentheses indicate the 2016 and 2021 shares

light from a source at a determined wavelength. The modulated light is guided through the fibre network, to its destination. The light signal is then converted back into an electrical signal by the means of an adequate receiver, and can then be processed by the receiver device. From the Nyquist-Shannon theorem [2], one can derive that the rate at which the data is modulated will impose a lower limit to the bandwidth the signal will occupy. Thus, the faster the modulation rate, the larger the bandwidth.

In order to transmit the signals from multiple sources to multiple receivers while accommodating the high data rate required by the users, one can chose to increase the modulation speed of the signal. This solution tends to expand the bandwidth of the signal around the source's wavelength, but the speed cannot be infinitely increased due to technological limitations. An alternative consists in using multiple sources at different wavelengths, each of them being used to carry a part of the data in parallel with the others. By using either, or a combination of both techniques brielfy described here, one needs a portion of the optical spectrum to be dedicated to transmitting the information. However, parts of the spectrum are more favorable than others to such transmission: the presence of water in the optical fibre causes losses due to the water absorption at certain wavelengths. This is why "optical windows" have been determined, where the transmission losses are lower, making the corresponding wavelength favorable candidates for long-distance communication. Notable windows include the O band, O standing for Original, spanning from 1260nm to 1360nm where the fibre loss is low, and the C "conventional" band, from 1530nm to

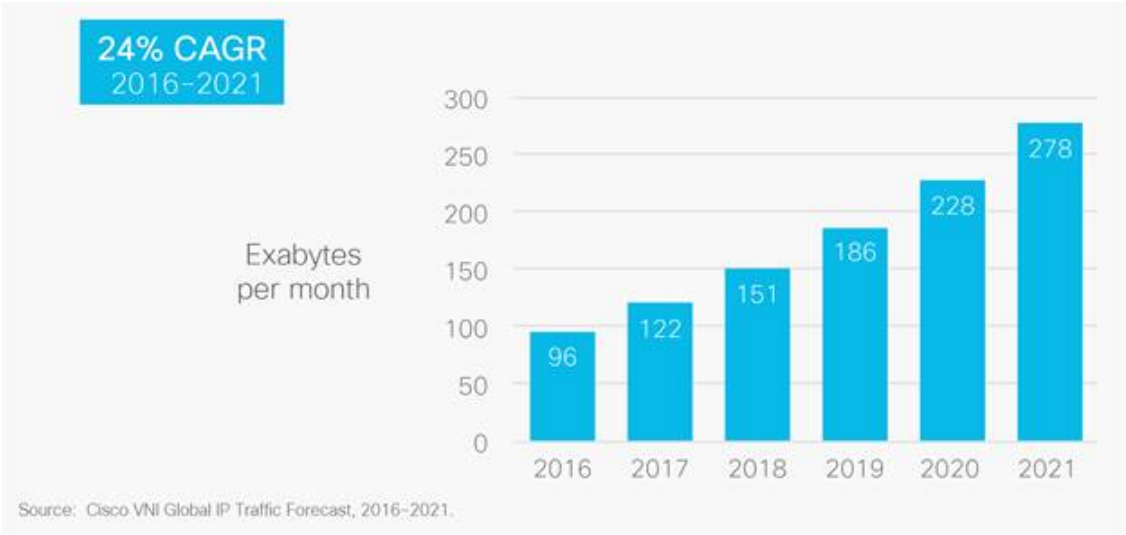

Figure 2.4: Cisco estimation and forecast of the annual internet traffic - although on short term the evolution appears linear, in longer term it follows an exponential trend

1565nm where the water absorption is lower and erbium-based solutions enable effective amplification of the optical signal. These limited windows, along with the spectral width occupied by the signal, result in a limit to the data rate a single fibre can support.

While the expected short-term growth of the traffic appears linear as illustrated in Figure 2.4 from [1], in the past it has been following an exponential trend [3] that seems to be settling down. However, according to the network systems company Cisco, the yearly traffic growth is not expected to drop below 20% in the foreseeable future, resulting in an increasingly high pressure on the existing physical infrastructure supporting the network. In order to reduce the strain on the fibre and the nodes, a solution could consist of adding more and more parallel cables to accommodate the traffic, or to upgrade the network with newer, more effective technologies. However, while the nodes are relatively easy to access, making their upgrade reasonably easy, the fibre network itself represents a length of buried and underwater cables that is practically impossible to calculate. Upgrading parts of the network represents a colossal work of digging up the fibres and replacing them with upgraded cables, or simply installing additional fibres to enable more bandwidth. As a result, the option of upgrading the existing fibre network is commonly dismissed as not worth the investment.

Thus, the development of higher-bandwidth solutions must be focused on using the existing fibre network, and only upgrading the easily accessible nodes of the

network. In order to use the same fibres to accommodate higher data rates, one needs to increase the data density in the same bandwidth, also referred to as the spectral density, or to explore additional regions of the spectrum and use them to accommodate the additional bandwidth.

2.2.1 Increasing the data density

Given a certain spectral width, there are solutions to increase the data transmission rate within the allocated space. One approach is to reduce or remove entirely the guard bands used between each carrier wavelength, and either increase the modulation rate of each carrier, or reduce the gap between adjacent carriers. This solution presents the risk that adjacent carriers, whether they are moved closer together or modulated faster, could start interfering with each other because of the spectral width caused by the signal modulation. This crosstalk is usually prevented by including sufficient gaps between adjacent carriers, at the cost of limiting the data capacity of the available spectrum.

An alternative approach consists in using complex modulation formats, in order to overcome the Nyquist-Shannon theorem: if the symbol rate generates a bandwidth around the carrier, this can be mitigated by increasing the quantity of information carried in each symbol. Starting from a simple on/off scheme that carries one bit: either 0 or 1, more complex signals can be generated. The signal amplitude can be modulated in more complex schemes than on/off, with intermediate states. For example, a 4-level amplitude modulation can carry two bits in each symbol.

Other modulation schemes can be used, by changing the phase of the signal, or combining phase and amplitude changes to generate a large variety of symbols that each contain multiple bits of information. This approach enables an increase the data density without significantly impacting the used bandwidth, but relies on the use of advanced detectors on the receiver side that can sense multiple states of the signal and determine the corresponding symbol. Another limiting factor is the noise: more complex modulation schemes reduce the difference between a symbol and another, and noise in the system can make the receiver misinterpret a noisy symbol for another one, generating a transmission error. Such errors can be digitally corrected but need to be avoided.

2.2.2 Exploring additional regions of the spectrum

Once a defined optical window is fully occupied, a solution to accommodate additional traffic is to make another part of the spectrum, available for optical communication. With the conventional C band (1530-1565nm) being saturated, the following L band of longer wavelengths (1565-1625nm) is being considered as the next window to use for optical communication. By expanding the communication spectrum to this band, additional carriers can be used to transmit more data in parallel, effectively increasing the traffic accommodated on the fibre.

It must be noted that while the L band shows low water absorption losses, it suffers from scattering losses caused by bends at microscopic and macroscopic scales [4]. The microbends and macrobends are presented in [5]. Macrobend losses are caused by the bending of the fibre that results in a part of the signal being refracted out of the fibre. The more acute the angle, the higher the loss. While such bends are rare in the case of long-range sections of fibre that are straight enough, the FTTH deployment implies lying out fibres into buildings and walls. This increases the chances of bending the fibre while doing so, creating losses at this level of the network.

The microbends are usually assumed to be caused by the contact of the fibre with its environment, as well as by the stress (twist, tension) the fibre is subjected to once in position. This results in numerous local perturbations of the refractive index profile of the fibre, scattering a fraction of the signal out of the fibre. While this phenomenon can be mitigated by engineering the fibre with protective cladding layers, upgrading the already established fibre network is not currently considered a valid solution.

2.2.3 Selecting the right light source

Using fibre optics to transmit information across long distances (such as across an ocean) appears to be the best solution available. The main reasons are that fibre can achieve much higher data rates than copper wires, and that the attenuation in fibre is very low, reducing the number of relays required to amplify the signal along the path. However, this attenuation is not zero, and a relatively large amount of power still needs to be deployed to transmit the information. In order to increase the power efficiency, as well as to increase the

data rate, complex modulation formats can be used, such as quadratic phase shift keying (QPSK), where two bits are transmitted in a single symbol. The transmission of such symbols require careful control of the signal's phase. One can thus identify two requirements: high power and phase control. Lasers meet those requirements. Indeed, using simple LEDs may be enough to fulfill the power requirement, but the incoherent light is not compatible with phase-controlled modulation formats. Lasers have the advantage of being coherent light sources, enabling such modulation formats, and are thus good candidates for fibre-powered communications. In addition to these two requirements, the saturation of the spectrum makes it necessary to not emit any strong signal in channels allocated to other users. As a consequence, the laser emission needs to be confined at a single wavelength, thus the necessity to use single-mode lasers. In the case of multi-channel transmissions, the failure of a laser tailored for a specific channel can be catastrophic. However, using lasers that can be tuned to different wavelengths makes it possible to reallocate lasers to the different channels, increasing the system's robustness. As a result, tunability is a desirable quality for lasers in optical communication systems. Thus, the single-mode tunable laser, a component at the core of the communication network, is the type of device on which this thesis will focus.

2.3 Providing more and more communication devices

With the growth of internet traffic, and the expansion of the fibre network to cover an ever larger portion of the world, more and more optical communication devices are needed to power the network. Satisfying the need for such devices and components requires the development of efficient fabrication processes. These processes need to enable large-scale production of a variety of components, short lead times from order to delivery, and must guarantee the reliability and repeatability of the products. The fabrication time and cost become a crucial factor in developing industrially attractive solutions, and the approach followed in this work consists in finding the inspiration in the electronics industry, where massive production of highly complex circuits is achieved by simplifying the fabrication process, and by maximising the number of different components that can be manufactured using the same steps. This was translated in this work in an attempt at simplifying the fabrication process, reducing

the lead time, and designing components in a way that is favorable to the integration of multiple components to fabricate entire circuits at the same time, rather than building components separately and assembling them afterwards. This approach will be detailed in the following chapters.

With the ever expanding need for bandwidth and exponential growth of the photonics market, more and more strain is put on companies of the sector that need to satisfy the demand while engaging in a fierce competition between themselves. Observing that Moore's law also applies to photonics [6], the evolution of production processes towards ever larger scale fabrication appears necessary to satisfy the needs of the market. Following the example of microelectronics, one can reasonably consider as likely, an evolution of the production methods towards increasingly complex integrated photonic circuits, which would be produced in ever larger quantities on automated production lines.

Considering the colossal investment an electronics production line represents, one can envision that due to the high similarity of the fabrication processes, photonic large-scale production lines would require equally large investment. For such investments to be made, with the impact on the economy and employment in the regions where such facilities are deployed, the return on investment needs to be satisfying enough to justify the investment. Streamlining the production time and cost thus appears crucial not only from a competition perspective, but also for investors to start such projects.

This thesis is a contribution to the effort of streamlining the fabrication time and cost of semiconductor photonic components. Conducting this research contributes to enabling the large-scale fabrication of highly complex photonic circuits, facilitating the development of an ever stronger communication network around the world and the expansion of broadband coverage to regions and populations still isolated from the rest of the world. Beyond the communication aspect, the contribution to this streamlining effort is an additional step towards the expansion of the young photonics industry and the investment in production facilities, with the resulting social and economical benefits associated with the deployment of industrial facilities.

In the following chapter of this thesis, a summary of the current technical situation will be outlined. Starting with the presentation of a simulation tool extensively used in this work, the main laser designs currently in use will be described, followed by a presentation of fabrication techniques used in the photonics industry. After this broad perspective on the current state of the art is

presented, the focus will be on the work done in this thesis. The fabrication and testing procedures used for this work will be described, as well as the organisation of this research in a cyclic system where the knowledge gained at each iteration is used to refine and improve the next.

Chapter 3

Semiconductor lasers: design, devices, processes

In this chapter, the different aspects of the development of semiconductor photonic components will be presented. Starting with the description of a mathematical tool used in this work to simulate the proposed devices, this method, which is at the core of the validation process prior to fabrication, will be applied to a series of examples. Well-established lasers will be presented with the help of this simulation method, in order to illustrate what solutions are currently in use for optical communications. Following the device development cycle, an overview of the fabrication techniques in use in photonics research and industry will be presented. Their application to this work will then be summarised with a presentation of the fabrication process, along with the description of the process variants proposed in the course of this work. The final part of the device development cycle will then be presented: the device characterisation. The setup used will be described, followed by an overview of the characterisation procedure and of the features analysed in this work.

3.1 Mathematical tools for the study of photonic devices

The scattering matrix method (SMM) [7] is a mathematical tool used to study the behavior of complex photonic circuits by decomposing them into a series of fundamental elements. Each of those elements has a given number of ports.

The SMM describes each element as a matrix where each coefficient corresponds to the signal alteration caused by the studied element, from one port to another. In the general case, each port can be considered as an input and as an output, leading to a square matrix. By considering the vectors $[A_1, A_2, \ldots, A_N]$ and $[B_1, B_2, \ldots, B_N]$ where A_k and B_k are respectively input and output signals through the port k, the scattering matrix **S** is defined as

$$\begin{pmatrix} B_1 \\ B_2 \\ \vdots \\ B_N \end{pmatrix} = \mathbf{S} \times \begin{pmatrix} A_1 \\ A_2 \\ \vdots \\ A_N \end{pmatrix}. \tag{3.1}$$

The coefficients of **S** are S_{mn}, representing the transfer function of the signal from Port n to Port m. In the case of a 2-port system, the equation becomes

$$\begin{pmatrix} B_1 \\ B_2 \end{pmatrix} = \begin{pmatrix} S_{11} & S_{12} \\ S_{21} & S_{22} \end{pmatrix} \times \begin{pmatrix} A_1 \\ A_2 \end{pmatrix}. \tag{3.2}$$

The scattering matrix has an equivalent transmission matrix **T**, that is described as follows for the 2-port case:

$$\begin{pmatrix} A_1 \\ B_1 \end{pmatrix} = \begin{pmatrix} T_{11} & T_{12} \\ T_{21} & T_{22} \end{pmatrix} \times \begin{pmatrix} A_2 \\ B_2 \end{pmatrix}. \tag{3.3}$$

S and **T** are related to each other by the following formulae:

$$\mathbf{S} = \frac{1}{T_{11}} \begin{pmatrix} T_{21} & det(\mathbf{T}) \\ 1 & -T_{12} \end{pmatrix} \tag{3.4}$$

$$\mathbf{T} = \frac{1}{S_{21}} \begin{pmatrix} 1 & -S_{22} \\ S_{11} & -det(\mathbf{S}) \end{pmatrix} \tag{3.5}$$

Considering a linear association of N 2-port elements, such as waveguides (one port at each end) or interfaces between areas of different indices (one port for each side). Let the corresponding transfer matrices be $\mathbf{T}_1$, $\mathbf{T}_2$, ... $\mathbf{T}_N$. The transfer matrix **T** of the association of those elements one after another is

$$\mathbf{T} = \prod_{k=1}^{N} \mathbf{T}_k. \tag{3.6}$$

The power of the SMM resides in the fact that a majority of linear photonic structures can be decomposed in a series of simple, fundamental elements being either a waveguide section, or a reflective interface. The scattering matrix for a section of waveguide is the following:

$$\begin{pmatrix} 0 & e^{-j\phi} \\ e^{-j\phi} & 0 \end{pmatrix}, \tag{3.7}$$

where j is the imaginary number and ϕ is the complex value including the phase variation due to the waveguide's length, as well as the gain or absorption that could occur during the propagation. A reflective interface has the following scattering matrix:

$$\begin{pmatrix} r & t \\ t & -r \end{pmatrix}, \tag{3.8}$$

where r and t are respectively the reflection and transmission coefficients of the interface. Most of the common structures involved in PICs can be defined as a combination of those two fundamental blocks. As such, it is possible to simulate significant portions of PICs, using the SMM. In the case of more complex structures that cannot be simply defined as a 2-port system, the SMM can still be used to study sections of the PIC to determine their transfer functions and use them to determine the behavior of the full PIC.

The method described here can be used to estimate the reflection profile of a large variety of structures. Given that the lasing is heavily dependent on the round-trip of the light within the cavity or cavities, it appears obvious that the reflection profile of the different structures has a direct impact on the laser emission spectrum. Indeed, the lasing will occur at the wavelength where the gain and reflectivity are the most favorable.

In this work, the proposed designs are not linear, and include multiple arms coupled in parallel, making the use of the SMM non-trivial to model the behaviour of the lasers. However, it can be used to simulate the behaviour of different sections of the lasers and obtain transfer functions that can be used in conjunction with additional methods to simulate the lasers. The SMM proved particularly useful for the simulation of looped devices, where sections must be considered from both sides in transmission and reflection. It is noteworthy that in the case of this work, the focus was put on simulating the reflection profile to predict which wavelengths could be sustained in the devices, and no

other considerations such as the gain were taken into account: the purpose of this simuation was not to model the laser entirely, but to support the design of geometries that would have the desired reflection profiles and corresponding spectral features.

3.2 Semiconductor laser diodes

A semiconductor laser diode consists of an active, intrinsic region, into which carriers, electrons and holes, are pumped from the N and P regions of the device. This pumping is generally achieved by applying a forward electrical bias to the diode. When electron-hole pairs recombine, the emission of photons occur, the photon energy corresponding to the energy released in the recombination. The laser material determines the bandgap, and thus the energy and wavelength of the emitted photons. In semiconductor lasers, the light is confined in a waveguide generally terminated by reflective ends forming a resonating cavity, where part of the generated light is reflected and remains in the device.

The photons present within the laser cavity can interact with atoms that were excited by the pumping. This interaction can result in stimulated emission, where the atom will drop to a lower state of energy, releasing a photon of same wavelength, phase, polarization and travel direction as the incident photon, resulting in optical gain that can compensate the losses, caused for example by material absorption or or transmission through the reflective end of the cavity. When the gain is equal to the losses, lasing threshold is reached. Beyond that point, stimulated emission dominates spontaneous emission, and lasing occurs.

In order to increase the efficiency of the simple laser diode structure, alternative structures were proposed. The one in use in this work is the multiple quantum well structure [8]. A quantum well is formed when the intrinsic region of the diode is narrowed to the point where quantum confinement occurs: the carriers are trapped at a determined energy level, that is tailored to favour the spontaneous emission at the target wavelength, thus increasing the efficiency of the laser. A stack of multiple quantum wells improves the overlap of the gain region with the optical waveguide mode.

3.3 Overview of the solutions currently in use

In this section, a number of mature and more recent lasers will be presented. Their description will be accompanied by simulations done using the SMM, showing how the cavity design leads to selecting specific lasing wavelengths.

3.3.1 Why single-mode, tunable lasers are needed

A specific class of lasers is needed in WDM systems: single-mode lasers. Such lasers have a narrow emission spectrum, where most of the power is focused on a specific wavelength. The quality of this single-mode behavior is measured with the side-mode suppression ratio (SMSR) that represents the power ratio between the strongest emission wavelength, and the second strongest one. In the simplest lasers, there are often several wavelengths, or modes, at which light is emitted. This is because several modes can be compatible with the laser geometry. However, this phenomenon is counter-productive in WDM systems. Indeed, each channel being controlled separately, using lasers that emit light also on other channels would disturb the transmission. In such conditions, only single-mode lasers can be used. Typically, SMSR values higher than 30dB are used in WDM applications.

The tunability also is an important parameter in developing lasers for WDM applications. Standard communication grids have been set, specifying the spectral position of each transmission channel. It is thus necessary to design lasers that comply with those requirements. However, relying only on the fabrication process to obtain a laser that perfectly fits in the grid is not wise. It is necessary to be able to adjust the output spectrum of the device, to guarantee it will follow the standard communication grid. Tunability, or the ability to select the emission wavelength, is thus necessary. It can be done by shifting a given lasing mode across the spectrum, or by favoring another mode so that this new one lases, rather than another. From a large-scale fabrication and integration point of view, using a single design of tunable lasers, able to reach a variety of wavelengths, is much easier than having a specific design for each wavelength.

In the following sections, we will study some examples of lasers, from the simple Fabry-Perot cavity to more complex structures.

3.3.2 The Fabry-Perot laser

The simplest semiconductor laser one can fabricate, is the Fabry-Perot laser. It consists only of a waveguide, with reflective facets at each end. When an electric current flows across this structure, light will be generated through spontaneous emission. A part of it will then be maintained in the cavity, due to the reflective ends. Stimulated emission will then amplify this light. Threshold is reached when the round-trip gain is equal to the round-trip losses, caused by the material absorption and the imperfect reflectors that let some light escape the cavity. This is the point when lasing begins.

In a Fabry-Perot cavity, only some wavelengths can be maintained: those for which the standing-wave equation is verified:

$$L_{cav} = k\frac{\lambda}{2n_{cav}}, k \in \mathbb{N}, \tag{3.9}$$

where L_{cav} is the cavity length, λ the wavelength in vacuum, n_{cav} is the cavity's index and k the longitudinal mode number. Using the scattering matrix approach described in [7], one can simulate the behavior of such a cavity. The reflection profile of this structure indicates which modes can be maintained in the cavity, and which cannot.

One can simulate the behavior of a Fabry-Perot laser using the SMM. This structure being a length of waveguide between two reflective interfaces, the SMM appears to be a very relevant approach. Considering the matrices $\mathbf{T}_{WG}$ and $\mathbf{T}_{ref}$ transfer matrices of respectively the waveguide and the interfaces between the semiconductor's facet and the air, one can write the transfer matrix $\mathbf{T}_{FP}$ for the Fabry-Perot cavity:

$$\mathbf{T}_{FP} = \mathbf{T}_{ref} \times \mathbf{T}_{WG} \times \mathbf{T}_{ref} = \frac{1}{t}\begin{pmatrix} 1 & r \\ r & 1 \end{pmatrix} \times \begin{pmatrix} e^{j\phi} & 0 \\ 0 & e^{-j\phi} \end{pmatrix} \times \frac{1}{t}\begin{pmatrix} 1 & -r \\ -r & 1 \end{pmatrix}, \tag{3.10}$$

$$\mathbf{T}_{FP} = \frac{1}{t^2}\begin{pmatrix} e^{j\phi} - r^2e^{-j\phi} & 2rj\sin(-\phi) \\ 2rj\sin(\phi) & e^{-j\phi} - r^2e^{j\phi} \end{pmatrix}. \tag{3.11}$$

It is then possible to extract the reflection profile of the cavity, being the S_{11} coefficient, using Equation 3.4:

$$S_{11} = r - \frac{rt^2e^{-2j\phi}}{1 - r^2e^{-2j\phi}} \tag{3.12}$$

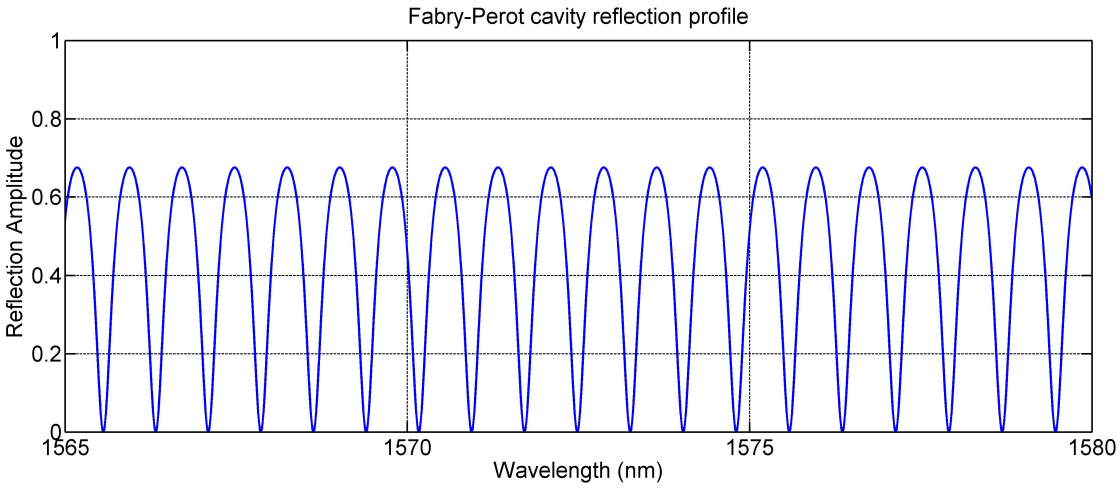

Figure 3.1: Simulated Fabry-Perot cavity reflection profile - the maxima correspond to the wavelengths that can be sustained in the cavity

An example is shown in Figure 3.1, for a 500μm long cavity with simple cleaved facets, with an index of 3.2 (typical index for InP-based material), in air. As suggested by Equation 3.9, the sustainable modes (maxima of the reflection profile) are directly related to the cavity length. This profile is obtained by taking the squared amplitude of the values described by Equation 3.12.

In this case, one can see that the sine-like reflection profile suggest that a large number of modes can be sustained in the cavity. It is thus difficult to control the lasing wavelength, as several modes could lase at the same time. Such devices are clearly inadequate for WDM applications. This is why, from this fundamental cavity that best illustrates how threshold is reached, much more complex structures are used to obtain emission spectra that fulfill the requirements of standard optical communication grids.

3.3.3 Single mode lasers

The example of the Fabry-Perot cavity, with the standing-wave equation, illustrates how the geometry of the device has a great influence on the emission spectrum. Based on this observation, one can try and develop alternative geometries that would favor some modes rather than the others, leading to single-mode lasing

Obtaining single-mode lasing

The main lever to influence which wavelengths can be maintained in the laser structure is the geometry of said structure. This can be done by replacing one or both of the facets by a grating, where the periodic index variation index will result in successive reflectors. The reflected light of each reflector will interfere with the one from the other, so that there is constructive interference only at specific wavelengths. This principle can also be applied to the laser cavity itself, rather than just the end(s). Alternatively, splitting the cavity in a series of sub-cavities will also make it possible to achieve single-mode behavior, when the reflection profiles match only for one mode. The following examples illustrate those solutions.

Distributed Bragg Reflectors

Lasers using distributed Bragg reflectors (DBR) were initially developed in the late 1970's [9]. In DBR lasers, one or both of the reflectors is not a simple cleaved facet, but a section in which the refractive index varies periodically along the device. Such a variation results in a series of interfaces, where a reflection occurs, the reflection coefficient r depending on the indices on each side of the interface, n_1 and n_2:

$$r = \frac{(n_1 - n_2)^2}{(n_1 + n_2)^2}. \tag{3.13}$$

The spacing between those interfaces is defined by the desired emission wavelength:

$$L_{period} = \frac{\lambda_{Bragg}}{4n}, \tag{3.14}$$

where L_{period} is the length of the section of index n, and λ_{Bragg} is the target wavelength that should be reflected towards the cavity for amplification. One can note that, ignoring all gain or attenuation the length of each section leads to a constant phase change ϕ:

$$\phi = \frac{2n\pi}{\lambda} \times \frac{\lambda_{Bragg}}{4n} = \frac{\pi}{2} \times \frac{\lambda_{Bragg}}{\lambda}. \tag{3.15}$$

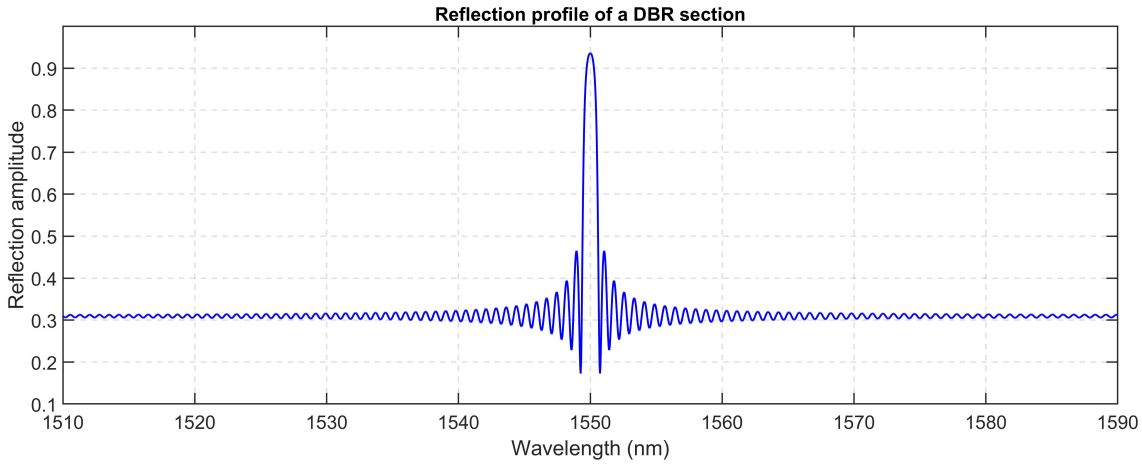

Figure 3.2: Simulated reflection profile of a DBR mirror including 1000 grating periods designed for a reflection at 1550nm, with refractive indices of 3.52 and 3.515

Considering a single period of the grating, composed of a waveguide of low index, an interface, a waveguide of high index, and another interface, one can write the transfer matrix $\mathbf{T}_{period}$ of this period:

$$\mathbf{T}_{period} = \begin{pmatrix} e^{j\phi} & 0 \\ 0 & e^{-j\phi} \end{pmatrix} \times \frac{1}{t}\begin{pmatrix} 1 & r \\ r & 1 \end{pmatrix} \times \begin{pmatrix} e^{j\phi} & 0 \\ 0 & e^{-j\phi} \end{pmatrix} \times \frac{1}{t}\begin{pmatrix} 1 & -r \\ -r & 1 \end{pmatrix}. \tag{3.16}$$

After calculation:

$$\mathbf{T}_{period} = \frac{1}{t^2}\begin{pmatrix} e^{2j\phi} - r^2 & r(1 - e^{2j\phi}) \\ r(1 - e^{-2j\phi}) & e^{-2j\phi} - r^2 \end{pmatrix}. \tag{3.17}$$

A transfer matrix can then be (numerically) calculated for a full grating composed of m periods:

$$\mathbf{T}_{grating} = \mathbf{T}_{period}^{m}, \tag{3.18}$$

from which the S_{11} coefficient can be extracted to determine the reflection profile of the DBR. This calculation can be applied to most of the gratings, as shown in the other examples. Simulating a DBR section using the SMM leads to reflection profiles such as the one presented in Figure. 3.2. The cardinal sine (sinc) shape illustrates the wavelength selectivity of such structures. By favoring a specific wavelength, it is possible to ensure only this one lases.

Practical DBR lasers can use one DBR mirror, the other end being a cleaved

facet, with [10] or without [11] a high-reflectivity (HR) coating. Some others use two DBR mirrors, one at each end of the structure [12]. A phase control section is sometimes included in the structure [13]. Some variants can be found where the DBR section is positioned between two gain sections, with each end cleaved [14]. One can note that using DBR mirrors rather than cleaved facets makes it possible to integrate other elements after the grating, such as semiconductor optical amplifier (SOA) sections to boost the output power, or modulator elements [10].

The fabrication process of DBR gratings is divided into several steps. A first epitaxial growth is performed, and the grating is etched. The dimensions of such gratings being extremely small (see Eq.3.14), traditional photolithographic processes are not adapted to this resolution. It is necessary to use other methods, such as electron beam lithography (the photoresist is exposed to a beam of electrons that engraves the grating's pattern) or holographic lithography, where interference fringes are used to expose or protect the photoresist. After the lithography and the consecutive etch, additional layers of material are epitaxially grown on top of the sample. Eventually, the waveguides and other structures are etched using standard processes. More details on the two-step growth process can be found in [15]. Epitaxial growth and advanced lithography techniques being expensive and time-consuming, the fabrication cost of such lasers is relatively high. Regrowth-free variants have also been reported, however they still require advanced lithography ([16, 17]).

Sampled-Grating Distributed Bragg Reflectors

As shown in the previous section, DBR mirrors allow only a limited portion of the spectrum to be reflected, around a single wavelength. As a result, the tuning range remains limited. It has been noted that the sinc shape of the reflection profile is the Fourier transform of the index profile along the DBR structure. However, it can be derived from the Nyquist-Shannon sampling theorem that the Fourier transform of a sampled signal is the Fourier transform of said signal, periodically repeated over the corresponding Fourier space. From this observation, a variant of DBR has been developed, where the grating is present only periodically, as the result of the grating function multiplied with a sampling function. The resulting device is thus called sampled-grating DBR (SG-DBR). A detailed theoretical analysis can be found in [18].

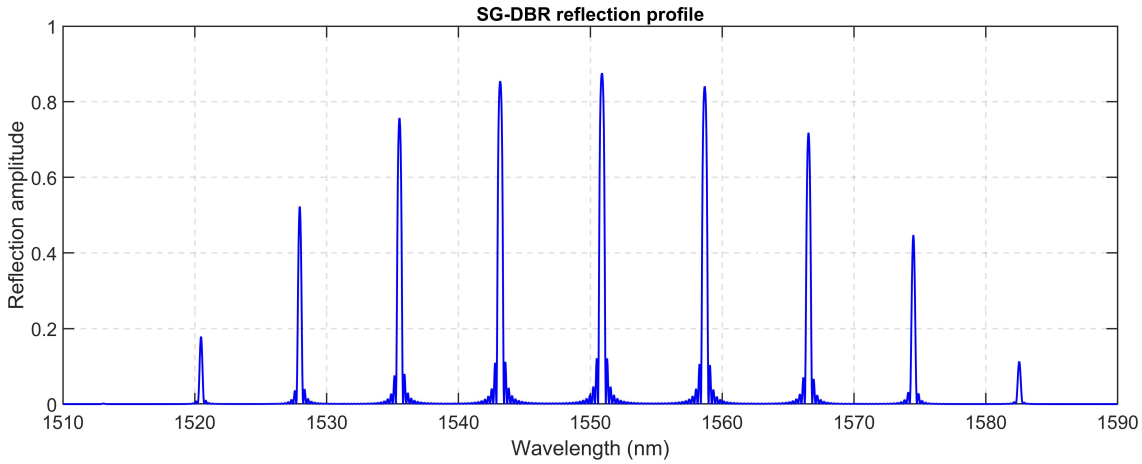

Figure 3.3: Simulated SG-DBR mirror reflection profile for 30 sampling periods, each containing 40 grating periods with indices 3.52 and 3.515

The reflection spectrum of SG-DBR structures is a series of cardinal sine functions, centered at regular intervals of the spectrum, as illustrated in Figure 3.3. It was obtained by alternating a series of grating periods as determined in the DBR example, with a longer section of waveguide, to represent the sampling function. Combining two of those structures in a laser device makes it possible to select the lasing wavelength by selecting the matching maxima of the two sections. This being done, it is possible to select another wavelength by modifying the bias on one of the SG-DBRs. By doing so, the slight index variation will shift the reflection spectrum, so that the match between the spectra is obtained at another wavelength. Such a mode selection is called Vernier tuning.

In order to cover a large spectrum, such devices can be fabricated into an array to modulate data on several channels simultaneously [19, 20], with SMSR values above 40dB [21]. Structures using only one SG-DBR also exist, and are combined with a phase control section to select the lasing wavelength, the other reflector being a cleaved facet [22]. Other variants include complex sampling functions such as the interleaved sampled grating [23].

Distributed Feedback Lasers

Distributed feedback (DFB) lasers have been studied from the 1970's, by introducing a corrugation along the laser cavity. Similarly to the DBR case, wavelength control is obtained by creating a grating in the structure. But in the case of DFB lasers, the grating is directly part of the lasing cavity, rather than acting

as a reflector at an end of the device. They can be optically [24], or electrically [25] pumped. In DFB lasers, the light is confined by the multiple internal reflections. Similarly to the DBR case, the Bragg wavelength defined by the grating's period is used to select the lasing wavelength. One or both of the facets are then cleaved to ensure good feedback. Once the Bragg wavelength is defined, relying solely on the grating and on the - random - position of the cleaved facets appears unwise, as the wavelength also has to be compatible with the cavity length. A small phase shift region can be added in the laser [26], leading to single mode operation when both facets are coated with an anti-reflective (AR) coating.

As the physical dimensions of the device don't permit a wide tunability, DFB lasers are often used in arrays where the laser corresponding to the desired wavelength is powered. The emitted light is then collected and transmitted to the other elements of the photonic circuit. This collection can be done with the help of a rotating mirror that redirects the light through a lens that focuses it on the output fibre [27], by using a multimode interference (MMI) coupler [28, 29], or a star coupler [30, 31].

Slotted Fabry-Perot Lasers

DBR, SG-DBR and DFB lasers have been widely studied over the last decades, and numerous systems are using them to power WDM communications. However, their fabrication process often involves an epitaxial regrowth step, and high-resolution lithography techniques. This comes at a high cost, both in time and money, reduces the yield, and thus their interest for large-scale production. Developing alternative solutions that don't require regrowth or high-resolution processes appears extremely interesting from an industrial point of view.

In the lasers previously mentioned, the index variations were induced by altering the core of the material, leading to a costly two-step growth process. An alternative has been proposed, where discrete index variations were induced by altering the surface of the device, rather than its core. The proposed technique consists in etching local imperfections (slots) on the Fabry-Perot cavity, thus the name: slotted Fabry-Perot (SFP) laser. The shape of a slot is illustrated in Figure 3.4. Those imperfections induce a local refractive index variation that can be used to select the modes that are maintained in the cavity. By carefully positioning the slot, it is possible to prevent some longitudinal modes from developing

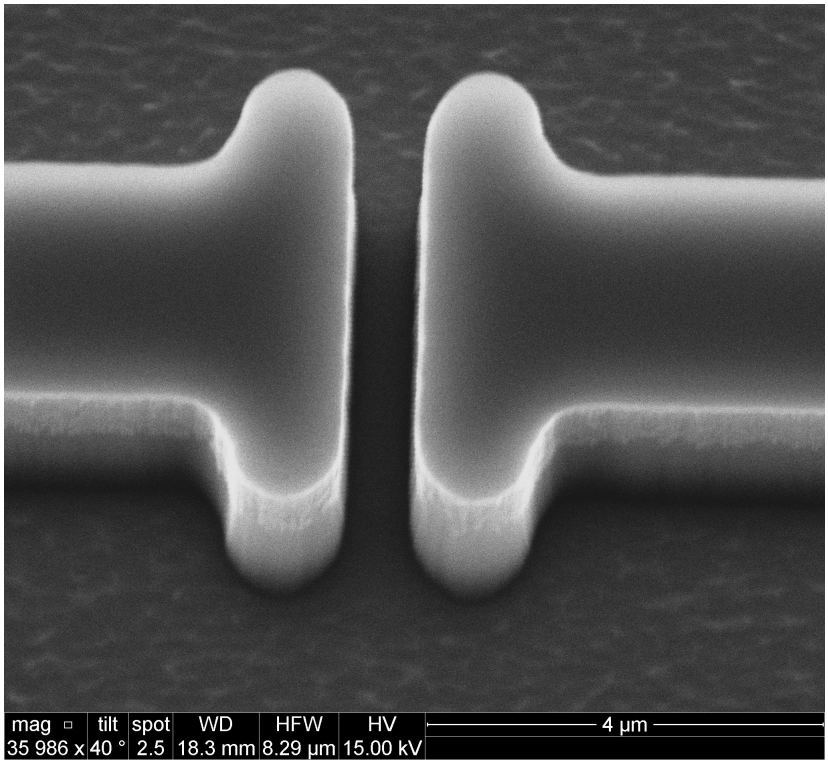

Figure 3.4: SEM picture of a slotted ridge - the T shape helps pushing away imperfections at the angles, for a flat interface

in the laser cavity, leading to single-mode lasing. The slots being defined and etched during the same step as the ridge waveguide, they require no additional fabrication step. Furthermore, their dimensions (typically 1μm wide) make it possible to use only standard lithography processes, further reducing the fabrication cost and time.

Initial results showed SMSR values of 25dB for three slots positioned at 1/2, 1/4 and 1/8 of the cavity [32]. More recent work proposing laser arrays showed SMSR values higher than 40dB for five slots. By modifying the inter-slot distance, it was possible to select the lasing wavelength [33]. Other variants have been developed, such as the two-section SFP laser where the two sections have slots with different spacing to obtain Vernier tuning [34]. A three-section SFP has been reported to cover 25 channels of the standard 100GHz International Telecommunication Union (ITU) communication grid in the C band, and to be compatible with advanced modulation formats [35]. Recently, lasers consisting of three sections separated by a slot have been reported to cover one half of the 50GHz ITU grid [36]. This recent gain of interest in slotted structures has underlined the need for more detailed studies of the slots' properties, leading

to the confirmation that while the slot width has only marginal influence, its reflection and transmission properties depend exponentially on the slot depth [37, 38].

Another use of slots has been studied, where their reflective properties are used to create a reflective grating, in a fashion similar to DBR laser structures. By etching slots in the waveguide, a local index variation is created. A waveguide on which a series of slots shows the same type of reflections than a DBR. However, the distance between the slots is much larger than the distance between the DBR's index variations. Indeed, the slots can be separated by several micrometers, while the DBR's period is a fraction of the target wavelength. The use of such structures removes the need for mirrors, and lasers relying on a pair of slotted reflectors have been demonstrated. Using different periods on the reflectors leads to single mode lasing and Vernier tuning [39, 40]. As such lasers don't rely on cleaved facets, they can easily be combined with other devices or waveguides, for further integration [41]. However, it is noteworthy that the slots cause power losses that need to be compensated by gain, and the mirror sections require a large number of slots, resulting in long section lengths and increasing the device's footprint.

The Vernier effect used by the SFP lasers introduced here is based on the combination of two or more coupled Fabry-Perot cavities of different lengths. As described for the Fabry-Perot laser, only the wavelengths that are solutions of the standing wave equation for the considered cavity, can be maintained in it, resulting is the periodic profile shown in Figure 3.1. Considering now that two Fabry-Perot cavities are coupled together, the wavelengths sustained in the system must satisfy the standing wave equations for the two cavities at the same time. Referring to the periodic profile, only the wavelengths corresponding to maxima of both profiles can be sustained in the system. Given that SFP lasers are generally a monolithic device using the same material being used for the different cavities, the parameter that will define the number of common maxima will be the length of the cavities. By selecting the cavity lengths so that there is only one matching wavelength over the operating spectrum of the laser, this wavelength will be the most susceptible to lase, resulting in single-mode operation.

The wavelength tuning of the laser is then possible by using the Vernier effect. Indeed, by changing the injected current into the sections of the SFP laser, the length and refractive index of the section will be altered, changing the param-

eters of the standing-wave equation and thus the solution wavelengths. Practically, it results in shifting the profile of the cavity. In a multi-cavity system, this shifting causes the common maxima to be found at wavelengths other than before adjusting the injected current, resulting in single-mode lasing at a different wavelength for SFP lasers.

3.3.4 Advantages and limitations of the current solutions

The grating-based lasers described here are a well-established technology, and show good single-mode performance with SMSR values above 40dB. However, DBRs and DFBs suffer from a poor tunability, due to the grating dimensions that impose a lasing wavelength. This aspect can be mitigated with the SG-DBR where the sampled grating allows for a wider tuning range. In addition, the use of a phase control section can remove the need for a cleaved facet, facilitating the monolithic integration of the laser with other components, but potentially requiring the use of AR coatings, increasing the fabrication complexity. These types of lasers are based on gratings that require the use of advanced lithography techniques for their fabrication, such as electron-beam lithography that is a slow and expensive process, or holographic lithography that is faster, but expensive. The regrowth is another part of the process that significantly impacts the fabrication time, reducing the attractiveness of such lasers for industrial scale production. Regrowth-free DFBs have been reported ([16], [17]), but still require the use of advanced lithography to achieve the quarter-wavelength resolution necessary for the gratings. These lasers thus show excellent single-mode performance and are a mature technology, but simpler, cheaper solutions need to be considered to increase the manufacturing scale.

A common alternative to gratings that is used today is the SFP laser. The use of sections of different lengths enables wide tunability and slotted mirrors result in SMSR levels above 40dB, and facilitate the integration of the lasers with other components. Due to their fabrication simplicity, manufacturing such structures is easy and fast. However, the slotted sections can be of significant length, increasing the footprint of the component. Moreover, the slots' performance is heavily dependent on the etch depth, and the losses at the slot, particularly for slotted mirrors including a large number of those features, makes this type of laser less repeatable. Indeed, any variation of depth has a major effect on performance [42]. As a result, although the large-scale production of SFPs is

relatively simple, the variability of performance can be crippling when the repeatability is a major concern of industry, with the widely used "6-Sigma" doctrine [43] that considers stable, predictable process results of vital importance to business success.

Given those observations, it appears relevant to explore alternatives that can be produced at industrial scale in an efficient and repeatable manner.

3.4 Towards a large-scale production of photonic circuits

With the ever-growing need for bandwidth in optical communication, it is clear that there is a need for photonic components that can be fabricated with high yield, at reduced cost. In order to achieve such a production, it appears necessary to develop complex photonic components and circuits that do not require expensive or slow fabrication steps. Another approach that can be considered, is the integration of multiple components, all fabricated at the same time, as done for integrated electronic circuits. This approach makes it possible to build complex circuits while limiting the fabrication time.

In such a context, the present work was oriented to explore the options available while remaining compatible with easy fabrication and facilitated integration. The component type studied was the laser, under the following set of constraints:

- Standard UV contact lithography only;
- Regrowth-free process;
- Cleave-free design for straightforward integration.

The objective under this set of constraints was to achieve single-mode operation and tunability, and to demonstrate the feasibility of the monolithic integration of the designed lasers with other components. The desirable SMSR for the single-mode nature of the lasers was set at 30dB or higher. While no minimal tuning range was defined, the goal was to expand it as much as possible, in order to cover the largest possible portion of the spectrum with a single device. Indeed, in the case of multi-channel communication, having one design of laser used to cover the entire target range can contribute to reducing the product

design complexity and cost. Finally, it was chosen to use electro-absorption modulators (EAMs) and gain-switched lasers for comb generation as the components to be integrated with the proposed lasers.

The work was done iteratively, over a series of laser generations where different geometries and fabrication techniques were explored in an attempt to develop a portfolio of options that are compatible with the objectives.

Given the set of limitations chosen for this work, specific fabrication techniques were not used in the development, such as electron beam lithography or regrowth. However, most of the techniques used for semiconductor fabrication were still acceptable in the chosen set of constraints. In the following sections, most of the fabrication processes that were used in this work will be described, followed by a presentation of the fabrication procedure, along with details on variants that were developed during this work.

3.5 Fabrication techniques for photonic integrated circuits

The fabrication of PICs starts with the growth of the wafers. In microelectronics, the silicon wafers are sliced from a silicon ingot. A small monocrystalline seed of silicon, of known crystalline arrangement, is dipped into melted silicon. At the contact point, silicon returns to solid state, following the crystalline arrangement of the seed. The monocrystalline ingot is progressively grown, and then is sliced into wafers that are then ready for processing. Similar techniques can be used to manufacture wafers from different materials, such as InP.

However, as mentioned earlier, photonic devices require multiple layers of material. This cannot be achieved solely with the process mentioned in the previous paragraph. Instead, the layers are epitaxially grown at the surface of the substrate wafer. The three main techniques for epitaxial growth are liquid-phase epitaxy (LPE), metal-organic chemical vapor deposition (MOCVD) and molecular beam epitaxy (MBE). In an LPE system, a substrate wafer is positioned in a furnace, and on which holders filled with the desired materials in liquid phase are applied. Layers of material will then grow at the surface of the wafer, while the holders are slid along the surface of the wafer. In the case of MOCVD, the substrate is exposed to a laminar gas flow that carries the growth

compounds. MOCVD can be done at low pressure or at atmospheric pressure, depending on the desired material properties and process requirements. Indeed, while atmospheric pressure leads to higher growth rate, the time required to clean the chamber from gases used for the previous layer is much longer. In the case of quantum wells, the low-pressure approach is preferred, for it results in clear interfaces between layers. MBE is realised at ultra-high vacuum (UHV). Compounds are evaporated from effusion cells, and condense back on the substrate. More details on those techniques can be found in [7].

Once the wafer is grown and ready for processing, the PICs can be fabricated. Most functions are obtained by removing material from the surface of the wafer. The abrupt change of effective refraction index confines the light in the areas where no (or less) material has been removed. By creating ridges along the wafer, one can thus guide light from one element to another. The removal of material is done in two main steps: first a lithography step, followed by the etching itself.

The lithography step consists in depositing a layer of photoreactive polymer (also called photoresist) at the surface of the sample. Some parts are then exposed to radiation that will alter the polymer structure. Depending on the chosen photoresist, either the exposed areas or the unexposed ones become sensitive to a developer chemical that will dissolve the photoresist. If the photoresist is dissolved in exposed areas, the photolithography is said to be "positive". In the other case, it is said to be "negative". Different exposition techniques exist. Some are based on electron beam lithography: a beam of electron is focused on the sample, to expose the desired areas. This results in an excellent lithography resolution, but is extremely costly and takes a long time. Another solution is to use ultraviolet (UV) light. A mask is positioned between the sample and the UV source, so that only the desired areas are exposed. The mask is made of quartz, on which a layer of chrome is deposited, following the shape of the areas to be exposed/protected. By selecting shorter wavelengths, one can reduce the diffraction inherent to this technique, and obtain sub-micron resolution. Verification structures are often scattered across the mask, where features of increasingly smaller size are included. Microscope imaging (Figure 3.5) of such structures after photoresist development, makes it possible to assess the lithography quality and resolution before proceeding any further. In the case of Figure 3.5, the 1.5μm and larger features are satisfyingly resolved, but the 1μm and smaller are showing imperfections that suggest devices with sub-micron features might not be correctly resolved by this lithography.

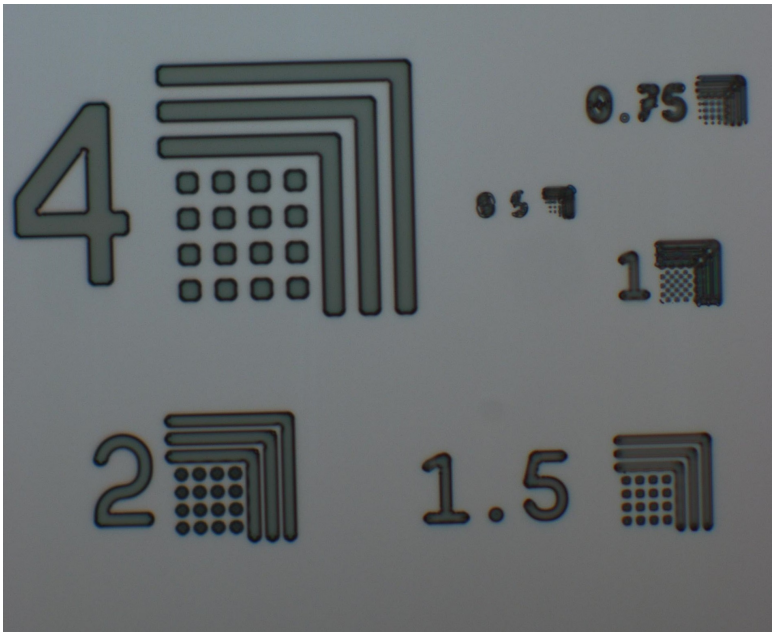

Figure 3.5: Microscope image of lithography resolution verification structures after photoresist development - the numbers correspond to the size of the nearby features in μm

Once the lithography is completed and the photoresist is developed, the exposed parts of the sample can be etched. The two main ways to proceed are wet etch, and dry etch. Wet etch is done using liquid-phase etchants, by simply dipping the sample into the etchant for an appropriate time. This process is often sensitive to the crystal orientation, and is isotropic. As a result, it can cause an undercut, and damage areas under the protective photoresist by etching the side walls. On the other hand, its selectivity implies that if an etch-stop layer, with the adequate composition, is included in the layer structure of the sample, the etchant will not remove material any deeper. This can be used to obtain a smooth surface, or to accurately reach a desired etch depth.

A dry etch, on the other hand, relies on the use of a plasma that will physically remove atoms from the surface of the sample. The very nature of the process leads to poor chemical selectivity, but the directional etch prevents an undercut, leading to quasi vertical etch walls as illustrated in Figure 3.6. This process is most often used for the first etch steps, while a wet etch is used to remove the last nanometers of material. The combination of those techniques results in clean, vertical side walls that ensure good light confinement and accurate depth control with limited undercut. Because of the physical principle of the plasma generation, the dry etch used for the present work is often referred to

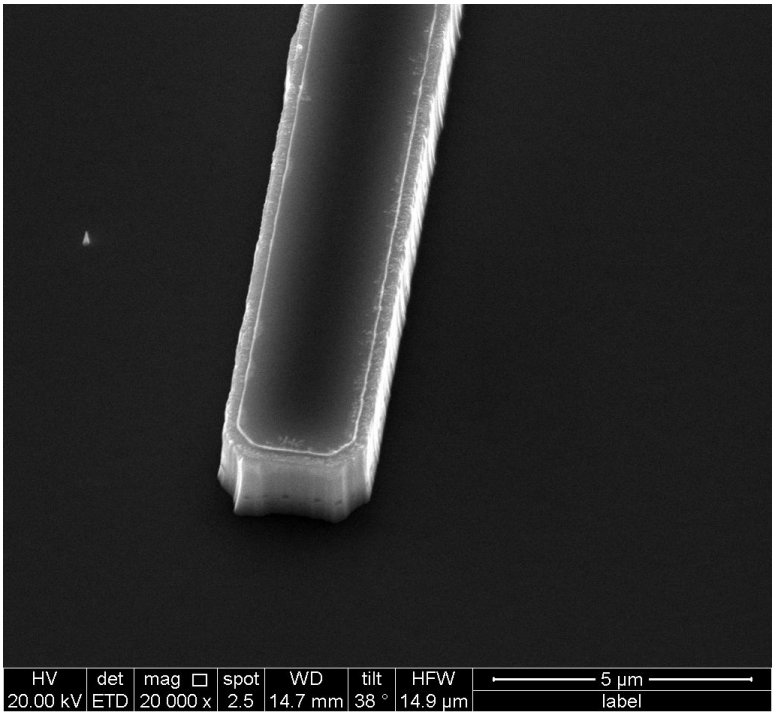

Figure 3.6: SEM image of a ridge after semiconductor etch - the chamfer shape at the corners (it should be a right angle) justifies the T shape for the slots to ensure a flat interface

as inductively coupled plasma (ICP) etch.

When photoresist masks are not enough, layers are added to the surface of the sample, such as silicon oxide or silicon nitride. In the rest of this document, these will be refered to as "oxide" and "nitride", silicon being implicit. They protect parts of the sample, and are called a hard mask. Such layers are grown on the surface of the sample by plasma-enhanced chemical vapor deposition (PECVD). The combination of those masks with photoresist layers is used to etch complex structures while limiting the number of lithography steps.

3.6 Typical DC fabrication process

The first elements to be fabricated on the sample are the wave-guiding structures. They are the core elements of the devices. First, a layer of oxide is deposited on the wafer. This is done using PECVD, for a thickness between 500nm and 700nm. A photoresist layer is then spun on the oxide, and the lithography is performed. All the alignment marks (Figure 3.7) are included in the pattern, so that subsequent alignments are based on this initial step rather than on the

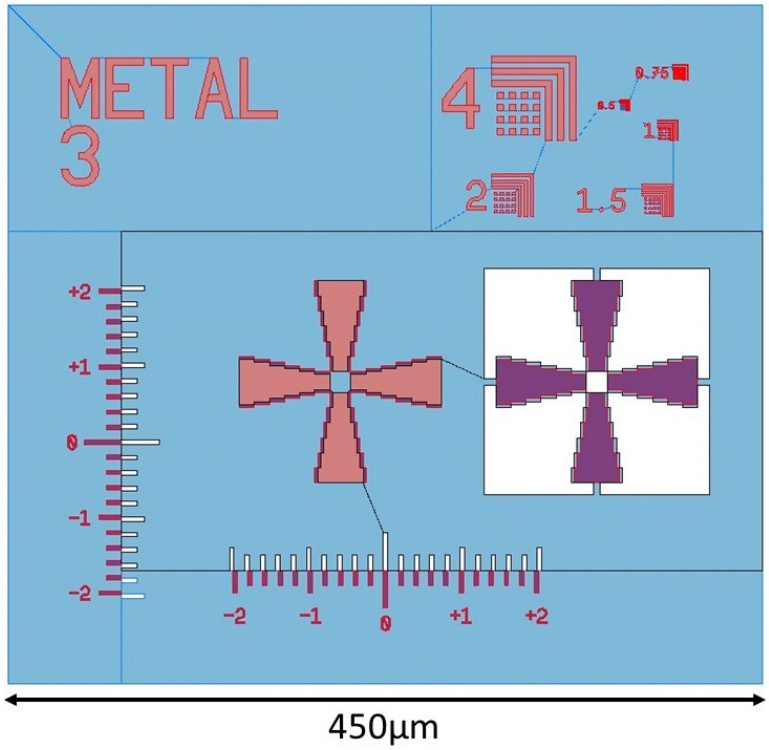

Figure 3.7: Schematic of the alignment marks used throughout the process

immediately previous step. This helps avoiding the propagation of misalignment from one step to the other. After development, only the to-be waveguides remain covered in photoresist. The exposed oxide is etched away using the dry etch process described earlier, and the remaining photoresist is removed. At this level, the wafer is still intact, but the ridge patterns are imprinted with oxide on top of it (Figure 3.8). This first step is one of the most critical ones, as most of the features are drawn during it. In the case of extremely small features such as slots, it is crucial to ensure they are resolved with a sufficient precision to avoid any significant alteration of their shape, which could lead to electrical isolation faults or losses caused by scattering.

In the case some areas need a deeper etch than others, some steps can be added after the initial oxide etch. A layer of silicon nitride (350 to 500nm) is deposited on the sample, using PECVD (Figure 3.9). Using lithography, the areas where the deep etch are required are left exposed, the rest being covered in photoresist. The nitride is then etched away in the exposed areas, using a selective dry-etch. At this level, the semiconductor is exposed in the areas that need to be deep etched, but any future waveguide present in the area is still protected by the oxide (Figure 3.10). Semiconductor is then dry etched to the adequate

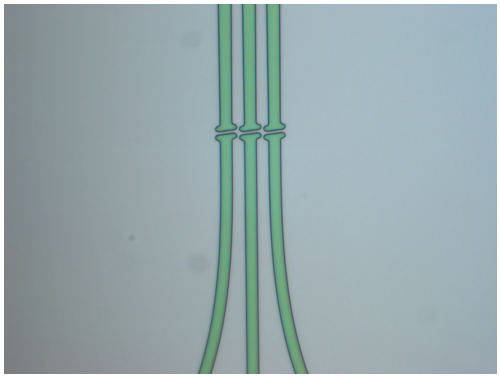

Figure 3.8: Microscope image of waveguide patterns etched in silicon oxide

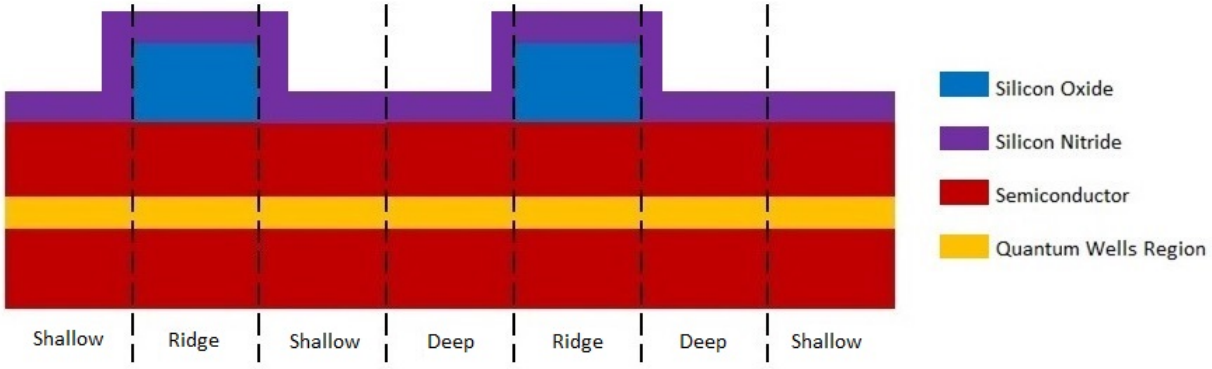

Figure 3.9: Wafer profile schematic after nitride deposition - depth indications refer to the target etch depth

depth (Figure 3.11), slightly above the quantum well region. A final wet etch can be used, in order to ensure the side walls are smooth and to guarantee the desired depth has been reached. Finally, the rest of the nitride is removed.

At this level, only the oxide remains and the shallow etch can be performed. By etching the semiconductor in the whole exposed area, the preserved areas are etched to the desired depth, with a typical target being approximately 100nm above the quantum wells, at a layer designed to resist chemical etching. The areas that had already been etched are etched even deeper, below the quantum wells (Figure 3.12). The remaining oxide is removed, so that only semiconductor material remains at the surface of the sample (Figure 3.13). A fresh layer of oxide is then deposited. It is used to protect the semiconductor material, and ensure good isolation between the material and the electrical contacts that will be added.

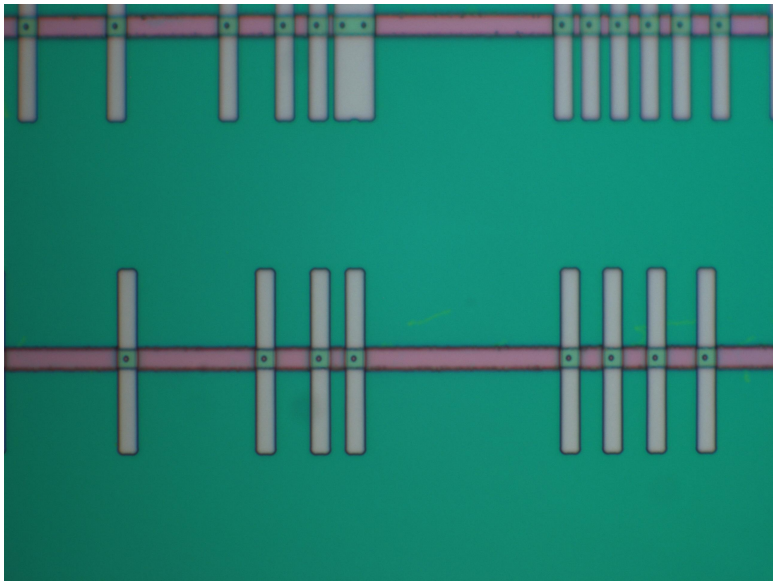

Figure 3.10: Microscope image of nitride openings around pits on ridges

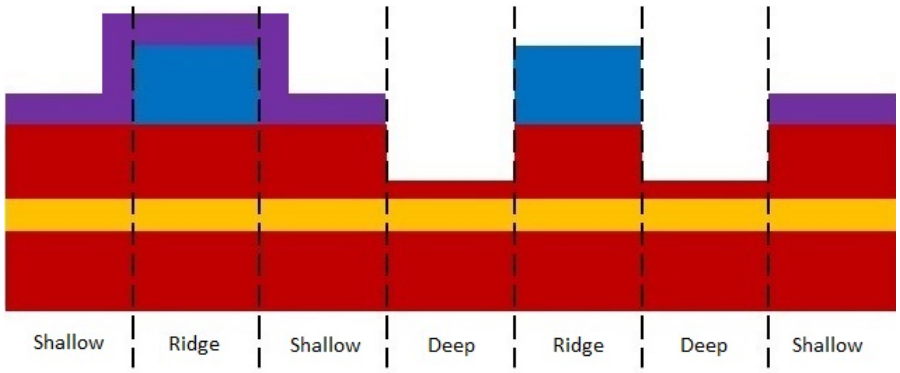

Figure 3.11: Wafer profile schematic after deep etch

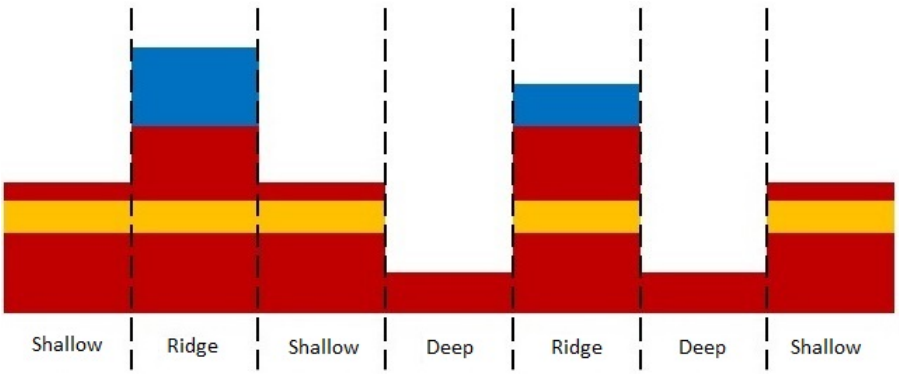

Figure 3.12: Wafer profile schematic after nitride removal and semiconductor etch

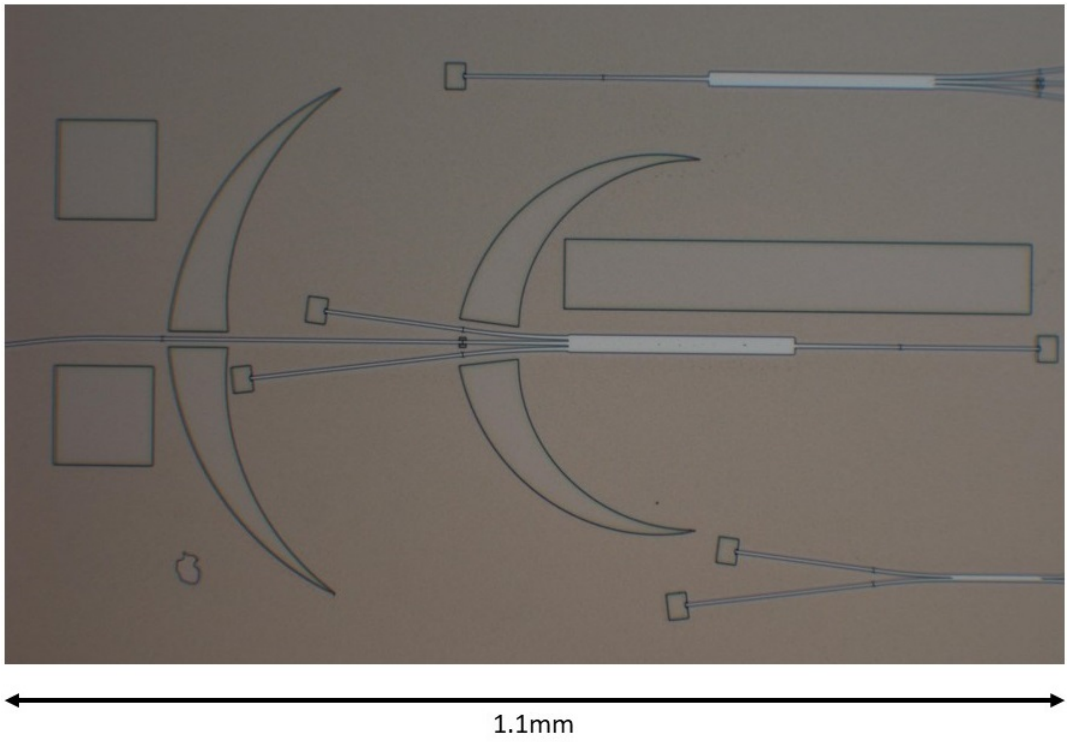

Figure 3.13: Microscope image of a future 1-by-3 MMI-based modulated laser after the nitride removal and semiconductor etch

In order to power the device, electric current needs to be provided to the different sections. This is done by positioning metal contacts and lines on the surface of the chip. However, it is necessary to ensure the current flows only where needed. To do so, a trench is opened in the oxide, on top of the structures that need to be powered. This is done by etching the oxide on the waveguides, using a lithography-etch process. It is critical to have good alignment at this level, as the opening has to be only on top of the structures, or current would flow away from the area that needs to be powered. A ridge being typically 2.5μm wide and the opening being typically 1.5μm wide, the margin for misalignment is very limited.

A solution used to facilitate this step and slightly increase the alignment tolerance, is the reflow technique. A thick photoresist is spun onto the surface of the sample. Once the mask and sample are aligned, the contact is made between the two, prior to exposure. However, the pressure applied between the mask and the sample is lower than usual. This is done by bringing the two elements against each other but without adding any supplementary force to tighten the contact. This leads to a reduced resolution and, by diffraction, to a larger exposed area. By over-exposing the sample to UV light (2 to 3 times the dose

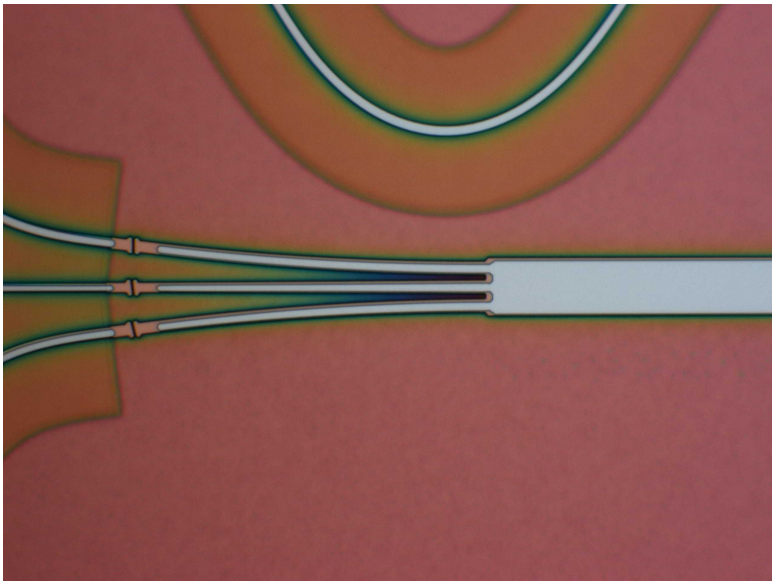

Figure 3.14: Microscope image of a future looped 1-by-3 MMI-based laser showing the oxide opening on top of the ridges

recommended for the photoresist), one can obtain larger features after development. In the case of the oxide opening step, the width of the exposed area is equivalent or larger than the ridge width. As a result, the exposed area overlaps with the floor level on one or both sides of the ridge. After development, the sample is baked at a typical temperature of 150 to 160°C in the case of the photoresist used in this process, for a duration of 10 minutes. This temperature is high enough to melt the photoresist layer and let it reflow in exposed areas, closing the gap at the floor level on the side of the ridge, so that only the top of the ridge is exposed at the end of the reflow process. Additional information on the reflow technique and its uses can be found in [44]. Once the photoresist has been patterned in the desired shape for the oxide opening, the oxide is dry-etched until only a thin layer (typically 20nm) remains in the exposed area. This layer acts as a protective film until the metal lift-off lithography is performed. The opened waveguides can be seen in Figure 3.14.

In order to pattern lines of metal on the sample, a lift-off process is used. Two layers of polymer are successively spun on the sample. The first layer spun on the sample has a higher sensitivity to the developer than the second one, to the point that it will be slowly dissolved by the developer even without having been exposed. After alignment and exposure, the development time is significantly increased compared to standard lithography. As a result, the bottom layer of polymer is fully developed in the exposed areas, and an undercut starts to form

Figure 3.15: Microscope image of undercut photoresist on contact pads - the undercut is visible as the double line on the edges of the opening

where the first polymer layer is dissolved underneath the top layer as shown in Figure 3.15: the undercut appears under a microscope, as a double line at the edge of the photoresist pattern. After the lithography is performed, the sample is exposed to an O_2 plasma for 5 minutes, in order to remove any residual layer of polymer from the exposed area. Once this step is completed, a wet etch of the remaining oxide layer is performed in order to expose the semiconductor itself. Again, an O_2 plasma is used for 5 minutes to further clean the surface of the semiconductor from any residue caused by the wet etch. The sample is then loaded in the metal evaporation tool to create the top-side metal contact pads and lines. In the process described here, the epitaxial structure of the wafer places the P-doped side of the junction on top of the wafer; the bottom substrate being N-doped. As a result, the top-side metal recipe is chosen to ensure good metal-semiconductor contact in a P-doped context.

The metal evaporation recipe consists of an initial layer of titanium (typically 20nm thick), followed by a significantly thicker layer of gold (250nm to 600m thick). The titanium, deposited on a heavily doped semiconductor contact layer, is used to achieve good adhesion between the semiconductor surface and the metal contacts. The gold layer is then deposited to ensure good contact with the probes used to power the sections of the device.

During the metal evaporation, a 360° rotational tool is used to ensure covering of the side walls, to guarantee continuity of the metal lines from the pad to the

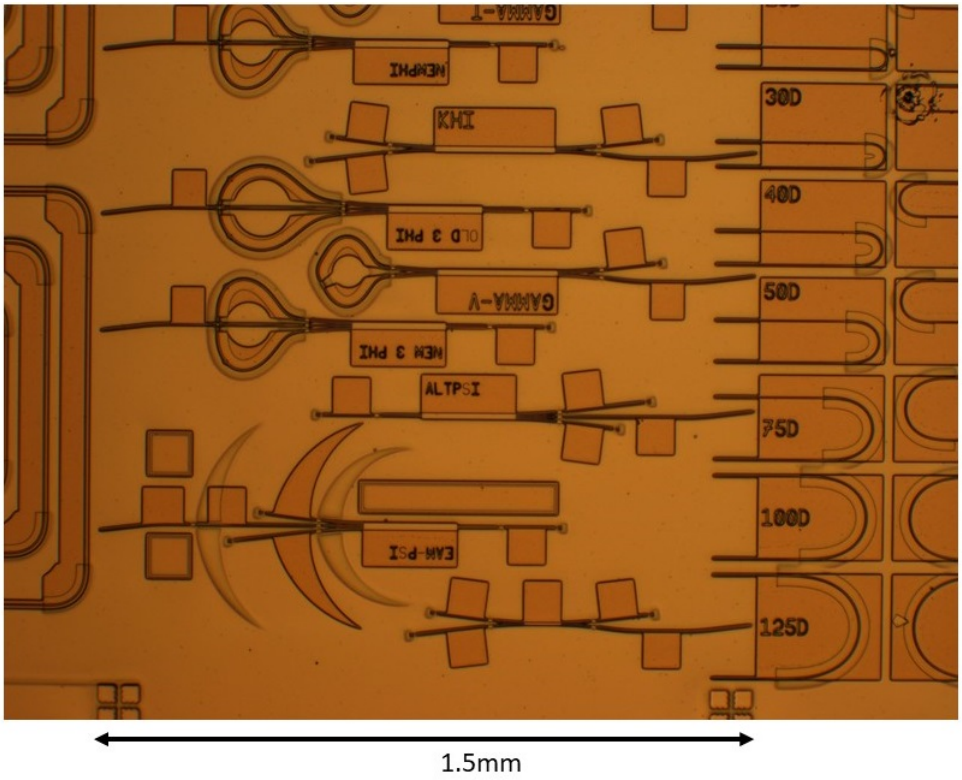

Figure 3.16: Microscope image of a sample after metal evaporation

ridge top. The metal is evaporated on the whole chip as shown in Figure 3.16, both where there still is the photoresist layer and where the sample is directly exposed. However, the undercut formed during the lithography step creates a discontinuity at the edge of the resist, as shown in Figure 3.17. Once the evaporation is complete, the samples are placed in a bath of solvent that dissolves the photoresist. Thanks to the discontinuity at the undercut, the solvent can flow underneath the metal, dissolving the resist. As a result, the unwanted metal is peeled off and removed from the sample, but leaving metal lines and pads on the sample, as shown in Figure 3.18. Once the top-side metal is deposited, the following step is the substrate thinning, followed by the back-side metal deposition.

Before evaporating metal on the back side of the chip to have the ground contact, one has to thin the sample. A thinner sample is easier to cleave accurately, and the thinning also benefits the thermal performance of the sample. By reducing the sample thickness, it is possible to reduce Joule heating that can disrupt the devices, and to ensure all the power is dedicated to powering devices, rather than wasted on counter-productive heating. This thinning is done by exposing the back of the sample to a Bromine-Methanol solution and N_2 bubbles that will

Figure 3.17: Schematic of the metal lift-off resist layout

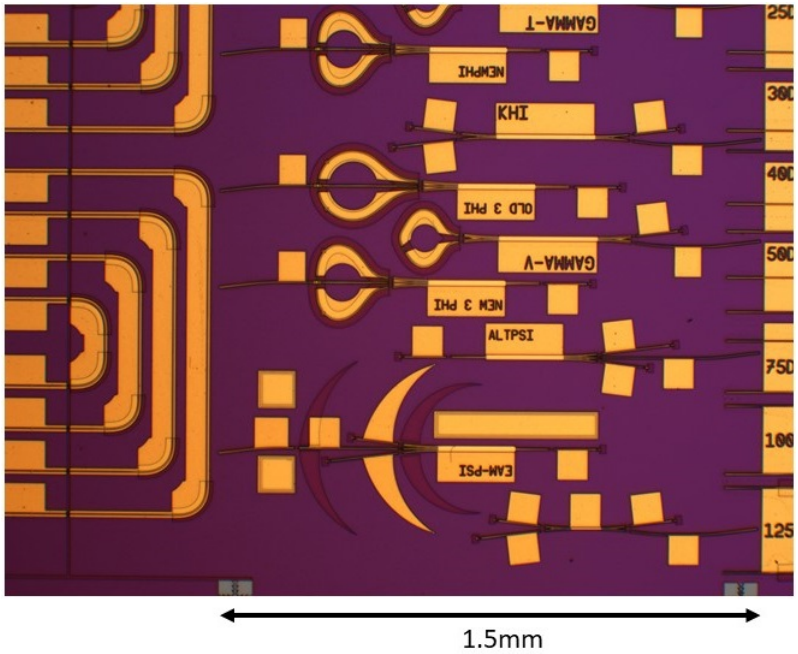

Figure 3.18: Microscope image of a sample after metal lift-off

etch away the excess of substrate. Black wax is melted on a slab of glass, and the sample is placed face-down on this wax. By doing so, the top of the sample is protected by the wax while the back remains exposed. A first mechanical thinning is performed, by rubbing the sample on abrasive material. The purpose is both to initiate the thinning, and to provide a clean, even surface before the chemical thinning. The sample is thinned until it reaches a thickness of 100 to 150μm, and metal is then evaporated on it. The evaporation recipe used for the N contact is Ti:Au (20:250nm). Finally, the sample is removed from the glass slab and wax is cleaned from its surface, using Toluene as a solvent.

At this stage, a contact quality test is performed to verify the low resistivity

of the metal contacts. Should the contact resistivity be too high, a 15-minutes annealing at 380°C is performed to improve the bond quality between the semiconductor and the metal layers.

The last step of the process is the cleaving. A sample under process is typically a quarter of a two-inch wafer, and a large number of devices can be positioned on it. Those devices need to be separated from each other to be studied. This is done by cleaving the sample along predefined marks. To do so, the operator uses a scriber. This tool scribes the surface of the sample using a diamond point, at positions chosen by the operator. By scribing at the edge of the sample, a weakness is created in the crystal structure. It is then possible, by applying a light torque on the sample, to cleave it along a crystal plane, at the position determined by the weakness from where the break will propagate. Each set of devices is then distributed to the different customers, for analysis and characterisation.

Practical considerations for the fabrication of devices

The fabrication process has been heavily streamlined over the years. Indeed, the fabrication time - from initial PECVD to the distribution of the devices - was reduced from more than a month at the beginning of its development, to about a week with a record of 4 days. During the time of this work, some practical difficulties have been encountered and led to significant changes in our fabrication habits. A series of examples will be presented here.

One of the early changes made to the process since we were put in charge of it, concerned the shallow semiconductor etch. Indeed, initially the shallow etch consisted in first a dry etch done by ICP, followed by a short chemical wet etch designed to stop at the etch-stop layer included in the epitaxial structure of the wafer. Although this technique seemed necessary to obtain smooth side walls leading to reduced scattering losses and improved reflectivity for some features, it appeared that there was a risk of undercutting the waveguide, caused by different selectivity levels between the layers of the epitaxial structures, as shown in Figure 3.19. As a result, it was decided that this risk was too important, and a major modification of our process was to remove this wet etch step, relying solely on ICP etch to perform the shallow etch.

Another aspect of the process that required modification was related to the dry etch in general, whether it is the hard mask (oxide or nitride) or the semicon-

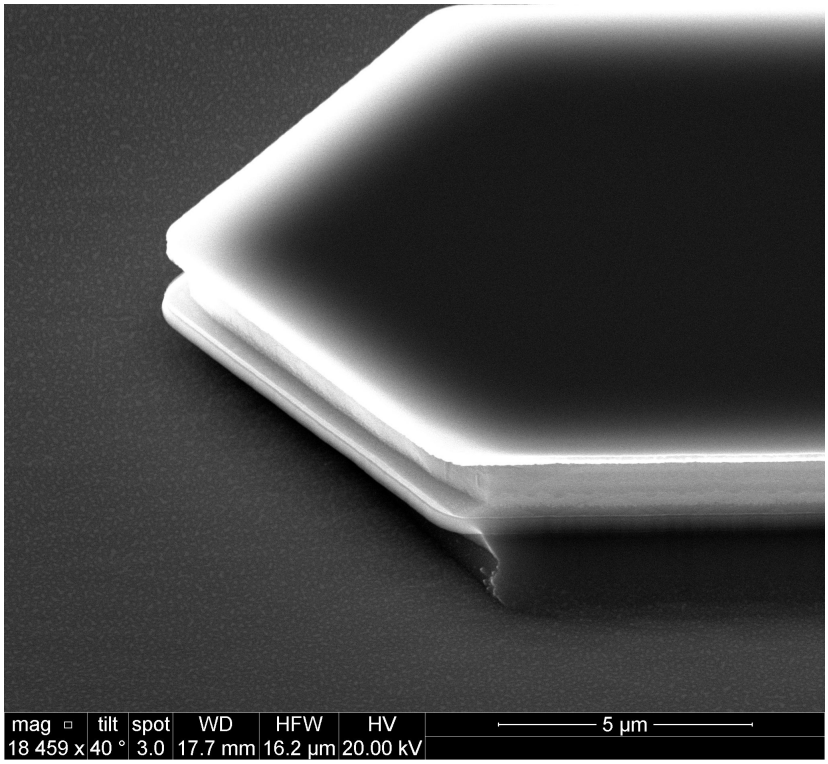

Figure 3.19: SEM picture of an undercut reflective feature showing the different selectivity of the etchant between the different layers

ductor that is etched. In the initial procedure, a preliminary etch was performed on a "dummy sample", a sacrificial fragment of silicon wafer on which oxide or nitride (depending on the layer to be etched) was deposited by PECVD. This was done to estimate the etch rate and from this, estimate the duration required to reach the desired depth on the real sample. However, it has been observed that the etch rate is not necessarily constant, which exposes the sample to multiple risks: an insufficient etch can leave residual layers that will prevent any current from flowing through the sample, and an excessive etch can damage the sensitive surface of the semiconductor material. In the case of the shallow etch, excessive etching might result in a deeper etch that can cause the whole sample to be practically deeply etched, dramatically increasing the waveguide losses and compromising the devices. This is why it appeared necessary to have better ways to monitor the progress of such critical steps.

This was achieved by systematically using a device called an end-point detection (EPD) system consisting of a laser directed at the surface of the sample, and a sensor measuring the intensity of the reflected light. Due to the multiple layers at play, it is possible to achieve interference between the surface and the

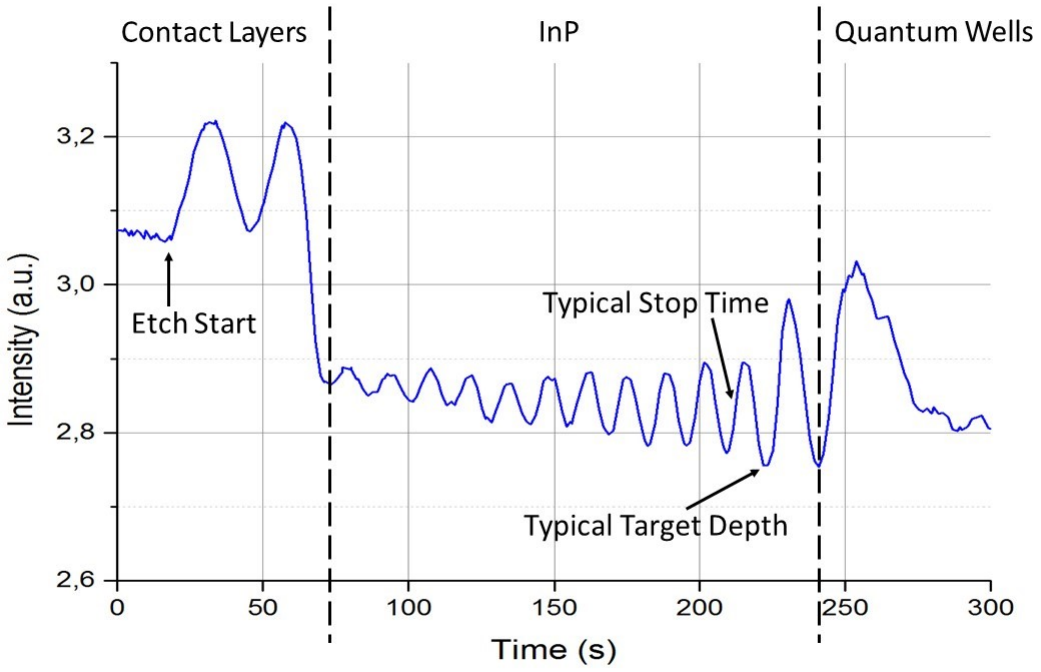

Figure 3.20: EPD reflection graph showing different epitaxial regions, with indications of points of interest for the operator

interface underneath. By monitoring the constructive and destructive interference patterns during the etch, one can interrupt the etch as soon as the target layer is reached. In the case of a partial etch, it was estimated through practice that an accuracy of 50nm can be achieved for hard mask etches, and 50nm to 75nm in the case of semiconductor etches. The reflection profile shown in Figure 3.20 correspond to the ICP etch of a sample past the quantum wells, and indicates the different regions of the epitaxial growth.

It is worth noting that while the oxide or nitride etch processes stop instantly when interrupted on the equipment control interface, this is not the case for the InP semiconductor etch that is performed using different equipment. Indeed, through practice, we estimated that after sending the interruption command, the etch continues for a few seconds, increasing the etch depth by about 100nm. This is the reason why on Figure 3.20, the stop time and final depth are not at the same position. While this figure presents the reflection profile from the surface to below the quantum wells, the "mapping" of this profile was done by partially etching the sample, using a profilometer to determine etch depth, and comparing it with the epitaxial datasheet provided by the manufacturer. By knowing the etch depth and corresponding epitaxial layer, multiple etches

at different depths made it possible to progressively determine what feature of the reflection profile corresponds to which layer of the sample. Through this experiment, it was possible to determine which layer was reached during the etch, thus the different regions highlighted in the figure. For example, in the InP region of the profile, the last fringe shows a wider amplitude. By stopping the etch before and after this feature, the etch depth showed that this fringe occurs immediately after the etch-stop layer is passed. This layer being the target for the shallow etch, it was possible to determine at which point to interrupt the etch to finish within 50nm of this target. It can also be used as a warning sign: when the amplitude is wider, it means that the etch-stop layer has been passed and the etch must be interrupted immediately to avoid reaching the quantum wells.

Another modification of the process has recently been under study, consisting in the deposition of thin metal layer on the surface of the sample, prior to any other processing. There are two main purposes to the modification. The first one is to have a protective layer shielding the sensitive semiconductor surface from potential damage while processing, particularly damage caused by ICP etches, thus maximising the contact quality between the metal layers and the semiconductor.

The second purpose is to mitigate risks associated with the oxide opening step, when the passivation layer is opened on top of the ridge to expose the semiconductor before metal deposition. The risks are related to the lithography and ICP etch steps. The oxide opening definition step is the most challenging lithography of the process, with a misalignment margin smaller than 1μm over the entire sample. Any excessive misalignment causing the floor to be exposed and electrically connected to the top metal, creating a short circuit and disabling the device. In order to mitigate this risk, a solution is to be particularly conservative in the exposure and development parameters to prevent any widening of the opening. This can result in patches of photoresist being left on the ridge, compromising good metal contacts. Indeed, in case of partial contact between the metal and the ridge, the excessive current density through a limited contact area can damage and burn the ridge in a spectacular fashion, as shown in Figure 3.21. If an underlying layer of metal is available, even limited contact between this layer and the final metal deposition allows the current to spread before reaching the semiconductor, reducing risks of overheating.

The presence of an initial metal layer caused us to change parts of the process,

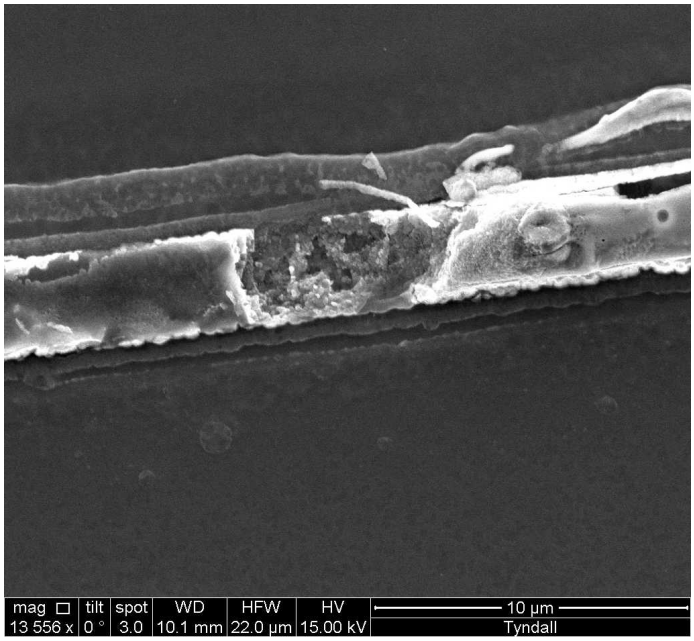

Figure 3.21: SEM picture of a ridge damaged by excessive current density

as follows:

- Deposition of Ti:Au:Ti - 15:30:15nm over the sample;
- PECVD of silicon oxide - 600 to 700nm;
- Ridge lithography and oxide ICP etch under EPD control, followed by photoresist removal;
- PECVD of silicon nitride - 350 to 500nm;;
- Deep area lithography and silicon nitride etch under EPD control, followed by photoresist removal
- Deep area semiconductor ICP etch under EPD control, followed by nitride removal with highly selective ICP etch;
- Shallow semiconductor ICP etch under EPD control, followed by oxide removal with ICP etch. Unlike the regular process, wet chemical etch is not an option here because the etchant (buffered oxide etchant - BOE) also etches titanium at a very high rate;
- Fresh oxide deposition (400 to 500nm);
- Oxide opening lithography and etch. Because the metal can be etched by the oxide etch recipe, EPD control is necessary;

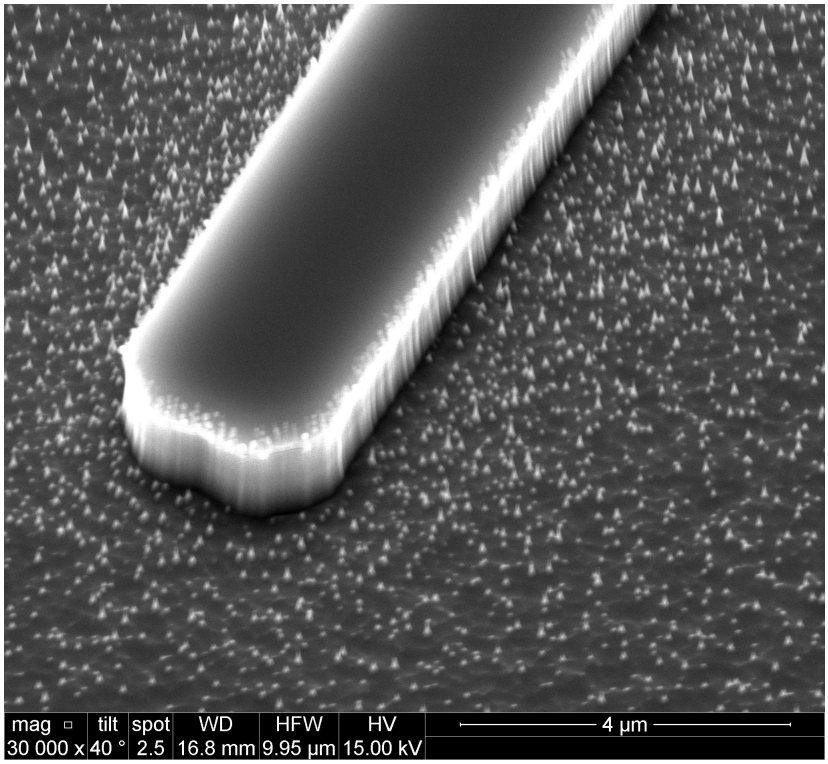

Figure 3.22: SEM picture of a ridge showing metal redeposition after combined oxide and metal etches

- Metal lithography followed by a gentle O_2 plasma for 2 minutes. Again here, the BOE dip step is removed to protect the metal layer;
- Metal evaporation (Ti:Au 20:600nm) and lift-off;
- Backside thinning to a target thickness of 100 to 150μm;
- Backside metal evaporation (Ti:Au 20:250nm)
- Annealing if relevant followed by cleaving and distribution of the samples.

This alternative process is still under refinement, for it comes with some risks. The ICP etch recipe used to etch the initial oxide and the metal layer for the ridge definition is not designed for the etching of heavy species such as gold. As a result, there is a risk of redeposition of some of the metal if it is not evacuated with the gas flow, as illustrated in Figure 3.22.

If too much metal is present on the side walls, this might cause a short circuit preventing the correct flow of the electrons through the ridge and the quantum wells. The presence of the hard layer underneath the oxide, along with redeposition, can also compromise the side wall smoothness. Indeed, it has been

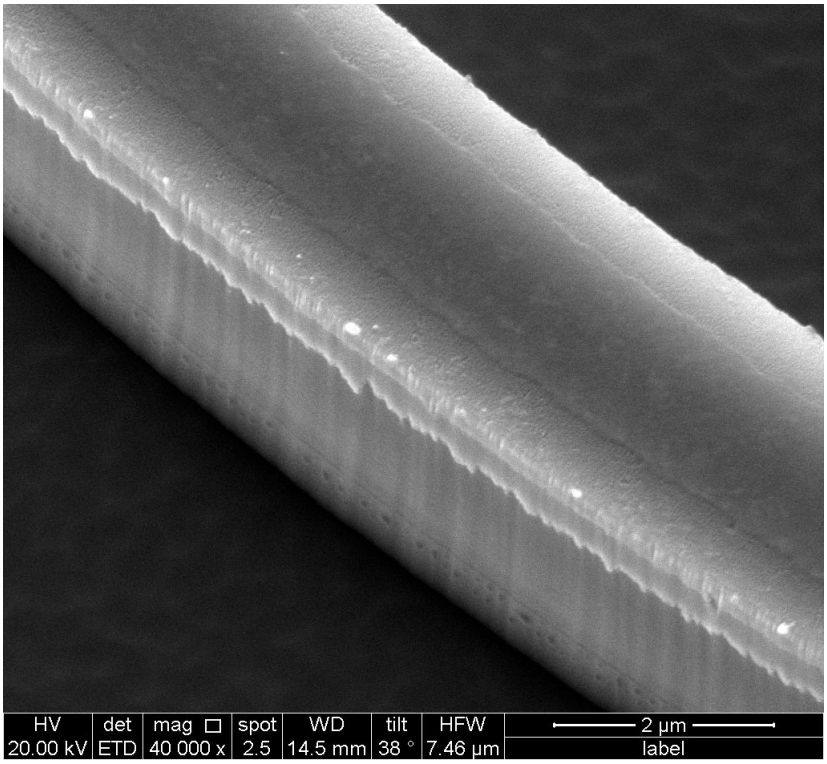

Figure 3.23: SEM picture of a ridge with a smooth side wall and no metal redeposition in the case of a thinner metal layer

observed (see Figure 3.22) that the walls are not as smooth and flat as what can be seen with the intial fabrication process.

A solution found to mitigate the added risks, was to reduce the metal thickness (initially Ti:Au:Ti - 25:50:25nm), to the proposed Ti:Au:Ti - 15:30:15nm recipe, leading to smooth side walls and no noticeable redeposition, as illustrated in Figure 3.23.

Over time, these different modifications to the process have been put in place, contributing to simplifying the fabrication, increase the repeatability of the process results, and generally reducing the overall fabrication time of the samples.

Once the fabrication is completed and the devices are cleaved, they are distributed to the different members of the group for characterisation, where the devices are powered and their performance is studied. In the following section, elements of the characterisation setup used in this work will be detailed, and the characterisation procedure will be described.

3.7 Typical characterisation process

The cleaved samples are placed on a temperature controlled chuck, and the different sections of the device under test are powered. The emitted light is collected by the means of a fibre and analysed using different tools.

3.7.1 Characterisation setup

Once the samples are cleaved and brought to the characterisation lab, they are placed in the characterisation setup shown in Figure 3.24. This setup includes a central temperature-controlled brass chuck. The chuck can be maintained at constant temperature by the means of a thermoelectric cooler (TEC), positioned between the chuck and an aluminum block used as a heat-sink. The chuck - TEC - heat-sink group is fixed to a translation stage to facilitate the alignment of the different setup components.

A U-shaped metal bracket is bolted to the table, kept slightly above the chuck by the means of fixed legs. This bracket is used to place the probe systems around the chuck, in order to reach the sample from any desired direction. A probe system consists in a X-Y-Z translation stage holding an arm terminated by a needle that comes in contact with the sample. The base of the translation stage is covered with a magnetic layer to secure it on the metal bracket and avoid accidental movement of the probe. Each of those units is fitted with a set of two coaxial connectors to connect the probe to current sources, and to enable 4-wire measurement, should the need arise.

The current sources used to power the different sections of the devices are commercial devices when high accuracy or advanced control are needed. When a resolution of 1mA or larger is acceptable for the needs of the characterisation, a set of custom current sources is used, that were fabricated at a fraction of the cost of a commercial device. Two sets of those custom current sources can be seen on each side of the U-bracket in Figure 3.24, they can be recognised by the set of four golden SubMiniature version A (SMA) connectors on each board. When the current sources are in use, a compliance voltage is set, typically at 3V, to prevent damage to the sample due to excessive currents being injected as a result of an intermittent contact.

Under the bracket, on both sides of the chuck, X-Y-Z translation stages are po-

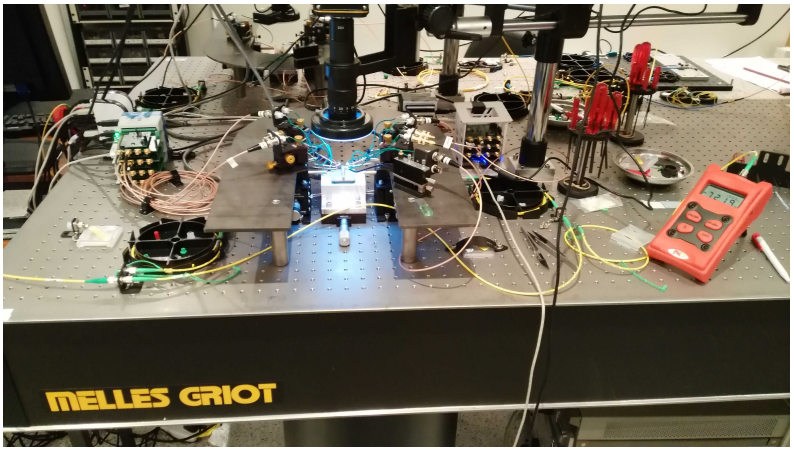

Figure 3.24: Characterisation setup including a central chuck, contact probes, microscope camera, current sources and a power meter

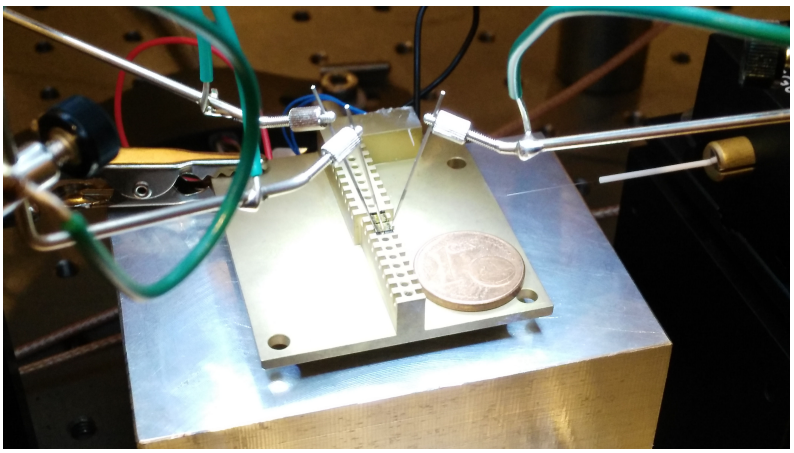

Figure 3.25: Photograph of a chip on the chuck, with probes and a lensed fibre. €0.01 coin for scale.

sitioned. They are equipped with a holder system to secure the fibres that are used to collect the light emitted by the sample, or to inject light into it. The translation stages enable fine adjustment of the fibre's position relative to the sample, to maximise the coupling. Figure 3.25 shows a lensed fibre on the right of the image, kept away from the sample until the probes are positioned to avoid damaging this fragile component.

Directly above the chuck, a microscope and digital camera are positioned. The purpose of the system is double: to enable probing the sample with an accuracy the naked eye cannot achieve (the target contact pads are typically 90μm by 90μm squares), and to avoid direct observation of the samples at a close range. Indeed, once the devices are powered, they emit light that can be invisi-

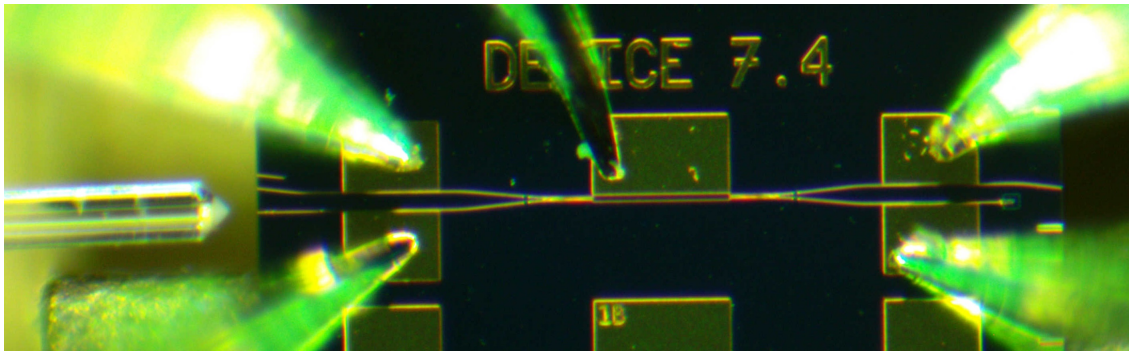

Figure 3.26: Detail of a device under test with probes and a coupling fibre

ble (in the case of this work, the emission wavelength is 1500nm to 1600nm). Although the beam divergence is high and the output power is low, making the regulatory safety distance required less than 5cm, the microscope view offers further protection by removing the need to look at the sample once it is powered. A view of the sample under test, taken using the microscope system, can be seen in Figure 3.26. It is noteworthy that the microscope is connected to the digital camera only and presents no eyepiece for direct observation by the operator. This additional safety measure is to ensure there is no risk of laser emissions being focused into the eye of the operator via the microscope, potentially harming them.

The collection fibres can be connected to a variety of devices to perform different measurements. One of the first devices used is a power meter that is monitored while adjusting the fibre's position, until maximum coupling is achieved. The device characterisation can be then performed.

3.7.2 Device characterisation

In this work, the focus is on the design of tunable single-mode lasers. As a result, the main data collected from devices is spectral information. This is done by using an optical spectrum analyser (OSA), connected to a computer. The laser emission spectra are recorded, and the focus of the analysis is on the tuning range and the side-mode suppression ratio (SMSR), used to determine the quality of the single mode: for optical communications, an SMSR of 30dB is commonly considered the minimum requirement.

Before powering the devices that can be complex and require several current sources, Current-Voltage curves (I-V curves) are taken to verify the good work-

ing of the device section. It is done by powering the target section of the device by the means of a current source, and scanning over a range of currents, typically from 0mA to 150mA. A typical diode behavior is expected, showing a steep voltage slope at low currents, until the turn-on voltage is reached. For currents higher than this point, the voltage slope is expected to be greatly reduced, leading to a linear behavior due to the internal resistance of the device. In order to verify the good health of the section, different features are checked on the IV-curve:

- the diode behavior: its absence would suggest damage to the semiconductor junction,
- the turn-on voltage: in the case of this work, it should be around 0.8V,
- the device resistance: experience shows that any section longer than 100μm should be able to sustain at least 75mA before reaching dangerously high voltages (2.5V and higher). Some wide sections have been seen to sustain several hundreds of mA. In the opposite fashion, a low resistance could suggest current leakage where it should be confined by the ridge structure.

If the devices show the expected behavior, all the contact probes are set in position to power the entire device. The collection fibre is brought at the level of the output coupler and the testing itself can start.

Once the device is powered and the emitted light is coupled into the collection fibre, the emission power can constantly be monitored by the means of an in-line power meter. It is also used to adjust the position of the collection fibre in case of a drift in its position, which could be caused by vibrations in the setup or temperature variations. In the case of the devices presented in this work, the power coupled into the fibre is in the range of -20dBm to 0dBm (10μW to 1mW).

Once as much power as possible is coupled into the collection fibre, it can be connected to a variety of systems to perform different measurements. The main one used in this work is the OSA that records the emission spectrum of the device. The sections are powered with different combinations of injection currents, and the emission spectra can be recorded. An example of emission spectrum can be seen in Figure 3.27. The primary feature that is examined in the spectrum is the SMSR to determine the quality of the single-mode behavior.

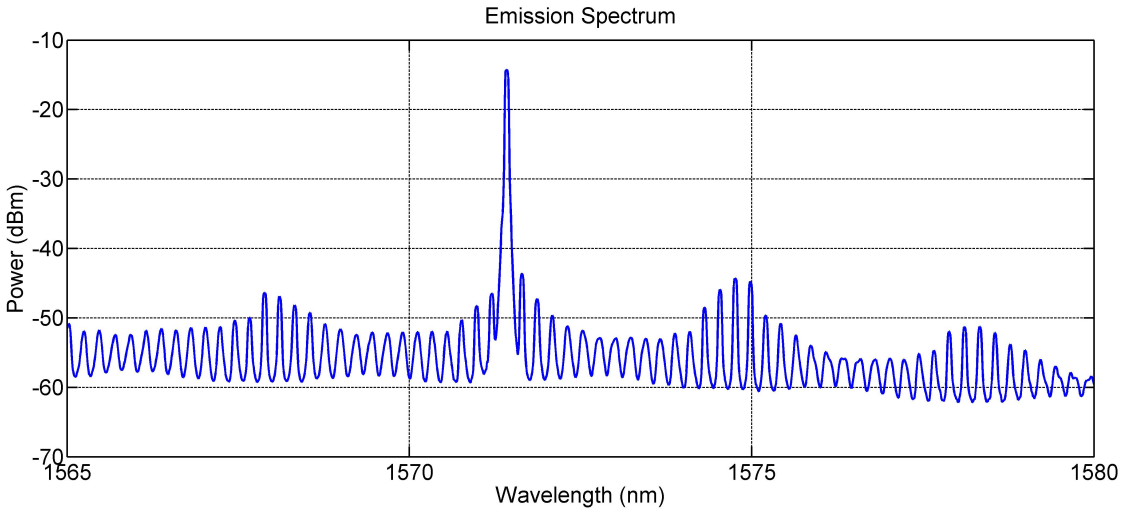

Figure 3.27: Example of laser emission spectrum graph

Another spectral feature studied is the spacing between the modes, and between the super-modes in the case of multi-cavity structures. Indeed, by the means of a fast Fourier transform algorithm (FFT), it is possible to extract data from the spectrum, such as the length of the cavity (or cavities) used in the design. The output of this algorithm, shown in Figure 3.28, can be used to identify the cavity and sub-cavity lengths leading to the obtained spectrum. This information can be used to refine the simulation models, by finely adjusting the simulated refraction index to better match the simulation and the reality for future designs. For dimension-sensitive sections such as MMI couplers, reflections caused by inadequate dimensions can appear on this plot, and thus be used to refine the design of the next iterations.

The tunability of the device can also be assessed by the means of the OSA. By varying the current injected in the different sections of the device, one can achieve different lasing wavelengths. By recording the emission spectra in multiple configurations (see Figure 3.29), the tuning range of the device under test can be determined. As a rule of thumb, increasing the current injected in the different sections leads to an increase in lasing wavelength. However, the further away from the natural bandgap of the material, the less likely it is to obtain satisfying emission power and SMSR. In this work, the widest tuning range achieved spanned from 1564nm to 1611nm, or 47nm. For simple lasers with one or two sections, tuning maps are a common way of showing the behaviour of the laser. In this work, the proposed lasers are complex with multiple sections, making it impractical to present tuning maps. However, a tuning strategy

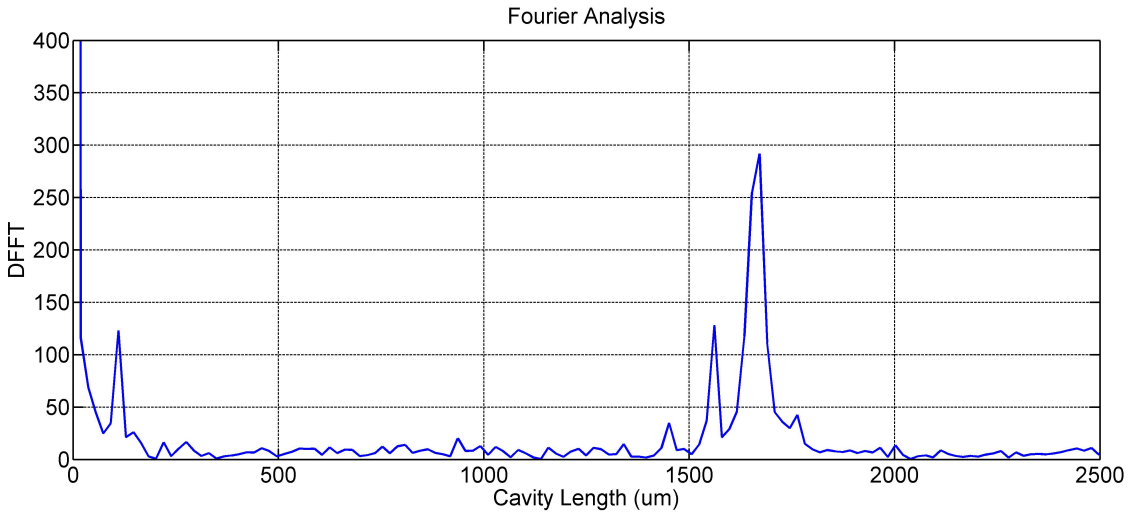

Figure 3.28: Graph of the FFT analysis of a laser emission spectrum, showing peaks at lengths corresponding to the resonating cavities present in the device

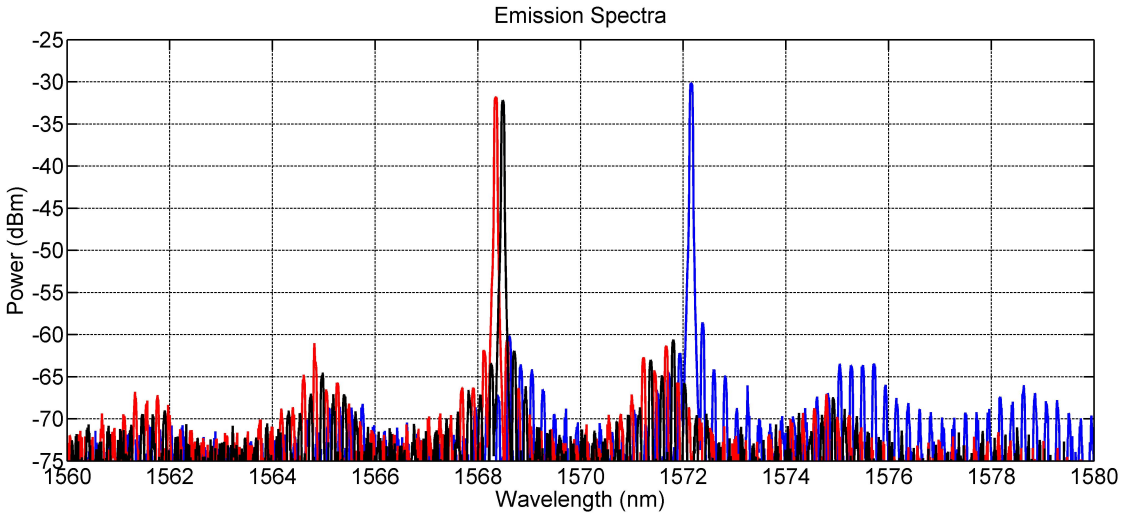

Figure 3.29: Superimposed laser emission spectra from a single device for different combinations of injected currents

can be devised.

Another element of interest is the linewidth of the laser. It corresponds to the width of the emission around the lasing wavelength, and can be caused by a large variety of factors, notably the remaining spontaneous emission that generates noise around the lasing wavelength [45, 46]. Another source of noise in the system is the current source powering the laser: a not completely steady current injection will broaden the linewidth of the laser. The linewidth cannot be obtained by the means of standard OSAs that don't have the resolution required

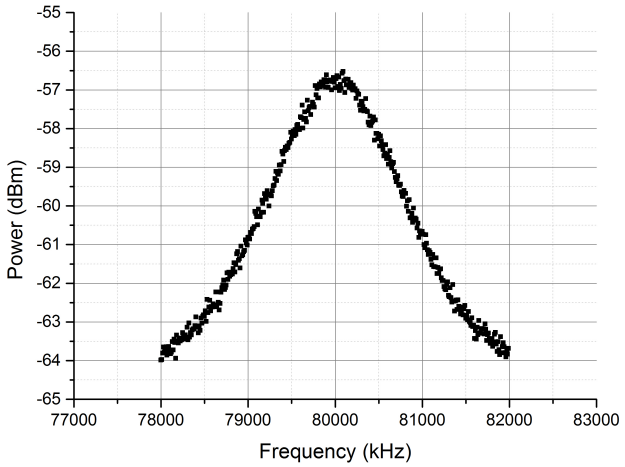

Figure 3.30: ESA data used to determine the laser linewidth - the linewidth corresponds to half the width of the curve at 3dB below maximum

to determine the spectral width of the laser emission. A delayed self-heterodyne technique is used [47] to obtain this information. The primary elements of this system are the following. The laser light is split between two branches. One of them includes a 50km fibre reel used as a delay to ensure that the signals are no longer coherent with each other once recombined. One of the branches also includes an acoutso-optical frequency shifter (AOFS) set at 80MHz and used to shift the signal frequency in the branch. The two signals are then recombined and received by a photodiode. The electric current generated by the photodiode is then spectrally analysed by the means of an electrical spectrum analyser (ESA). The ESA data can be seen on Figure 3.30. The signal shows a peak around 80MHz caused by the AOFS. The width of the signal around this central frequency can be used to determine the linewidth of the laser: it is equal to one half of the full-width at half-maximum (FHWM) of the peak.

Once the devices are characterised and their performance determined, the information gathered during this step is used to refine and improve the next generation of devices. This improvement can be in the form of modifications to the device geometry, as well as changes in the fabrication process when problems are observed systematically on multiple samples from different researchers.

3.8 Summary of the proposed methodology

A large number of well-established semiconductor lasers are available, as shown in the previous sections. However, most rely on the usage of gratings to obtain single-mode behavior. Such gratings often require multiple epitaxial growth steps that increase the fabrication time and cost. In addition to the regrowth, the usage of advanced lithography techniques such as electron-beam or holographic lithography also has a significant impact, increasing the cost of fabrication and in the case of the electron-beam, the time taken to obtain fully functional devices. A means to avoid the usage of such processes, is to achieve single-mode lasing by including slots in the design, removing the need for regrowth and advanced lithography. However, the slots are highly sensitive to the etch depth, reducing the repeatability of the process. Moreover, while the usage of multiple slots in a high-order grating allows the design of cleave-free mirrors, this multiplies the problem of the repeatability.

The limitations presented above have the direct consequence of reducing the industrial attractiveness of the semiconductor lasers currently in use. In order to propose industrially attractive lasers where the fabrication time and cost are kept minimal, this work presents the development of a series of lasers designed to remove or reduce the usage of techniques and features that could negatively impact the fabrication efficiency. The development aimed at removing the need for gratings, regrowth, or any advanced lithography. The usage of slots was kept minimal to reduce the dependence of the lasers to this source of repeatability issues. In order to facilitate integration, the proposed lasers were kept cleave-free.

Several generation of devices were designed, resulting in a portfolio of lasers where single-mode and tunability were achieved by combining multiple cavities of different lengths, while using on-chip reflective features to remove the need for cleaved facets. This work was done over several cycles of design and simulation, fabrication, and characterisation of multiple device generations. The knowledge acquired by characterising one generation was used to refine the design and simulation of the next in an iterative approach. Ultimately, proofs of concepts were designed, fabricated and tested where the most promising designs were monolithically integrated with modulators and optical comb generation sections. The resulting photonic integrated circuits formed regrowth-free, grating-free units with minimised usage of slots and reduced fabrication

complexity, in an industry-friendly approach contributing to the development of solutions to match the ever increasing demand for photonic components.

Chapter 4

First generation of lasers

4.1 Design and purpose

The development of single-mode tunable lasers was done incrementally, and was based on the principle of coupling several cavities of different lengths to achieve single-mode behavior. The technology that was adopted to achieve coupling between different cavities was the MMI coupler [28], using the self-imaging properties of wide waveguides to split input signals between several output ports. The extensive mathematical analysis of such structures [48] enabled the simulation of the MMI couplers and include them in an SMM-based model.

The additional constraint brought by the need to develop integration-friendly devices, was the necessity to not rely on cleaved facets to achieve reflection. Indeed, in the case of highly complex photonic circuits, the requirement for a cleaved facet puts an additional constraint to the overall design of the circuit. In order to overcome this constraint, deeply etched multimode interference reflectors (MIR) [49] were used to achieve reflection without using cleaved facets.

The first iteration in the development process was focused on validating the design of MMI couplers and MIRs. Several devices were designed, based on a 2-by-2 MMI coupler, each of its ports being connected to a waveguide. Some of those arms were terminated by MIRs, while the others reached the cleave plane, either at normal incidence to achieve reflection, or at an angle to avoid it. Variations on the number of reflectors were done to assess different elements of performance. The 1-reflector structure (Figure 4.1) was designed to validate

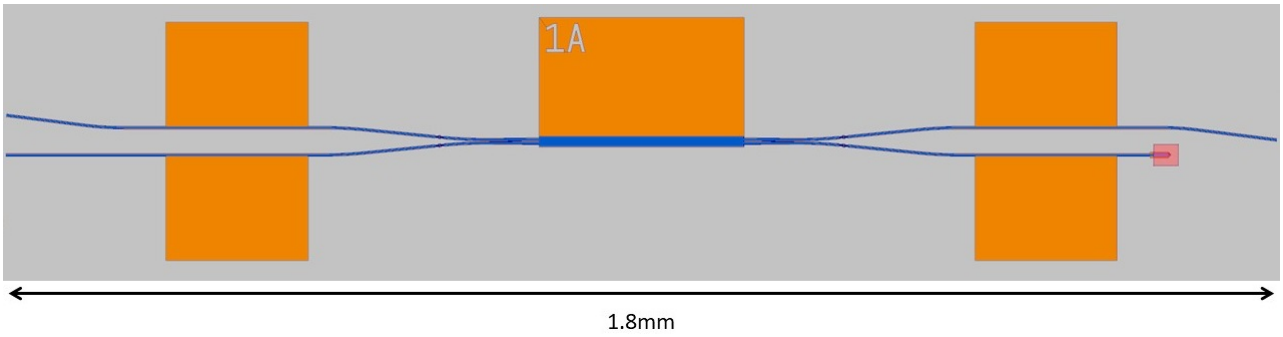

Figure 4.1: One-reflector structure schematic for validating the MMI dimensions - the ridges and MMI sections are in blue, the metal in orange and the deeply etched sections in red

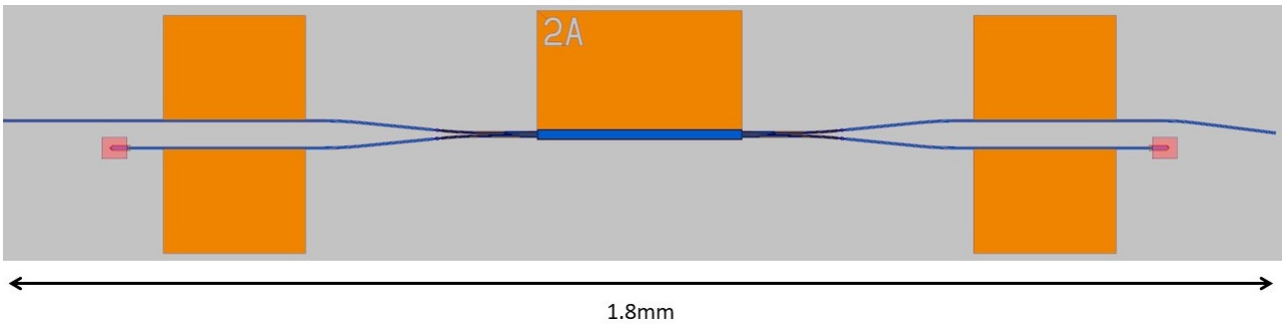

Figure 4.2: Two-reflectors structure schematic for validating the MIRs to create a cavity

the equal splitting of the light by the MMI coupler. The 2-reflector structure (Figure 4.2) was designed to assess if lasing was achievable in a cavity defined by two MIRs. The 3-reflector structure (Figure 4.3) was designed as an initial attempt for a double-cavity MMI-based laser. The normal incidence of the output arm was chosen to obtain a reflection after a different path length, leading to a difference between the lengths of the coupled cavities, and thus favouring single-mode behaviour.

The large number of different sections for these devices implied the use of 5 different pads per laser for current injection. This large number of pads would be challenging for testing the devices, which is why a set of devices (Figure 4.4) was designed where several sections were electrically connected to the same pad, in order to reduce the characterisation procedure's complexity.

The different sections of the devices were isolated from each other by the means of angled slots. Variations were included with deep or shallow etched slots to compare the isolation performance in each case.

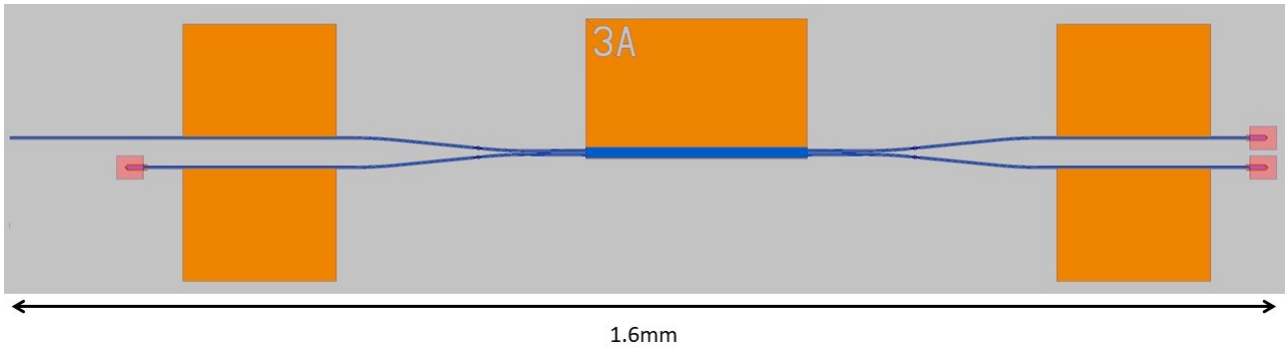

Figure 4.3: Three-reflectors structure schematic for an early attempt at a dual cavity MMI laser

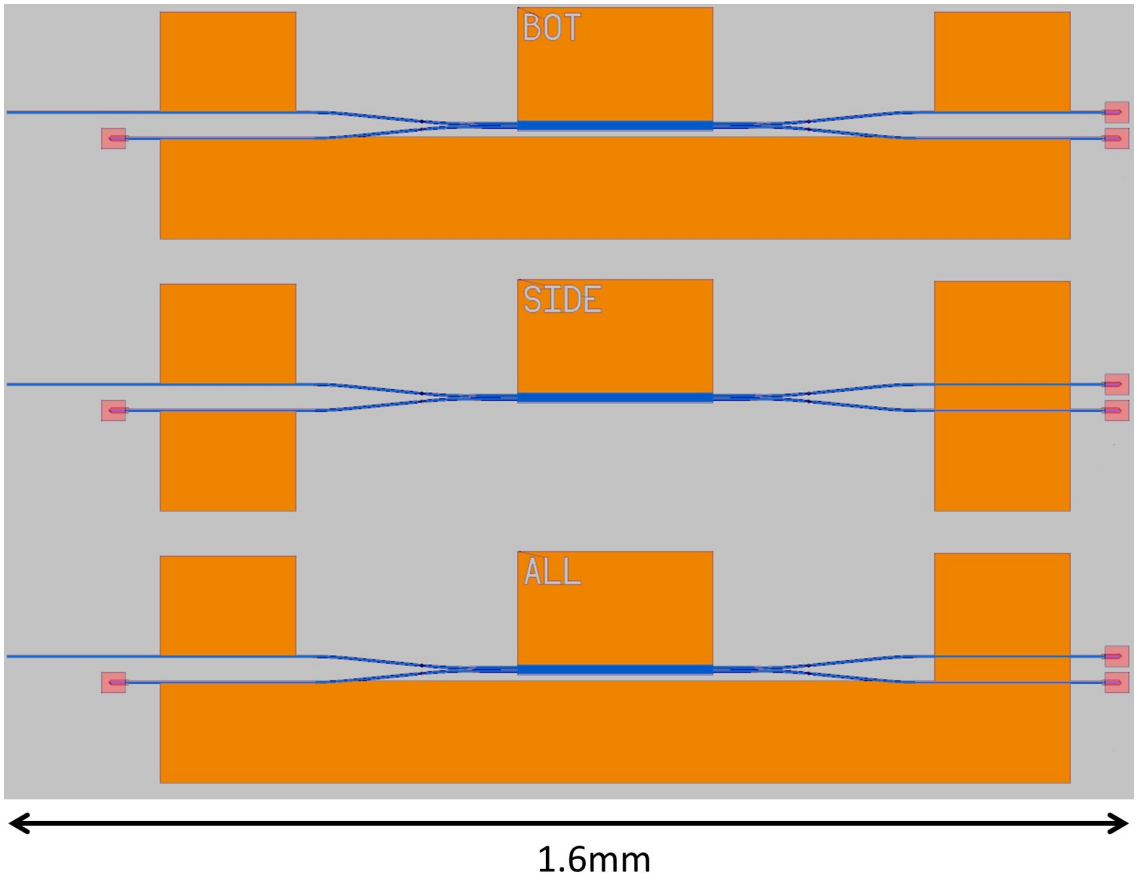

Figure 4.4: Device schematics for alternative contact configurations to facilitate the powering of the laser

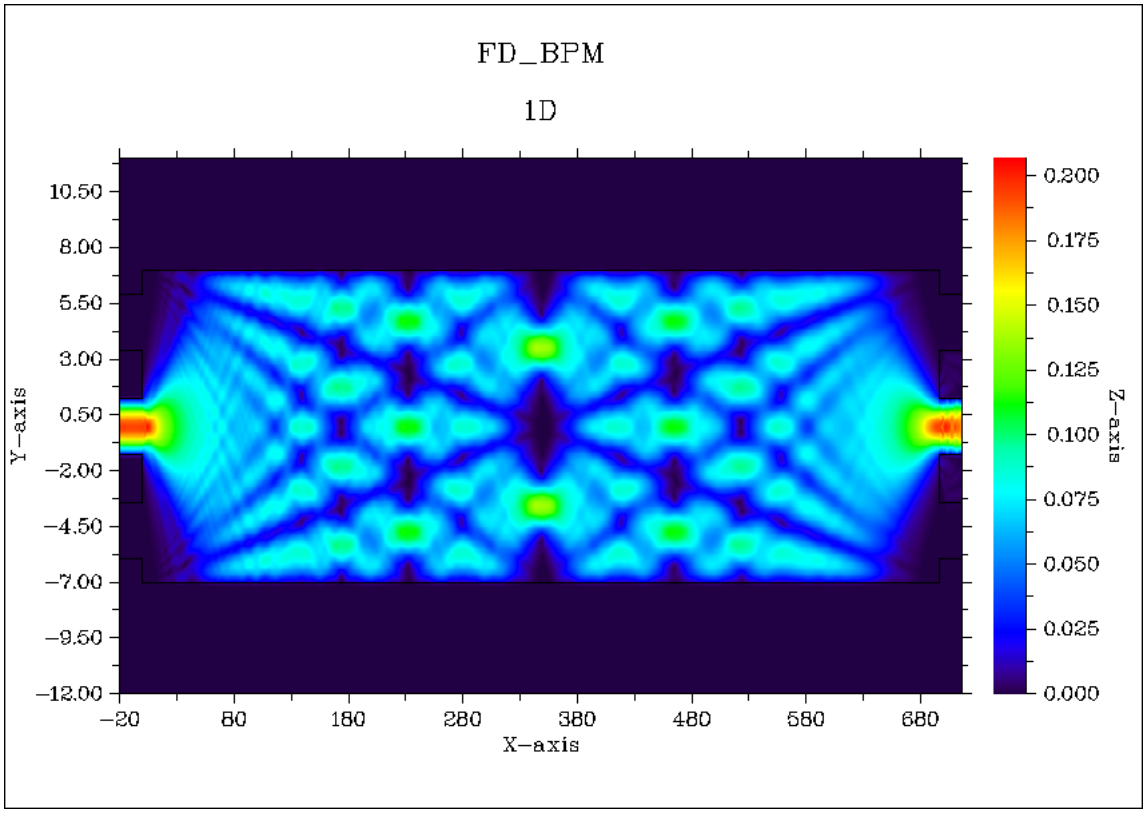

Figure 4.5: Simulated signal propagation through a 696μm long and 14 μm wide MMI coupler at 1550nm illustrating the self-imaging properties of an MMI, and points of interest along the path.

4.2 The multimode interference coupler

The MMI coupler is at the core of the designs proposed in this work. It consists in a wide rectangular waveguide, and originates in the idea of a confined Talbot effect [50]. Indeed, Talbot observed that if an optical plane wave of given wavelength is incident upon a periodic diffraction grating, then the image of the grating will repeat itself at a fixed distance away from the diffraction grating. This observation was later expanded to the imaging of two-dimensional images [51]. It was then proposed to use the total internal reflection of an optical fibre as a substitute to the grating to obtain confined Tablot effect [52]. Since the experimental validation of an MMI based on this effect, this class of devices has been widely used in PICs.

The simulation of a beam propagation through an MMI structure is illustrated in Figure 4.5. The self-imaging principle is illustrated where the beam is injected from the left, travels through the MMI, and is reconstructed at the right

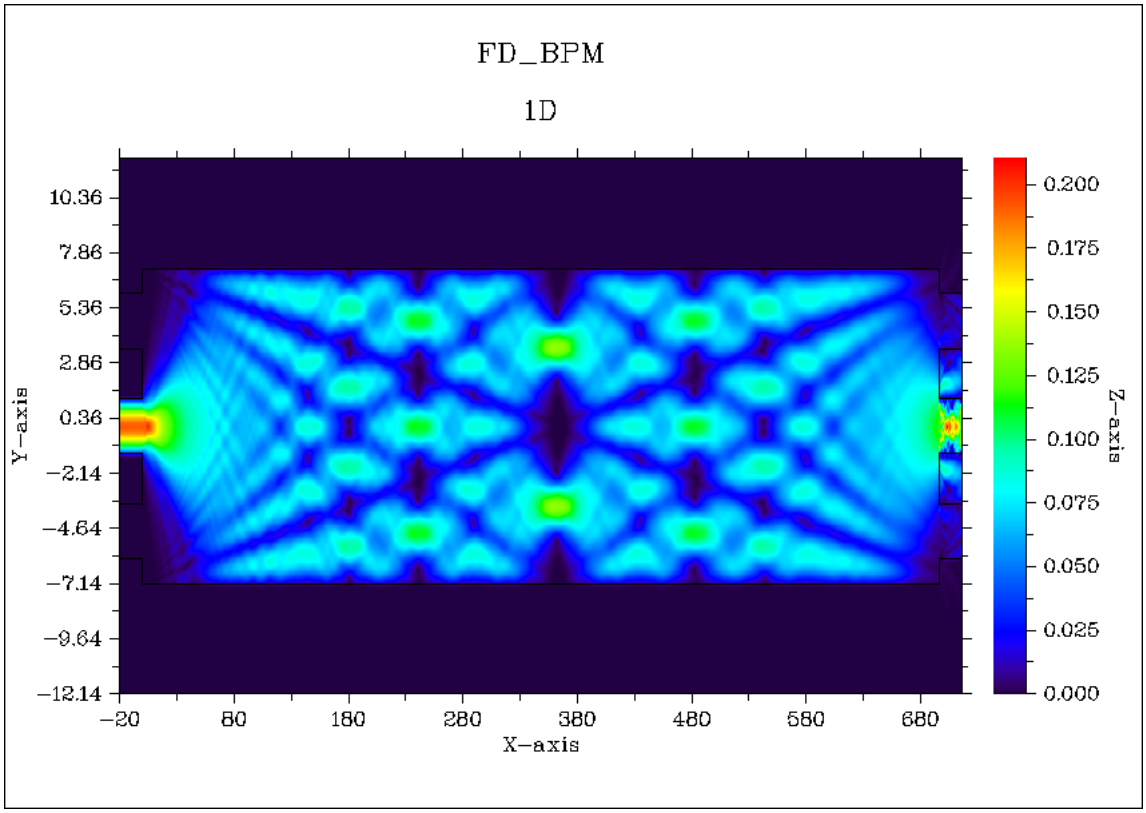

Figure 4.6: Simulated signal propagation through a 696μm by 14.28μm MMI coupler at 1550nm illustrating the sensitivity of MMIs to width variation.

side port. Some points of interest can be observed along the propagation path, particularly at 1/4, 1/3, 1/2, 2/3 and 3/4 of the MMI length where the optical signal converges to respectively 4, 3, 2, 3 and 4 positions where the power is equally split. This observation lead to the development of splitters, by terminating the MMI at these positions and positioning the ports at the correct position to collect the part of the signal converging there. Another class of MMIs that was proposed is the multi-port MMI coupler, with multiple input and output ports. By using the points of interest indicated above to obtain for example a 2-by-2 structure, one can obtain the parallel coupling of cavities, leading to the structures used in this work that use the 2-by-2 for this generation, and the 3-by-3 configuration later. Extensive information on the underlying mathematics of the MMI structures can be found in [48].

The beam propagation simulation also allows the study of the effect of fabrication imperfections on the MMI performance. Figures 4.6 and 4.7 show the simulated signal propagation where respectively the width and length of the MMI have been altered by 2% compared to the initial scenario. It shows that

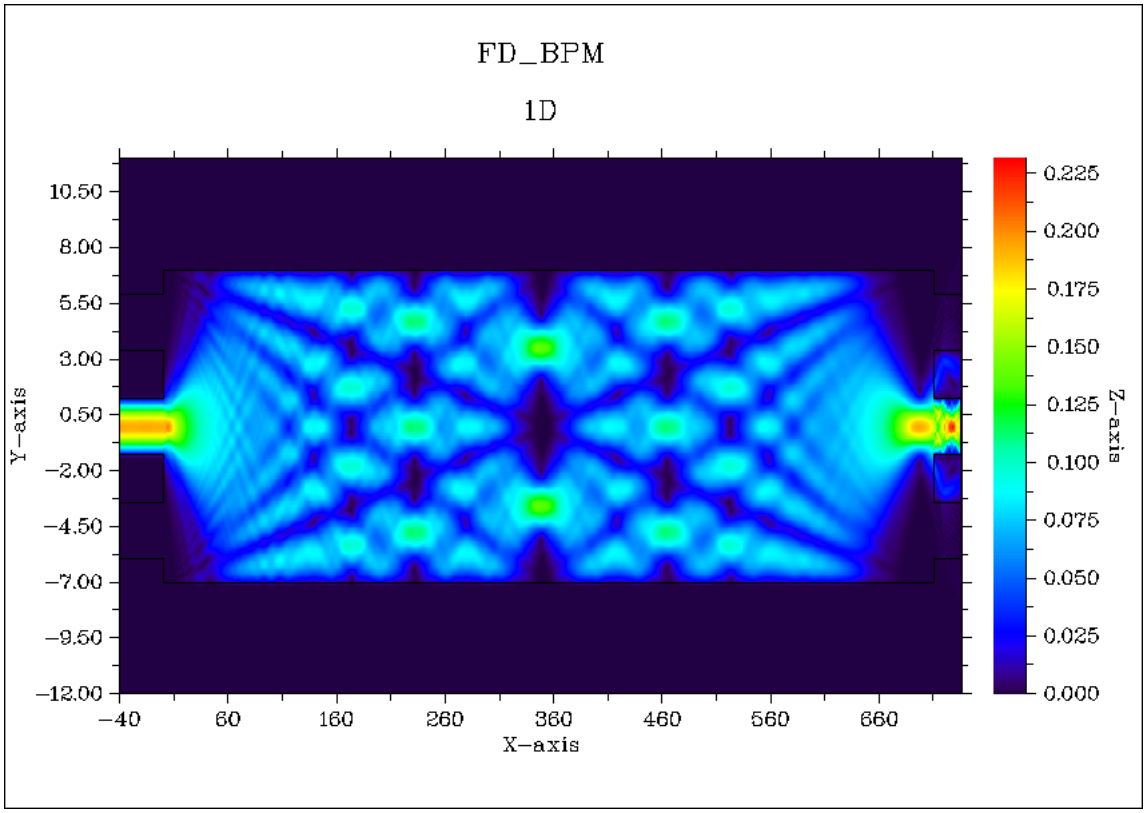

Figure 4.7: Simulated signal propagation through a 709.9μm by 14μm MMI coupler at 1550nm illustrating the robustness of MMIs to length variation.

the MMI is sensitive to width variation, but robust to length variation. It is to be noted that the fabrication procedures lead to an uncertainty of typically 0.1μm for waveguide dimensions. The simulation (Figure 4.8) of a MMI with a 0.14μm (1%) variation from the initial scenario shows that a significant portion of the signal is still coupled into the output port, suggesting that MMI couplers, although sensitive to width variation, are robust enough to be reliable when fabricated with the procedures used in this work.

4.3 Device simulation

The 3-reflector structure was simulated by using the SMM, combined with the known properties of the 2-by-2 MMI coupler that were used to generate the transfer functions associated with it, representing the splitting of an input signal between the two outputs, and the phase shift caused by the coupler. The whole structure is considered as a one-port system, corresponding to the output arm. The corresponding transfer function thus represents the reflectivity of

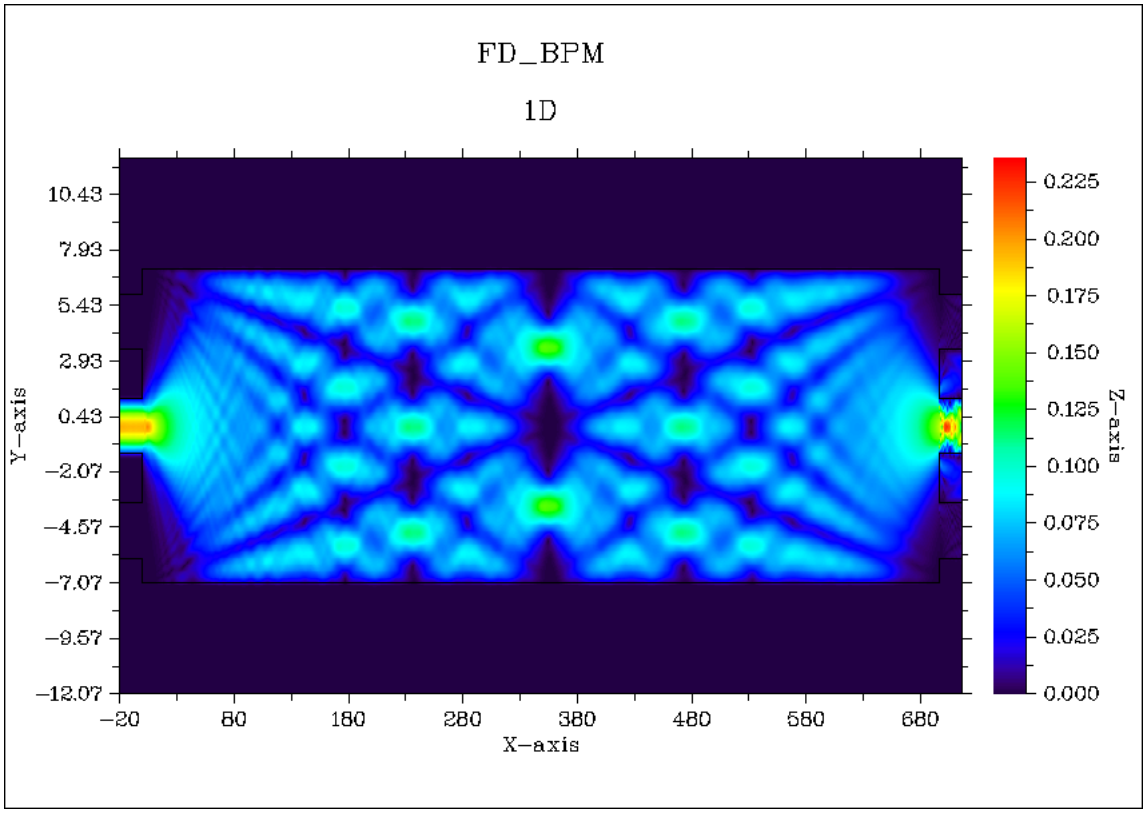

Figure 4.8: Simulated signal propagation through a 696μm by 14.14μm MMI coupler at 1550nm for realistic fabrication uncertainty.

Figure 4.9: Schematic structure studied consisting in a 2x2 coupler and four arms, arm 3 being the input port in this study

the structure, which is related to the expected output spectrum. When the reflectivity of the structure is high at a given wavelength, this wavelength is more likely to be sustained in the structure, leading to lasing. The schematic structure shown in Figure 4.9 presents a generic configuration where the MMI coupler is linked to four arms that are disconnected from each other. Considering the arm labeled 3 to be the input/output port of the whole structure, and the arms 1, 2 and 4 to be waveguides of known length terminated by a reflective element, it is possible to derive the transfer function of the structure.

For the following calculation, no gain or loss was considered, and it was as-

sumed that the MMI coupler was perfect, equally splitting an input between the two output ports.

The first step in the calculation was to determine the transfer functions associated with the arms 1, 2 and 4. These can be derived from the scattering matrix method.

Let λ be the wavelength of the considered signal. Let $L_k, n_k, g_k(\lambda)$ be respectively the length, refractive index and gain profile of the arm labeled k. Let $f_k(\lambda)$ be its transfer function, $\mathbf{S}_k$ and $\mathbf{T}_k$ its associated scattering matrix, corresponding to a waveguide segment terminated by a reflective interface of coefficients r_k and t_k. For this step, the arm is considered as a two-port system, the first port in the propagation direction being the link to the MMI, and the second one being the reflective termination. The desired transfer function is related to the first port, as the behavior of the MMI will be studied based on the inputs and outputs at each of its ports. One can write:

$$\mathbf{T}_k = \frac{1}{t_k}\begin{pmatrix} 1 & r_k \\ r_k & 1 \end{pmatrix} \times \begin{pmatrix} e^{j\phi} & 0 \\ 0 & e^{-j\phi} \end{pmatrix} \tag{4.1}$$

$$\mathbf{T}_k = \frac{1}{t_k}\begin{pmatrix} e^{j\phi} & r_k e^{j\phi} \\ r_k e^{-j\phi} & e^{-j\phi} \end{pmatrix}, \tag{4.2}$$

where $\phi = 2n_k\pi\frac{L_k}{\lambda} + jg_k\lambda L_k$ is the phase shift and amplitude gain induced by the length of the arm. One can thus calculate the scattering matrix for the arm:

$$\mathbf{S}_k = \begin{pmatrix} r_k e^{-2j\phi} & t_k e^{-j\phi} \\ t_k e^{-j\phi} & -r_k \end{pmatrix}, \tag{4.3}$$

From this equation, it is possible to obtain the transfer function related to the MMI side of the arm. Due to the model chosen for this calculation, the transfer function is the top-left coefficient of the scattering matrix. One can thus write:

$$f_k(\lambda) = r_k e^{-4jn_k\pi\frac{L_k}{\lambda}} e^{2g_k\lambda L_k} \tag{4.4}$$

Once the transfer functions associated to the reflector arms of the structure have been determined, it is possible to study the MMI itself. For this calculation, the MMI will be modeled as a waveguide of known length, where any signal entering a port will be equally split between the two opposite ports, with an adequate phase change. In order to reduce the complexity of the calculation, no ampli-

tude variation through material absorption or gain was considered ($g_k(\lambda) = 0$). In this model, the MMI is assumed to be perfect, splitting the input perfectly between the output ports.

One can thus consider two functions to represent the MMI, one related to the transmission (i.e. from port 1 to port 3), and one related to the coupling (i.e. from port 1 to port 4). Those functions will respectively be called $t_{MMI}(\lambda)$ and $c_{MMI}(\lambda)$. The phase changes for both cases involve the following quantities:

$$\delta\beta_0 = \frac{3\pi^2}{2n_{MMI}k_0W_{MMI}^2} \tag{4.5}$$

$$\beta_0 = n_{MMI}k_0 - \delta\beta_0 \tag{4.6}$$

$$\phi_0 = -\beta_0 L_{MMI} - \frac{3\pi}{4}, \tag{4.7}$$

where n_{MMI} is the MMI coupler's refractive index, $k_0 = \frac{2\pi}{\lambda}$ the wavenumber and W_{MMI} and L_{MMI} respectively the width and length of the MMI coupler. The phase shift expression for transmitted and coupled signals can then be written:

$$\phi_t = \phi_0 + \frac{\pi}{2}, \tag{4.8}$$

$$\phi_c = \phi_0 + \pi, \tag{4.9}$$

thus the MMI functions:

$$t_{MMI}(\lambda) = \frac{1}{\sqrt{2}}e^{j\phi_t} \tag{4.10}$$

$$c_{MMI}(\lambda) = \frac{1}{\sqrt{2}}e^{j\phi_c}. \tag{4.11}$$

Let the input and output signals of arm k be called respectively i_k and o_k. Note that the terms "input" and "output" are relative to the arm, so that the input is the signal coming from the MMI, to the arm. One can write two sets of equation showing their relations:

$$\begin{cases} i_1 &= c_{MMI}(\lambda)o_4 + t_{MMI}(\lambda)o_3 \\ i_2 &= c_{MMI}(\lambda)o_3 + t_{MMI}(\lambda)o_4 \\ i_3 &= c_{MMI}(\lambda)o_2 + t_{MMI}(\lambda)o_1 \\ i_4 &= c_{MMI}(\lambda)o_1 + t_{MMI}(\lambda)o_2 \end{cases} \tag{4.12}$$

$$\begin{cases} o_1 &= f_1(\lambda) i_1 \\ o_2 &= f_2(\lambda) i_2 \\ o_4 &= f_4(\lambda) i_4 \end{cases} \tag{4.13}$$

The goal is to determine the full system's transfer function, defined as $f(\lambda) = \frac{i_3}{o_3}$ with the notation chosen for inputs and outputs. Rewriting the expression for i_3:

$$\begin{aligned} i_3 = c_{MMI}(\lambda) f_2(\lambda) \left[c_{MMI}(\lambda) o_3 + t_{MMI}(\lambda) o_4 \right] \\ + t_{MMI}(\lambda) f_1(\lambda) \left[c_{MMI}(\lambda) o_4 + t_{MMI}(\lambda) o_3 \right]. \end{aligned} \tag{4.14}$$

It can be reorganised into the following, replacing o_4 by its expression from 4.13

$$\begin{aligned} i_3 = & \left[c_{MMI}(\lambda) f_2(\lambda) c_{MMI}(\lambda) + t_{MMI}(\lambda) f_1(\lambda) t_{MMI}(\lambda) \right] o_3 \\ & + \left[c_{MMI}(\lambda) f_2(\lambda) t_{MMI}(\lambda) + t_{MMI}(\lambda) f_1(\lambda) c_{MMI}(\lambda) \right] f_4(\lambda) i_4. \end{aligned} \tag{4.15}$$

Following a similar procedure, i_4 can be expressed as a function of o_3:

$$\begin{aligned} i_4 = & \left[c_{MMI}(\lambda) f_1(\lambda) t_{MMI}(\lambda) + t_{MMI}(\lambda) f_2(\lambda) c_{MMI}(\lambda) \right] o_3 \\ & + \left[c_{MMI}(\lambda) f_1(\lambda) c_{MMI}(\lambda) + t_{MMI}(\lambda) f_2(\lambda) t_{MMI}(\lambda) \right] f_4(\lambda) i_4 \\ i_4 = & \, o_3 \frac{\left[c_{MMI}(\lambda) f_1(\lambda) t_{MMI}(\lambda) + t_{MMI}(\lambda) f_2(\lambda) c_{MMI}(\lambda) \right]}{1 - \left[c_{MMI}(\lambda) f_1(\lambda) c_{MMI}(\lambda) + t_{MMI}(\lambda) f_2(\lambda) t_{MMI}(\lambda) \right] f_4(\lambda)}. \end{aligned} \tag{4.16}$$

Using 4.16 in 4.15, one can conclude for the system's transfer function $f(\lambda)$:

$$\begin{aligned} f(\lambda) = & \, c_{MMI}(\lambda) f_2(\lambda) c_{MMI}(\lambda) + t_{MMI}(\lambda) f_1(\lambda) t_{MMI}(\lambda) \\ & + \left[c_{MMI}(\lambda) f_1(\lambda) t_{MMI}(\lambda) + t_{MMI}(\lambda) f_2(\lambda) c_{MMI}(\lambda) \right] \\ & \times \frac{\left[c_{MMI}(\lambda) f_2(\lambda) t_{MMI}(\lambda) + t_{MMI}(\lambda) f_1(\lambda) c_{MMI}(\lambda) \right]}{1 - \left[c_{MMI}(\lambda) f_1(\lambda) c_{MMI}(\lambda) + t_{MMI}(\lambda) f_2(\lambda) t_{MMI}(\lambda) \right] f_4(\lambda)}. \end{aligned} \tag{4.17}$$

This equation is the transfer function of the 2-by-2 MMI coupled cavity structure.

For the 3-reflector structure, the expected reflection spectrum was simulated by implementing Equation 4.17 with Matlab, with the dimensions of the design. The result can be seen in Figure 4.10. The mode spacing is due to the main cavity length (approximately 1.5mm), while the super-mode spacing is caused by the length difference between the two coupled cavities. The super-mode

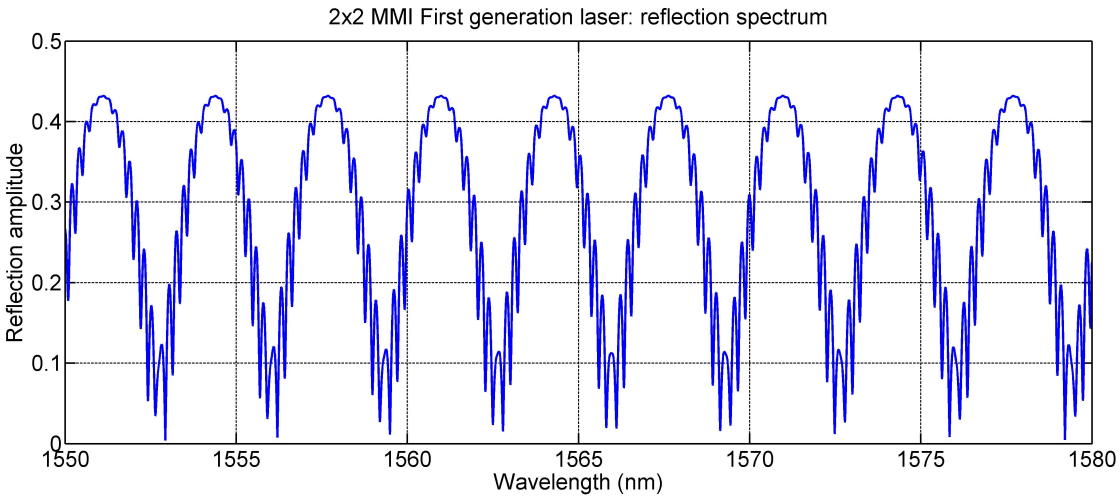

Figure 4.10: SMM-simulated reflection spectrum for the first generation device with 3 reflectors and a cleaved facet showing an expected mode spacing of 1.5nm and a super-mode spacing of 3.5nm

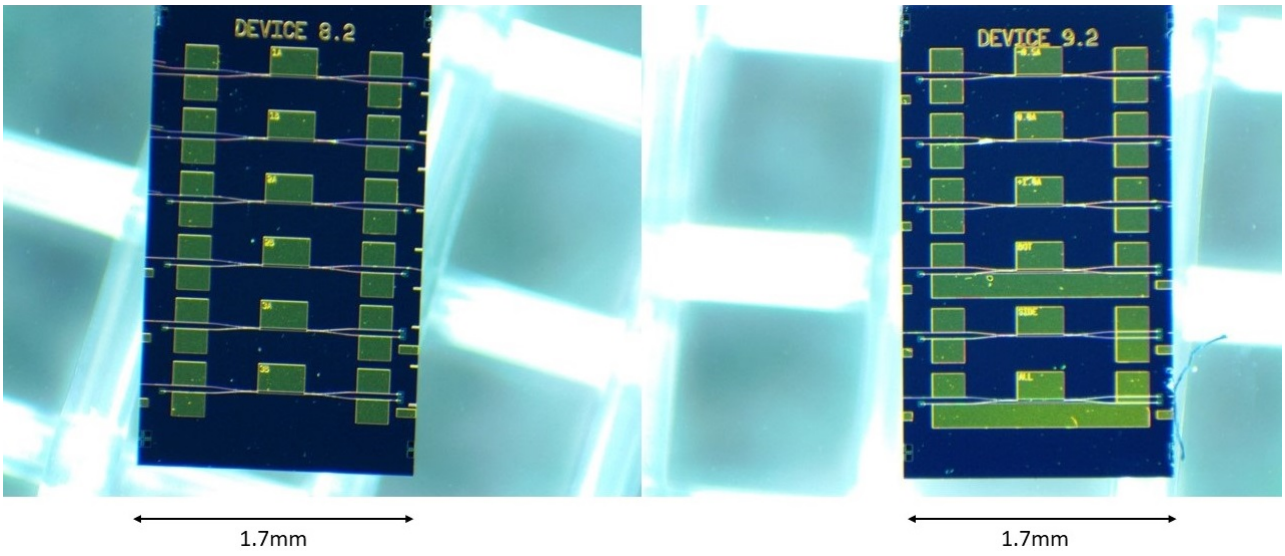

Figure 4.11: Microscope image of fabricated and cleaved devices from the first generation

spacing expected through simulation is approximately 3.5nm.

4.4 Device characterisation

After fabrication, the samples were cleaved (see Figure 4.11) and the testing procedure was performed. The main purpose of the 1-reflector structure was to

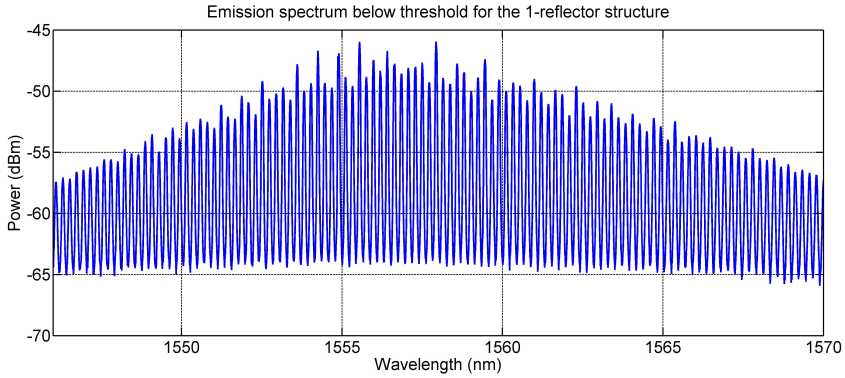

Figure 4.12: Emission spectrum below threshold of the 1-reflector structure with shallow isolation slots

ensure that the MMI coupler was successfully working. To do so, the bottom-right arm (with the MMI reflector), was powered and the power output was measured from each arm on the right using a handheld power meter. In the absence of current, the background signal was measured to be -70dBm. When 50mA was injected in the aforementioned arm, power levels of -56dBm were recorded for each output arm, confirming the MMI coupler was equally splitting the light signal between the two outputs. For this series of devices, up to 180mA were injected into the MMI sections, and up to 70mA were injected into the waveguide sections.

The emission spectrum for below threshold for the structure with shallow slots (See Figures 4.12 and 4.13) showed a behavior similar to a Fabry-Perot laser of length equal to that of the structure, however residual reflections on the slots were recorded, shown as the lower peaks in the Fourier analysis. In the case of deep slots, the Fourier analysis shows a much stronger effect of the slots (Figure 4.14).

The 2-reflector devices (Figure 4.2) were developed in order to confirm that a cavity equipped with MMI reflectors on each end could successfully lase. A variety of emission spectra were recorded in different current configurations. Figure 4.15 presents a lasing spectrum, and the Fourier analysis (Figure 4.16) that clearly shows two cavities of different lengths. Those lengths are compatible with the geometry of the device, one being the cavity formed by the bottom arms, and the other one being the cavity formed by a the top-left arm equipped with a cleaved facet, and the bottom-right arm with a MMI reflector. Figure 4.17 illustrates different lasing spectra that confirm both Vernier-like tuning and fine tuning around the lasing wavelength by small adjustment of the cur-

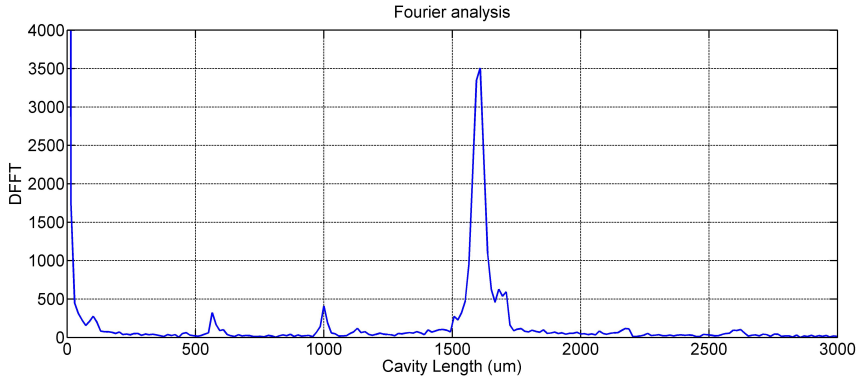

Figure 4.13: Fourier analysis of the emission spectrum of the 1-reflector structure with shallow isolation slots - the low peaks at 500μm show the limited impact of shallow isolation slots on the reflection profile

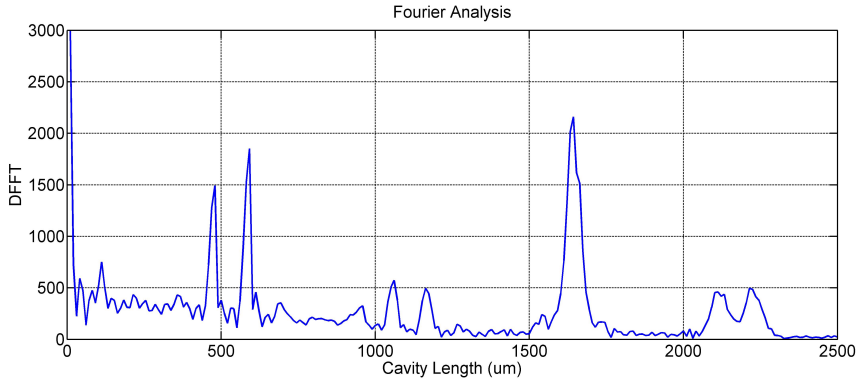

Figure 4.14: Fourier analysis of the emission spectrum of the 1-reflector structure with deep isolation slots - the larger peaks at 500μm show the increased effect of deeply etched slots on the reflection profile

rent injected into the MMI, are achievable. Power outputs of up to -10dBm, and SMSR values up to 30dB were recorded for those devices. It can also be noted that the main lasing cavity is the one involving the cleaved facet. This suggests the MIRs have a lower reflectivity than cleaved facets. The structure using deep slots showed similar behavior, but the deep etch significantly increased the effect of the slots on the spectrum (Figure 4.18).

The 3-reflector structures showed similar behavior, with fine tuning achievable over a range of 0.8nm (Figure 4.19). Once again, the main cavity was the one involving the output arm, which was equipped with a cleaved reflective facet. In the case of the deep slots, a 26dB SMSR was achieved (Figure 4.20) for a total collected power output of -15dBm.

The variations of contact configurations were also tested, where some sections

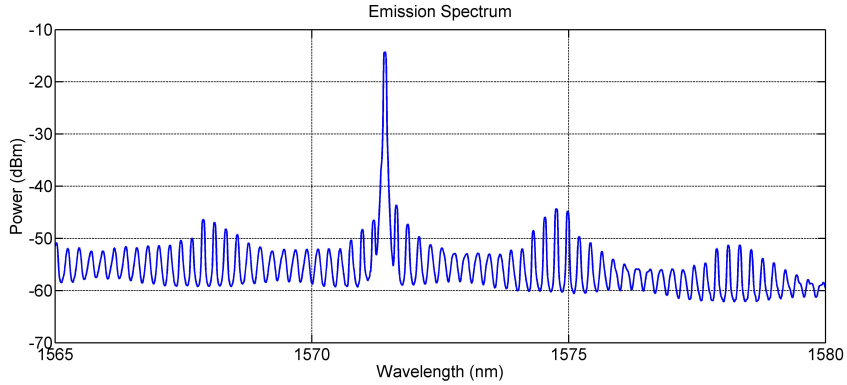

Figure 4.15: Emission spectrum of the 2-reflectors structure with shallow isolation slots showing single-mode operation and the envelope typical of a dual-cavity system

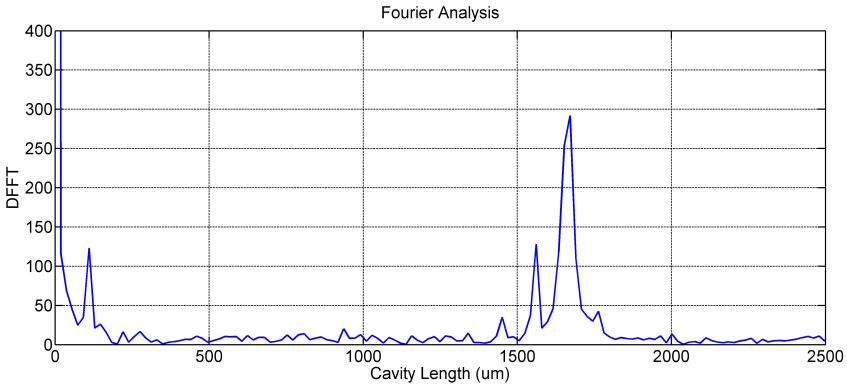

Figure 4.16: Fourier analysis of the emission spectrum of the structure with two reflectors and shallow isolation slots - the peaks at 1.6mm and 1.7mm match the lengths of the different cavities defined by the cleaved facet and MIRs and the 0.1mm peak corresponds to the length difference between the two cavities, with no visible effect of the slots on the spectrum

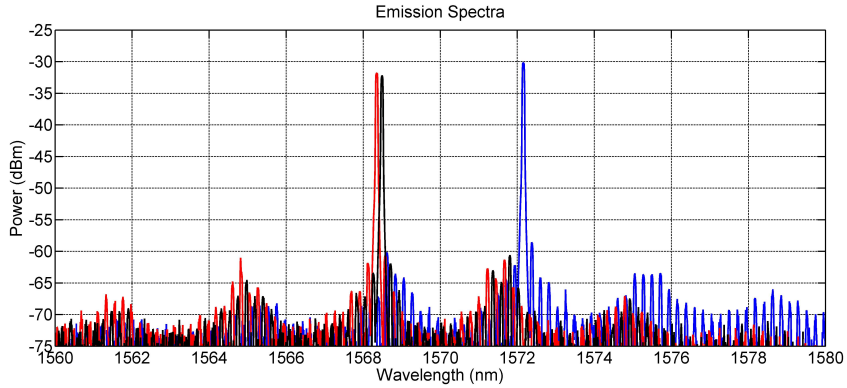

Figure 4.17: Superimposed emission spectra showing both Vernier-like and fine tuning achieved for the 2-reflectors structure with shallow isolation slots

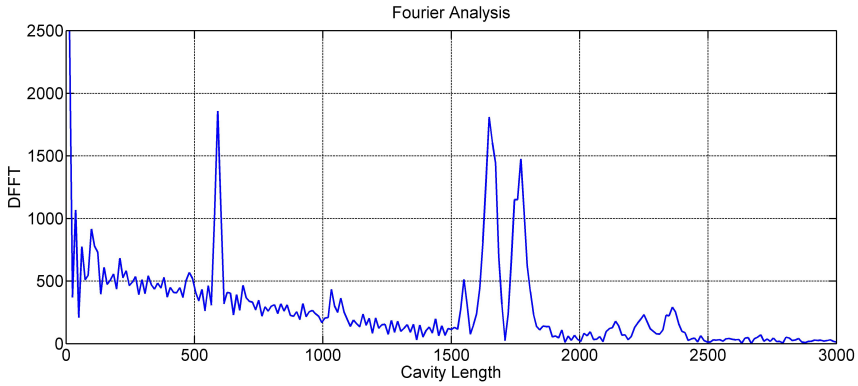

Figure 4.18: Fourier analysis of the emission spectrum of the structure with two reflectors and deep isolation slots - although the 0.1, 1.6 and 1.7mm peaks match the cavity dimensions, the 0.6mm peak suggests the deep slots cause strong interference

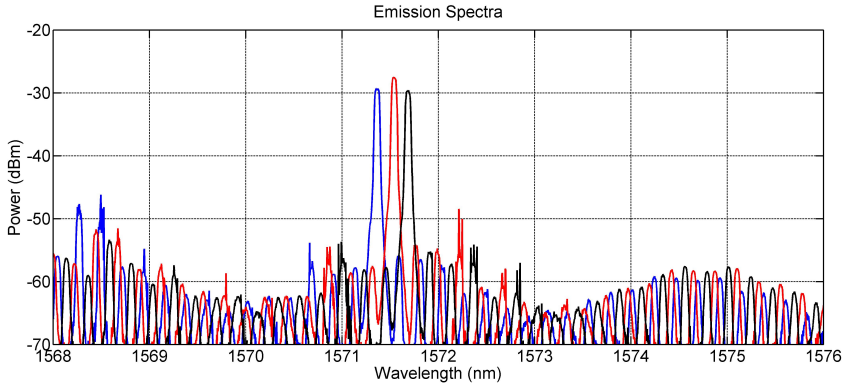

Figure 4.19: Superimposed emission spectra showing the fine tuning of the 3-reflectors structure with shallow isolation slots

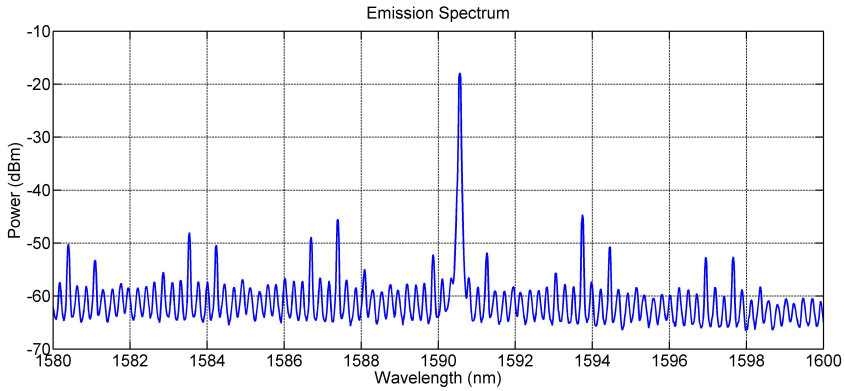

Figure 4.20: Emission spectrum for the 3-reflectors structure with deep isolation slots

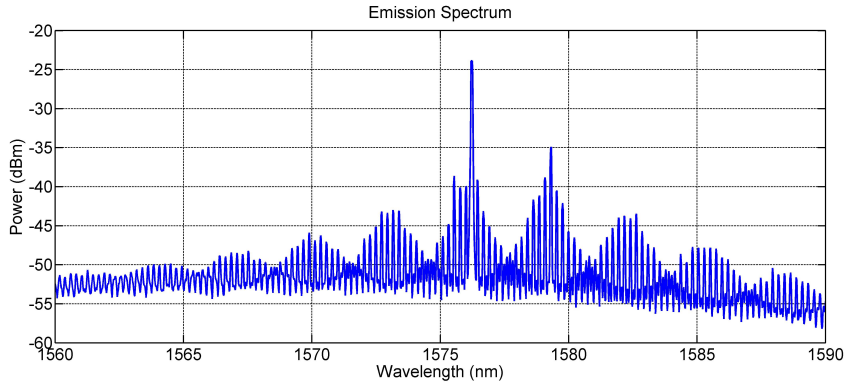

Figure 4.21: Emission spectrum for the three reflective sections electrically connected - the lack of flexibility for the different sections makes it difficult to achieve single-mode lasing

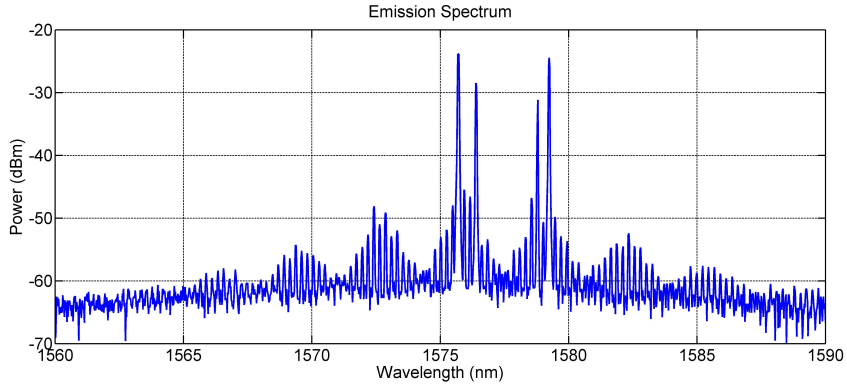

Figure 4.22: Emission spectrum for the two right hand side sections electrically connected - the lack of flexibility for the different sections makes it difficult to achieve single-mode lasing

were powered from the same contact pad. The case where three sections were controlled together showed poor single-mode performance (Figure 4.21), and no real control of the spectrum could be achieved. The case where two side arms were connected was not satisfactory either (Figure 4.22).

With this set of samples, preliminary validation of the theoretical model for the spectral behaviour of the devices was achieved. The MMI coupler's geometry was also confirmed correct, with equal splitting of the input signal between the two output ports. It was also shown that the deeply etched slots, despite being angled by 7° relatively to the waveguide, caused significant reflection which, if undesired, suggests the design rule that isolation slots should be kept shallow unless reflection is also desired. The necessity for separate control pads was confirmed by the poor control achieved on devices including electrically

connected sections. Finally, single mode was achieved as well as tuning, confirming the coupling of the two cavities and that further investigating this type of devices is relevant. With the validation of the MMI couplers, the effort was oriented towards another of the objectives of this incremental work: the development of cleave-free devices for facilitated integration. The development in parallel of a simulation tool to predict spectral features of the devices also required further validation and the use of cleave-free reflectors was crucial to this, with cavities of known lengths, while a cleaved facet introduces an uncertainty due to the unpredictable position of the cleave.

Chapter 5

Second generation of lasers

5.1 Design and purpose

The second generation of devices was undertaken with the aim of developing a proof of concept for an MMI-based laser using exclusively MIRs as reflectors, instead of cleaved facets. After observing in the previous generation that the deep isolation slots caused an undesired parasitic reflection, they were kept shallow for this new set of devices.

Another objective was to reduce the round-trip losses caused by the design itself. Indeed, the laser design uses an output coupler extracting 50% of the power via the 2-by-2 MMI coupler. This output power is a loss for the round-trip, thus increasing the necessary gain to achieve threshold. A solution considered to reduce this loss was to include a deep reflective slot, at a carefully chosen position, on the output arm. The reflected power would offer a feedback boost reducing the necessary gain, and thus reducing the current needed to achieve lasing and corresponding heating.

The other goals of this generation of devices were to refine and validate the simulation model, and to assess the tunability of the proposed designs. For this purpose, variants were included where the length difference between the two coupled cavities is adjusted by modifying the length of one of the arms of the structure. Length differences from 25μm to 150μm were included.

This led to the development of two sets of devices for this generation, one including a slot on the output arm and one without. The overall length of the lasers was also reduced in order to reduce the overall footprint, improving

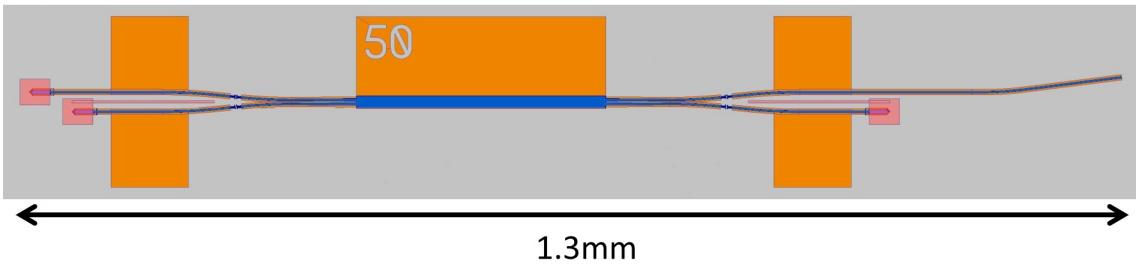

Figure 5.1: Schematic of a second generation 2x2 MMI laser - the output is angled relative to the cleave place to avoid reflections, so that the cavities are defined only by the MIRs

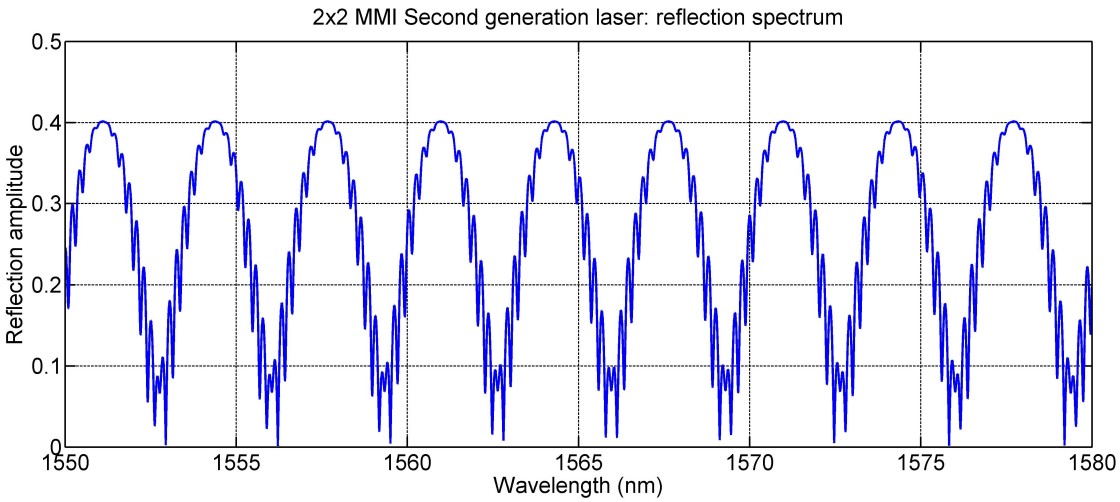

Figure 5.2: SMM-simulated second generation 2x2 MMI laser reflection profile

the device density and thus the yield and cost effectiveness of the fabrication process.

The proposed devices were simulated similarly to the previous generation of lasers. The version without a reflective slot, shown in Figure 5.1, led to a reflection spectrum displayed in Figure 5.2, showing a typical dual-cavity system where the Fabry-Perot behavior is modulated by an envelope caused by the presence of two cavities.

In addition to this set of devices, directly inspired from the first generation, a set of devices was included where a reflective slot is included on the output arm. In a general case, this raises to four the number of cavities one can identify in the structure. Considering L the main cavity length defined by the bottom arms, ΔL the arm length variation on the device previously described, this slot is positioned so that a new arm length $L_{basearm} + k \times \Delta L$ is created. One can

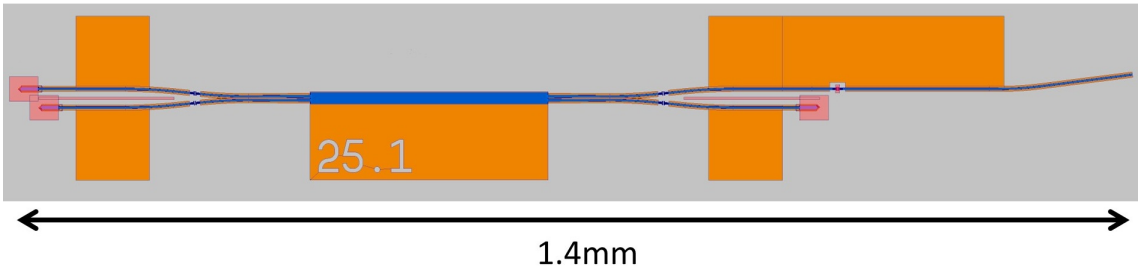

Figure 5.3: Schematic of a second generation 2x2 MMI slotted laser with $\Delta L = 25\mu$m and $k = 1$ - the slot is placed on the output arm to increase feedback and to modify the reflection profile

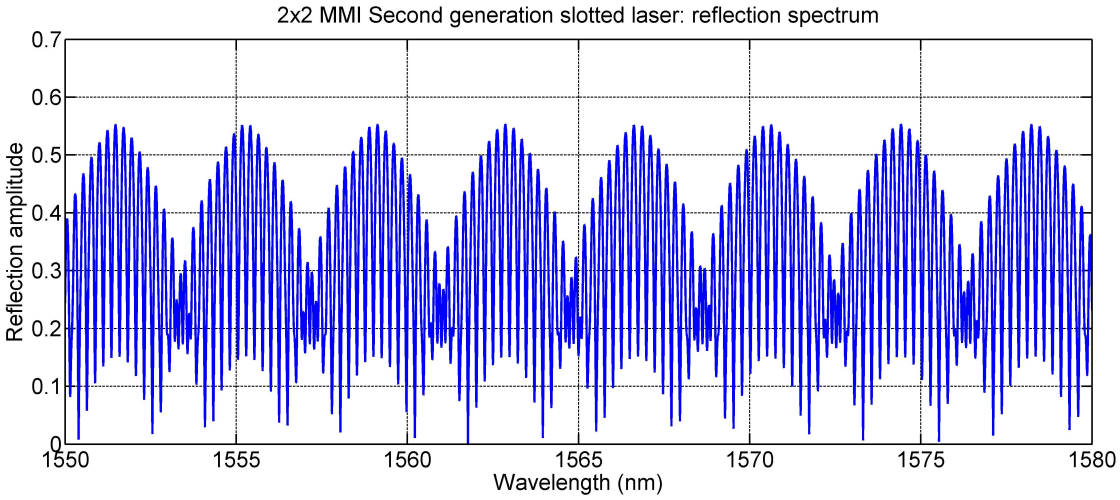

Figure 5.4: SMM-simulated second generation 2x2 MMI slotted laser reflection spectrum illustrating how the addition of the slot modifies the envelope shape

thus identify four cavity lengths: $L_1 = L$, $L_2 = L + \Delta L$, $L_3 = L + k \times \Delta L$ and $L_4 = L + (k+1) \times \Delta L$. In the specific case where $k = 1$, only three cavities remain, and only two cavities when $k = 0$. The schematic structure where $\Delta L = 25\mu$m and $k = 1$ is shown in Figure 5.3, and the spectrum for the case $\Delta L = 100\mu$m and $k = 1$ is shown in Figure 5.4. One can note that the super-mode shape is modified by the additional slot.

5.2 Device characterisation

Upon completion of the fabrication run including devices of the second generation, the initial testing was not successful to achieve any lasing with a spontaneous emission only leading to power ouputs below -50dBm. The emis-

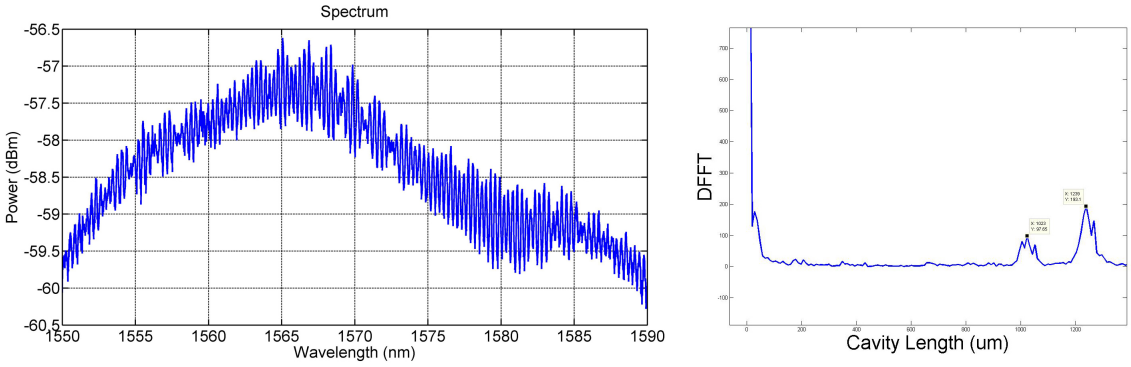

Figure 5.5: Emission spectrum and corresponding Fourier analysis of an unsuccessful Second Generation MMI laser where no lasing was achieved but dual-cavity behavior can be noticed with the super-mode envelope and the two peaks in the Fourier analysis

sion spectrum below threshold was recorded and analysed, using a Fourier transform-based technique to determine the cavity lengths leading to the observed spectrum. It showed that two resonant cavities were involved, of lengths corresponding to the two cavities of the design (Figure 5.5). For this series of devices, up to 180mA were injected into the MMI sections, and up to 50mA were injected into the waveguide sections.

However, the other customers of this fabrication run also noticed unusual behavior and difficulties achieving lasing with their own devices. SEM imaging of some samples was performed, showing that the oxide passivation layer was extremely porous (Figure 5.6). The layer is used to protect the semiconductor material and to prevent any electrical contact between the metal and the areas that don't need to be powered. In case of porosity, the current can leak and not reach the waveguides that need to be powered. The leakage, combined with the inherently lossy design, resulted in the absence of lasing, even when high currents were applied to the different parts of the device.

In the meantime, other members of the group successfully demonstrated the use of etched facets instead of MIRs as on-chip reflective features, which led to the design of the third generation of devices. As a result, the following fabrication run involved second and third generation devices, as well as test structures to compare the performance of MIRs and etched facets. In order to reduce the leakage risk for this new fabrication run, is was decided to increase the passivation layer thickness from 400nm to 500nm, and to also increase the metal layer thickness, from approximately 300nm to approximately 400nm. By doing so, the risks of a porous passivation layer and of metal breaking on side

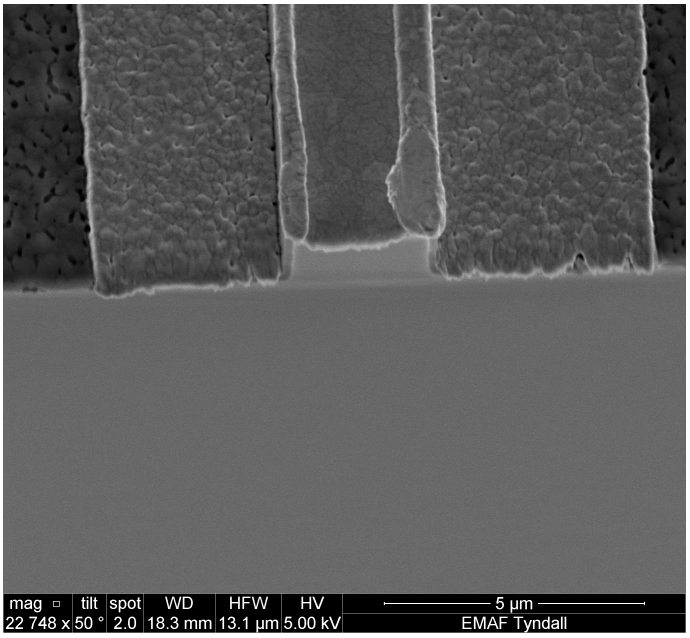

Figure 5.6: SEM image of a ridge showing a porous passivation layer, compromising the electrical isolation

walls were reduced, increasing the chance of success for the devices.

The new set of devices typically showed SMSR values between 15dB and 25dB and power outputs in the range of -15dBm, as well as moderate tuning capabilities (Figure 5.7). As shown in Figure 5.8, good agreement was also observed between the spectra below threshold, and the theoretical model predicting the mode and super-mode spacing in the device emission spectrum. However, after observing significantly better performance (SMSR, tunability...) for third generation devices, the study of the second generation was stopped early to focus on the more promising, third generation devices.

The second generation, although limited in terms of performance due to the poor reflectivity of the MIRs, brought valuable information with the validation of the theoretical model and of the MMI-based laser concept.

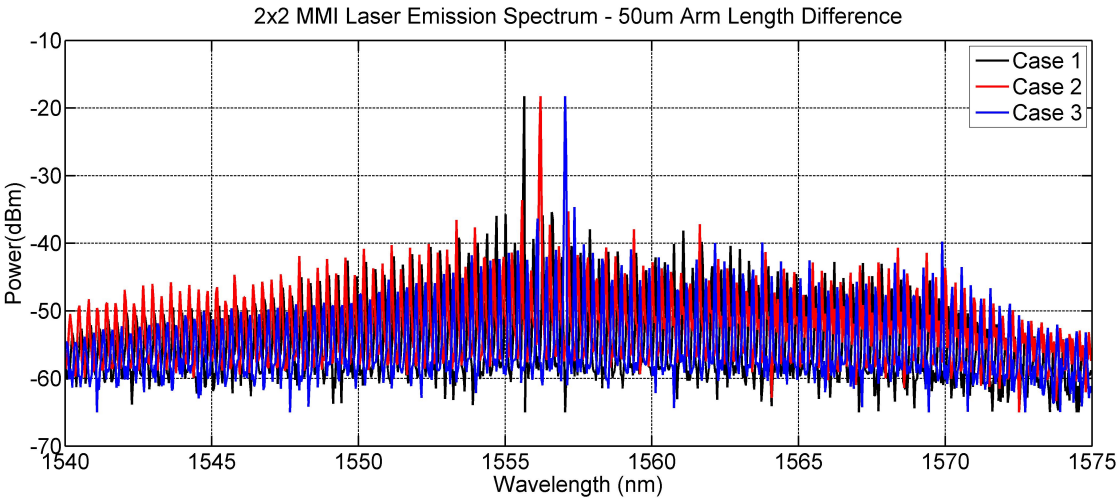

Figure 5.7: Superimposed emission spectra of a 2x2 MMI/MIR laser for different configurations of injected currents showing limited tuning capability for this laser

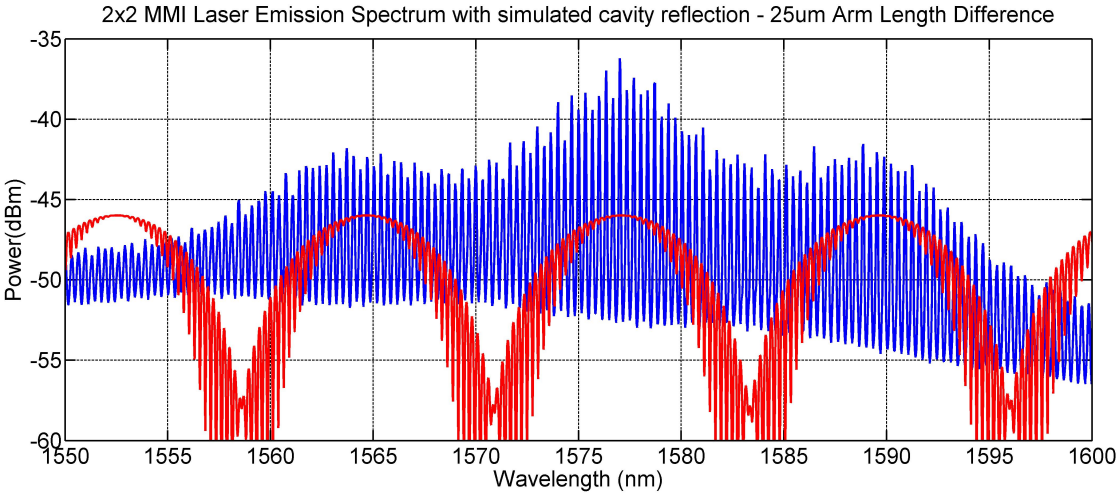

Figure 5.8: Superimposed emission spectrum and SMM-simulated reflection profile showing good agreement for the super-mode spacing - the simulated profile was vertically offset for clarity

Chapter 6

Third generation of lasers

6.1 Design and purpose

The third generation of devices was developed with the aim of reducing the round-trip losses caused by the etched reflectors and the output coupler from the MMI structure.

Indeed, while the perfect MIRs are using total internal reflection to achieve high reflectivity, the fabricated structures have imperfect side walls, causing scattering losses and compromising the total internal reflection. It appeared necessary to explore alternative reflector designs, such as the etched facet (EF): the waveguide is terminated by a stub, in a deeply etched area. The stub is designed to ensure that any defects caused by the lithography resolution occur at a distance from the centre of the waveguide. This facilitates the etch of a flat wall perpendicular to the waveguide to maximise reflection. The deep etch causes the quantum wells to be exposed to the reflective interface, maximising the portion of the mode meeting the interface and thus further improving the reflection. In order to futher improve the reflectivity of the facet, the step used to deposit the contact metal layer is also used to deposit a layer of metal on the wall created. This reflective feature is called metal-coated etched facet (MEF).

The device design also causes round-trip losses due to the nature of the 2-by-2 MMI coupler. Indeed, 50% of the power is coupled into the output waveguide, and is lost in terms of feedback, and approximately 30% (facet) of the 50% (MMI split) so 15% of the power is reflected back into the cavity for this part of the round-trip. As a result, the lasing threshold requires more pumping to com-

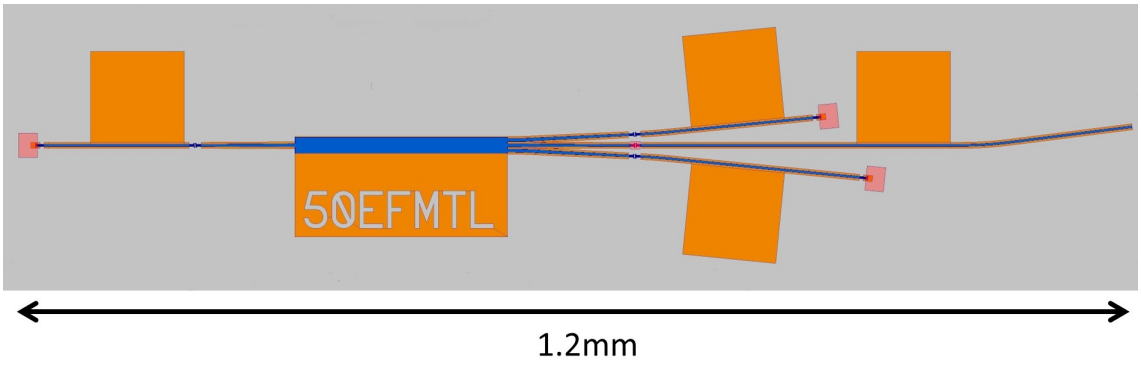

Figure 6.1: Third generation 1x3 MMI laser schematic - the 1x3 design reduces the power that is lost for feedback and in this design, a deep slot is used to increase feedback and MEFs are used as an alternative to MIRs to assess their performance as a reflector

pensate for the loss, compared to designs such as the Fabry-Perot laser where approximately 30% of the power would be kept for feedback at the facet. While reflective slots can be added to the output arm, they cause additional loss and are sensitive to depth [38]. Another approach was proposed to mitigate this problem: using a 3-by-3 MMI coupler reduces the power being coupled out to 33% instead of 50%. A laser design was developed using a 3-by-3 coupler MMI: at one end of the coupler, the central port is connected to a waveguide terminated by a reflective feature, either a MIR or a MEF. At the other end, the central port is connected to an output coupler including a 1μm wide deeply etched slot, while the two outer ports are connected to arms of different lengths and terminated by MIRs or MEFs. The different arm lengths make it possible to obtain single mode lasing and tunability. This design is shown in Figure 6.1 and was dubbed "Psi" laser due to its resemblance to the Greek letter.

This generation of devices aimed at testing the MEF as an alternative to MIRs for on-chip reflection, and at determining if the 1-by-3 MMI laser concept was a valid option or not. After the poor performance of the previous generation, it appeared necessary to include again the 2-by-2 structures from the second generation, to determine their performance after good fabrication conditions.

6.2 Device simulation

The proposed laser relied on a different type of MMI coupler, so a careful simulation of the new design was necessary prior to approval for fabrication. One

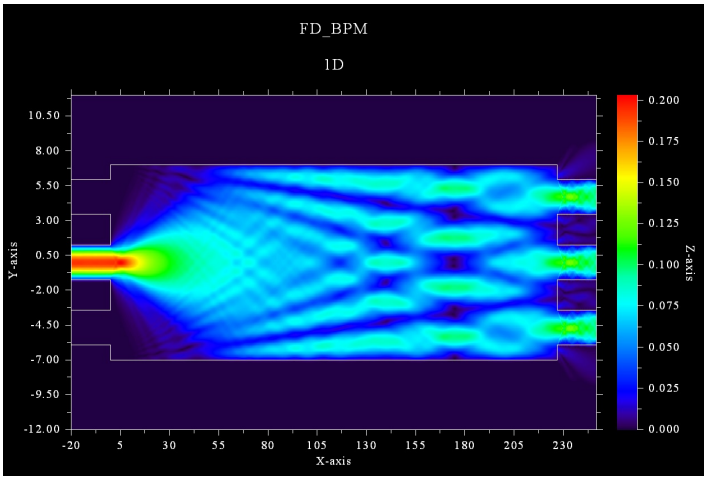

Figure 6.2: BPM simulation of the Splitter operation of the 3x3 MMI coupler

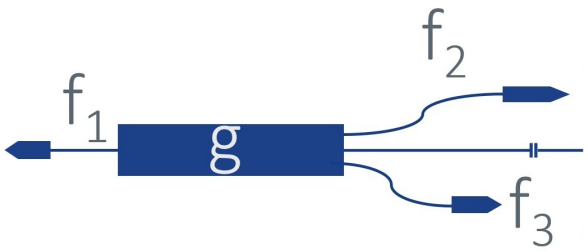

Figure 6.3: 1x3MMI laser schematic with the names of the transfer functions used in the calculations

of the key points to determine was the dimensions of the 3-by-3 MMI coupler used in the design. To do so, the beam propagation module (BPM) of the PICDraw design software was used to simulate the MMI coupler, for different dimensions. This simulation aimed at finding the dimensions leading to minimal signal losses in the splitting and recombination situations, as well as the even splitting of the input power, into the output ports. A satisfactory geometry, with the simulation shown in Figure 6.2, was found, with a length of 227.3μm and a width of 17μm.

In addition to finding the correct dimensions for the MMI coupler, the device behaviour was simulated by using the same method used previously: the transfer functions of the different sections were determined by the means of the scattering matrix method, and combined using the theoretical properties of a perfect 3-by-3 MMI coupler, described in [48]. The resulting reflection profile was determined using the transfer function 6.1, using the names presented in Figure 6.3.

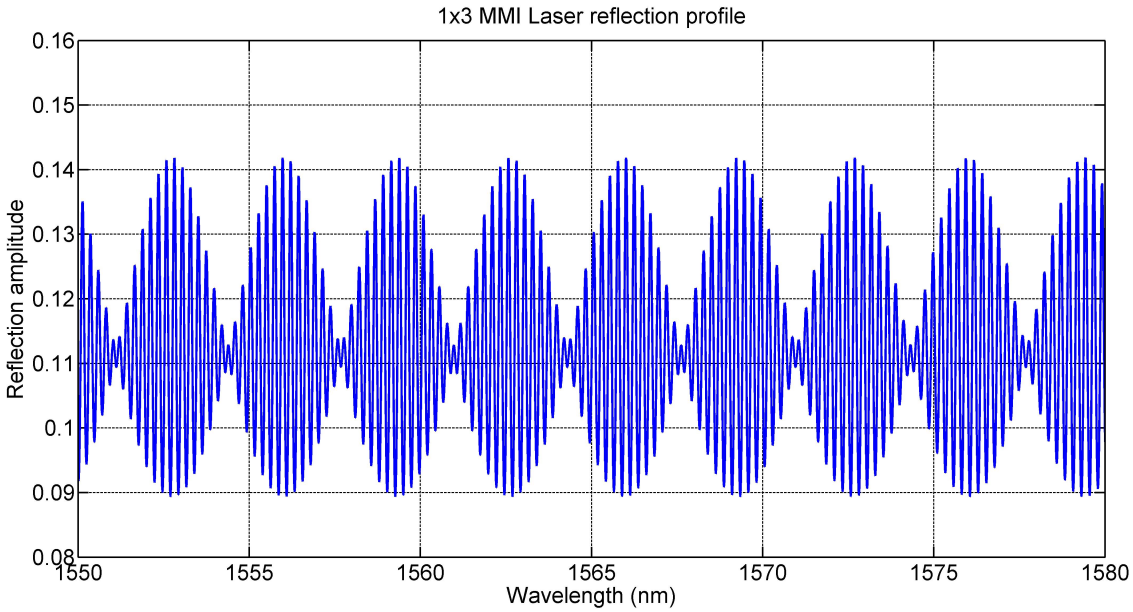

Figure 6.4: 1x3 MMI laser SMM-simulated reflection spectrum showing a 3nm super-mode spacing

$$f_{3\times3} = g_{14} f_1 \times \left(g_{41} + \frac{g_{12} f_1 g_{41} \left(f_2 + f_3\right) g_{21}}{1 - g_{12} f_1 g_{21} \left(f_2 + f_3\right)} \right) \tag{6.1}$$

The resulting reflection profile is shown in Figure 6.4. The super-mode spacing is related to the length difference between the two main cavities and can be adjusted during the mask design phase. With the simulation of the 1-by-3 MMI laser, several iterations were included in the lithography mask, using different reflectors: MIRs and MEFs, as well as different length differences.

6.3 Device characterisation

6.3.1 2-by-2 laser characterisation

After the samples were fabricated and cleaved, the testing was performed. The bars were placed on a brass, temperature-controlled chuck. Needle probes were used to inject current into the different sections of the devices. Lensed fibres were used to collect the light output. A view of the devices under test can be seen in Figure 6.5. It was possible, by adjusting the injected current in the different sections, to modify the output wavelength of the laser.

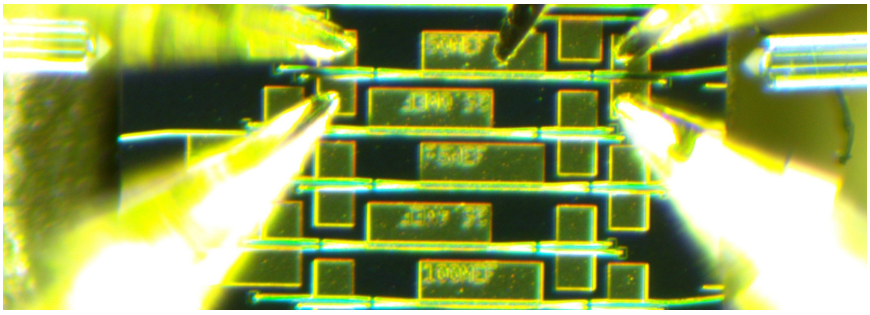

Figure 6.5: 2x2 MMI/MEF devices under test

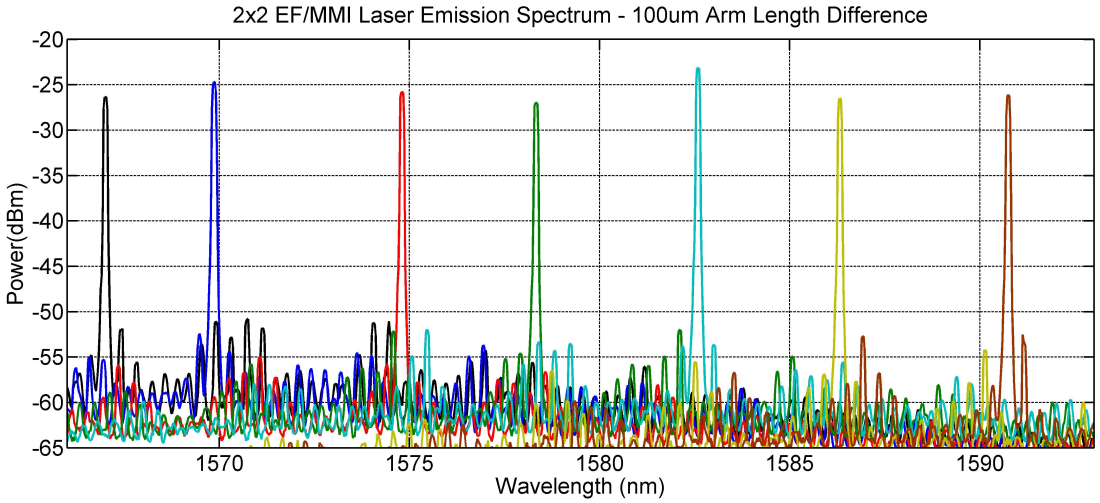

Figure 6.6: Superimposed emission spectra of a 2x2 MMI/MEF laser showing a 24nm discrete tuning range and SMSR levels above 25dB

Different current configurations were used to achieve discrete tuning, the lasing wavelength "jumping" from one super-mode to the next. Seven different super-modes were reached, covering wavelengths ranging from 1567nm to 1591nm, a span of 24nm with a total collected output power comprised between -25 and -20dBm. The superimposed emission spectra can be seen in Figure 6.6. The SMSR of the laser was maintained between 25dB and 30dB. The applied currents were between 75mA and 100mA for the MMI section, and between 15mA and 40mA for the waveguide sections.

In a similar fashion, a small adjustment of the current injected into the MMI section was used to finely tune the laser emission wavelength. A fine tuning range of 1.5nm was achieved in Figure 6.7, around the 1575nm wavelength. Larger variations of the current caused the SMSR to degrade, and eventually the main lasing wavelength to jump to the next super-mode.

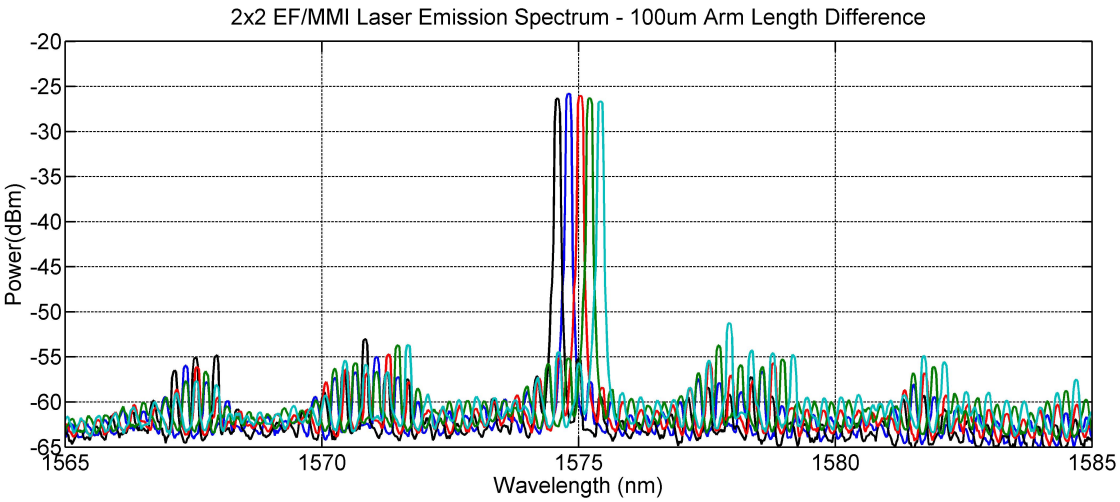

Figure 6.7: Superimposed emission spectra of a 2x2 MMI/MEF laser showing a 1.5nm continuous tuning range

This generation was also an opportunity to further validate the simulation model developed previously. A simulation was performed using the design dimensions for a 2-by-2 MMI laser. Because of the uncertainty on the exact refractive index, it was necessary to translate the simulated spectrum to match the maxima positions when compared with an actual laser emission spectrum. Indeed, considering the simulation of this laser, a variation of 0.05% of the index corresponds to a 1nm shift of the spectrum. Because the wavelength is significantly smaller than the cavity length, this index uncertainty has no significant impact on the super-mode spacing calculation, but does affect the position of the super-modes. Once this alignment was performed, it appeared clear that the predicted super-mode spacing matched that of the actual laser, validating the model as a means to predict the super-mode spacing of this type of devices. Superimposed simulated and collected spectra can be seen in Figure 6.8, showing good agreement in terms of super-mode spacing.

The laser linewidth was also measured, using a standard self-heterodyne technique described in [47]. The self-interference profile was collected (see Figure 6.9), showing a full-width at half-maximum (FWHM) of 1.2MHz. The laser linewidth is half of this value: 600kHz.

The slotted version of the 2-by-2 MMI laser was also tested. The emission spectra showed no significant variation compared to the version without slots. After observing that the laser behavior was similar, the testing was not pushed further.

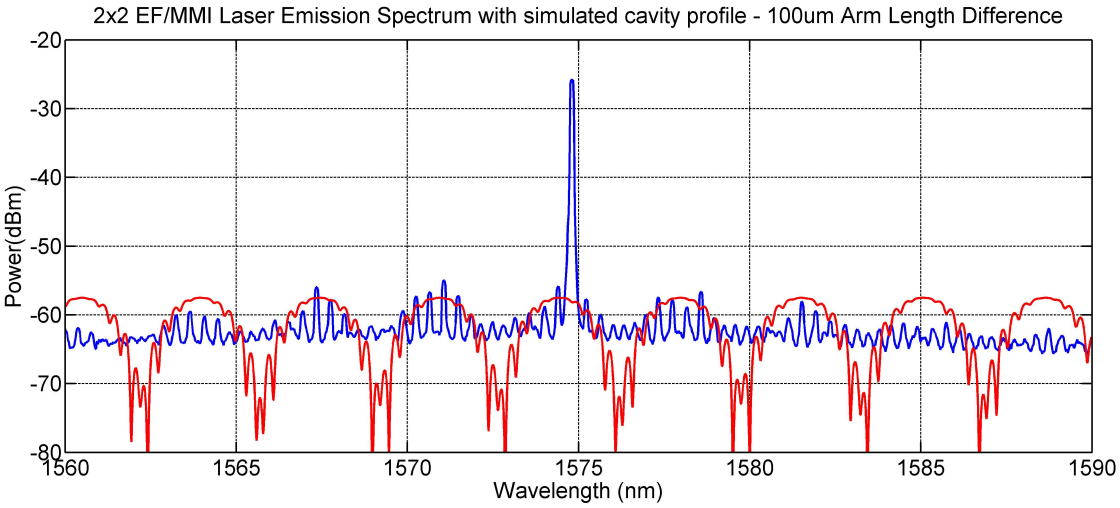

Figure 6.8: Emission spectrum of a 2x2 MMI/MEF laser (blue) and simulated reflection profile (red) showing good agreement between the simulation and measured data

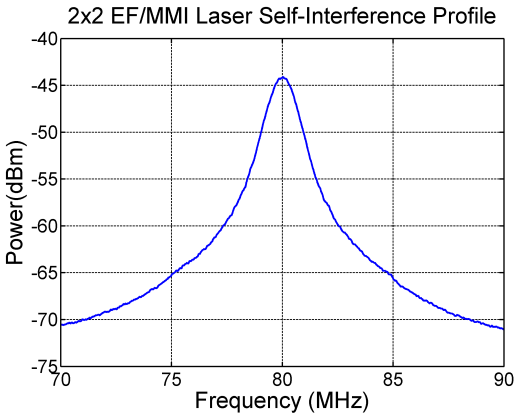

Figure 6.9: Self-interference profile of a 2x2 MMI/MEF laser showing a full width at half maximum of 1.2MHz, for a 600kHz linewidth, obtained using a self-heterodyne technique

6.3.2 1-by-3 laser characterisation

With the 2-by-2 device characterisation completed, the focus was shifted towards the new 1-by-3 design that can be seen on Figure 6.10. The characterisation procedure was similar to that of the 2-by-2 devices: first the verification of the lasing and of the single mode capability, followed by a focus on tunability, and additional specific testing for the linewidth. Attention was also brought to the spectral characteristics of the laser emission.

The initial testing performed on the 1-by-3 lasers confirmed that single-mode

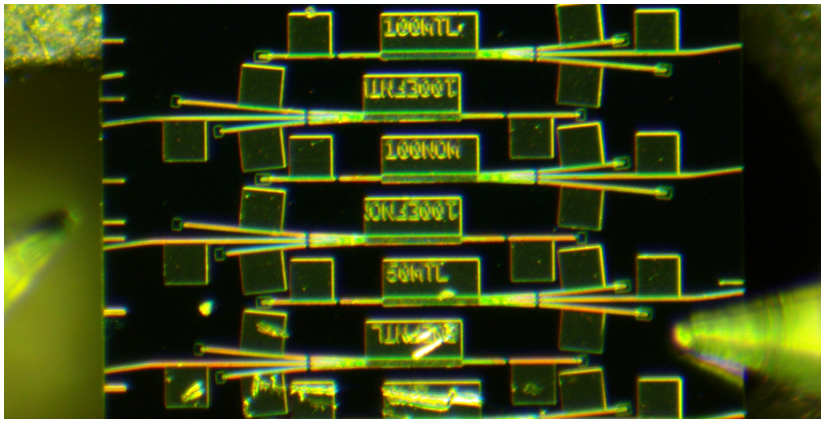

Figure 6.10: 1x3 MMI/MEF devices on the characterisation setup

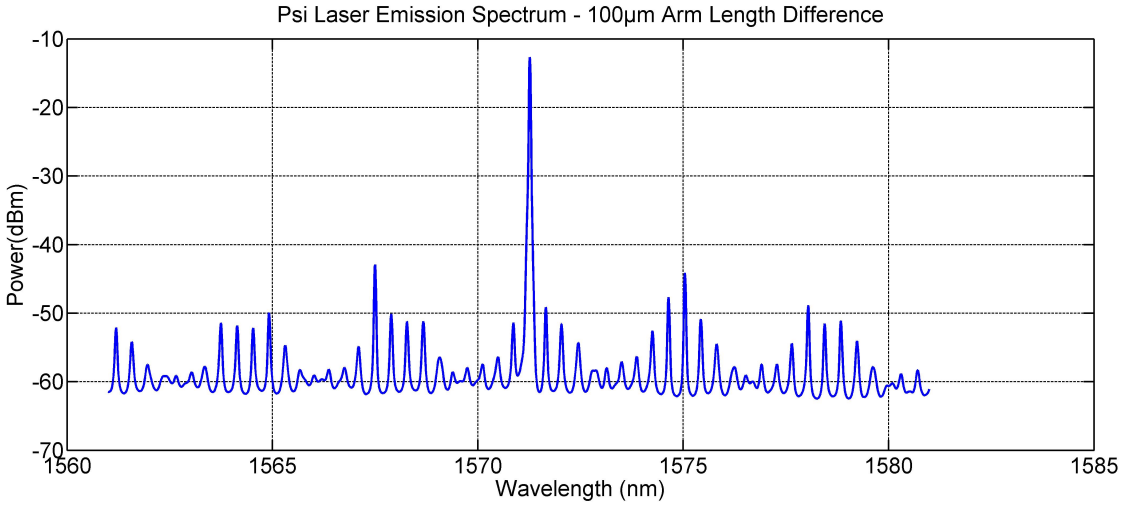

Figure 6.11: Emission spectrum of a 1x3 MMI/MEF laser showing single mode behavior with a 30dB SMSR and a super-mode spacing of approximately 3nm, matching the simulated reflection profile

lasing could be achieved, as shown on Figure 6.11. The super-mode shaping of the emission spectrum confirmed the multi-cavity nature of the laser, suggesting the 3-by-3 MMI coupler dimensions were adequate to achieve the desired function. The SMSR of approximately 30dB confirmed the single-mode nature of the laser.

With the initial testing showing the successful lasing of the device, a Fourier analysis of the emission spectrum was performed and is shown on Figure 6.12. This analysis allows a determination of the cavity lengths involved in the laser emission. This makes it possible to identify parasitic reflections that could be caused by imperfect MMI dimensions.

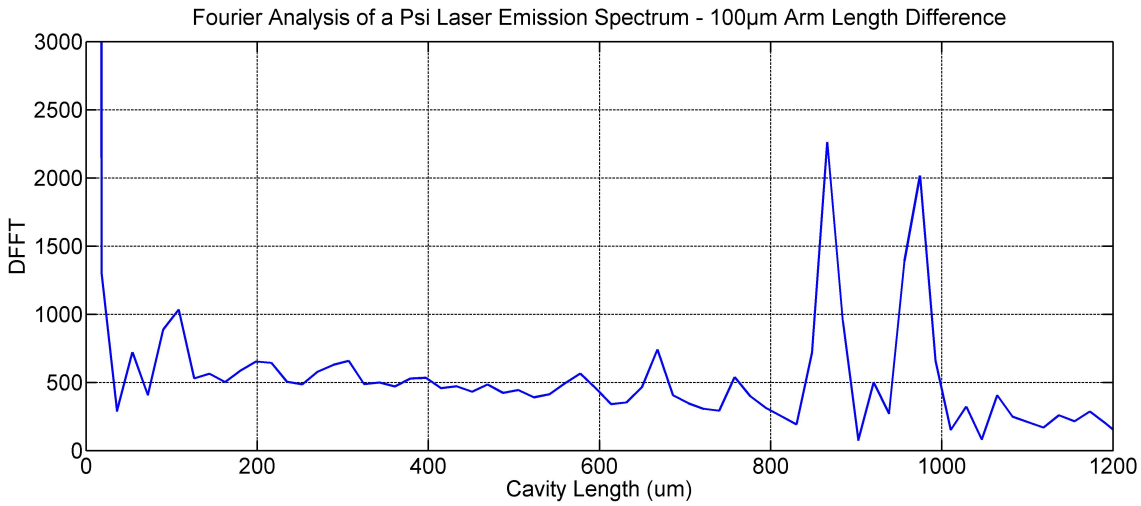

Figure 6.12: Fourier analysis of a 1x3 MMI/MEF laser emission spectrum, showing two main cavity lengths and additional parasitic reflections, suggesting imperfect MMI dimensions but satisfying operation of the MEFs

The two main peaks observed between 870 and 970μm correspond to the two cavity lengths included in the design. Their combination appears on the peak around 100μm. However, three minor peaks can be detected near 550, 650 and 750μm. These lengths corresponds to the path from a MEF to the opposite end of the MMI coupler for both arms (550 and 650μm) followed by their combination, 100 microns further. A possible conclusion could be that the design, although close to optimal, still leads to undesired reflections, suggesting a non-optimal geometry for the MMI.

One can also observe that no such reflection was observed that describes the path from the common MEF arm to the MMI coupler. If this reflection is exclusive to the combiner function of the MMI coupler, this leads to another possible explanation: this reflection could be the manifestation of imperfect recombination due to the phase mismatch of the different inputs. Indeed, a fraction corresponding to the mismatch between the actual phases and the ideal case, might not be successfully recombined into the common waveguide, and be reflected by the MMI wall and sent back to its source, leading to the observed reflection. A mismatch in terms of input powers could also cause a similar phenomenon, because the recombination is perfect only for equal input powers, with adequate phase differences. This hypothesis can be supported by the Psi design, where only a deep slot is used as a reflective feature on the central output arm, thus providing reduced feedback on the central input and leading to different input powers into the different MMI ports.

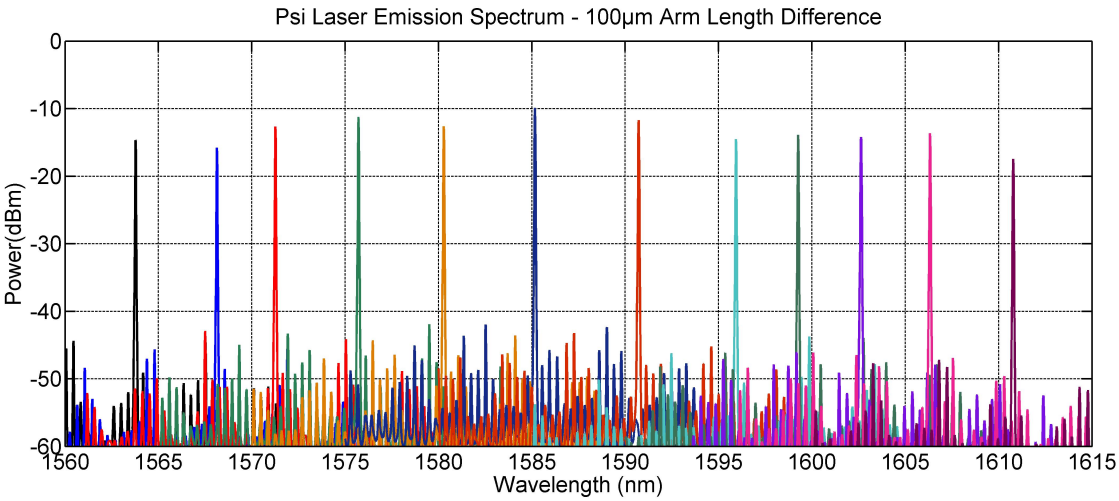

Figure 6.13: Superimposed emission spectra of a 1x3 MMI/MEF laser showing a 47nm discrete tuning range and SMSR levels above 30dB

Despite the imperfect nature of the laser, single mode lasing was achieved with total output powers of up to -7dBm, and the tunability was then assessed. The adjustment of the current in the different sections of the laser made it possible to tune the output wavelength over a range of up to 47nm, from 1564nm to 1611nm. The SMSR was maintained over 30dB over this range. The superimposed emission spectra showing the covered range are shown on Figure 6.13. For this design, the injected currents varied from 60mA to 100mA in the MMI section, and 10mA to 62mA for the waveguide sections. The tuning strategy observed here is similar to the other designs, where the gain is shifted by injecting more current into the MMI and common sections of the laser, followed by an adjustment of the injected current in the different cavity-specific waveguide sections to obtain single-mode. Small adjustment in the current injected into the MMI can then be performed for fine tuning of the lasing wavelength.

Fine tuning was also achieved, and a range of up to 3nm, from 1583nm to 1586nm was achieved for the 1-by-3 MMI/MEF laser designed with a cavity length difference of 50μm. In this range, the SMSR was maintained above 25dB.

Finally, the linewidth characterisation of the laser was performed using the same setup as for the 2-by-2 lasers. The laser linewidth, taken for the 1564nm lasing wavelength, was found to be approximately 800kHz, which is half of the FWHM on the self-interference profile shown on Figure 6.15. It is noteworthy that as for the 2-by-2 lasers, the actual linewidth might be lower than the one

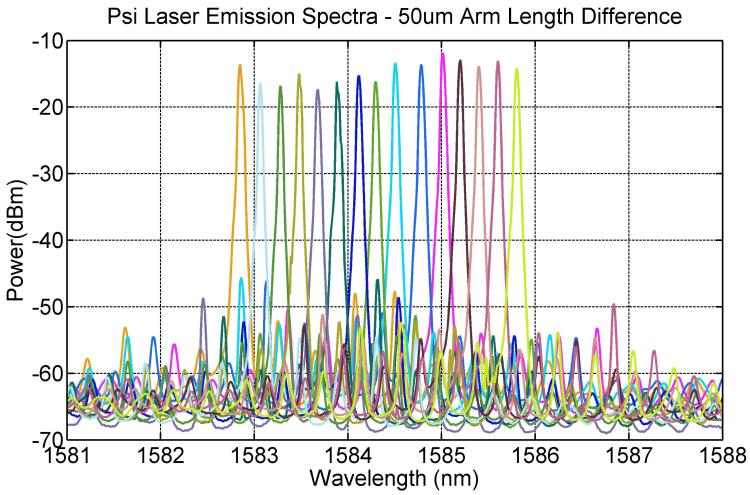

Figure 6.14: Superimposed emission spectra of a 1x3 MMI/MEF laser showing continuous tuning over a 3nm range

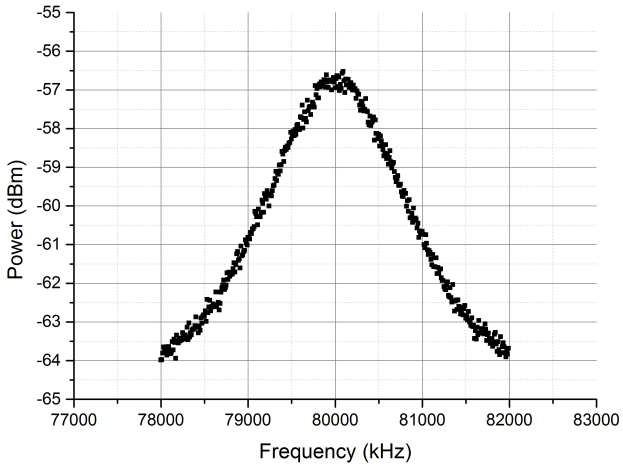

Figure 6.15: Self-interference profile of a 1x3 MMI/MEF laser showing a full width at half maximum of 1.6MHz, for a 800kHz linewidth

observed here, at is has been observed that the experimental setup is extremely sensitive to its environment. Every precaution was taken to reduce external interference (measurements taken after working hours to avoid vibrations from other activities, isolated optical table...) but it is practically impossible to reduce some sources of noise, such as that from the power supplies themselves or traffic around the building.

Considering the encouraging results of the MMI-based geometries, a set of new designs were then proposed. A particular interest was to study the usage of

loops for MMI-based devices, as well as alternatives to slots to create intra-cavity reflections. Improvements of the design tool used in this work to generate the lithography masks and thus device geometries, enabled the usage of customised curves and loops, and the opportunity to use this new functionality was taken with the following generation of lasers.

Chapter 7

Fourth generation of lasers

7.1 Design and purpose

With the success of the 1-by-3 MMI laser, a new generation of devices was developed in order to increase the range of designs based on MMI couplers. One point on which improvement seemed possible, is the round-trip loss. Indeed, the usage of etched facets, even though enabling cleave-like reflection, still means that a significant part of of the incident power is transmitted and lost. In an attempt to mitigate these losses, a variant was proposed, using loops and intra-cavity reflective features to achieve single mode. In the new designs, the waveguide loops from one port of the MMI to the other, so that in either direction, the power transmitted through the reflective feature can be redirected into the laser.

Two variants were proposed for the 2-by-2 and the 1-by-3 configurations. The reflective feature used for this series of devices was a pit, a deeply etched hole of diameter 1μm on the centre of the waveguide [42]. One or two pits were positioned at different locations in the loop, in order to generate an asymmetry leading to single mode behaviour. An example of a processed pit can be seen in Figure 7.1. Due to their shape, the two laser geometries were dubbed "Gamma" and "Phi".

The two geometries, shown on Figures 7.2 and 7.3, were designed with the main purpose of determining the viability of the loops in the lasers. In addition to this goal, this iteration was the opportunity to explore the effect of a crossing of two waveguides at a right angle, and to study the effect of a single pit as

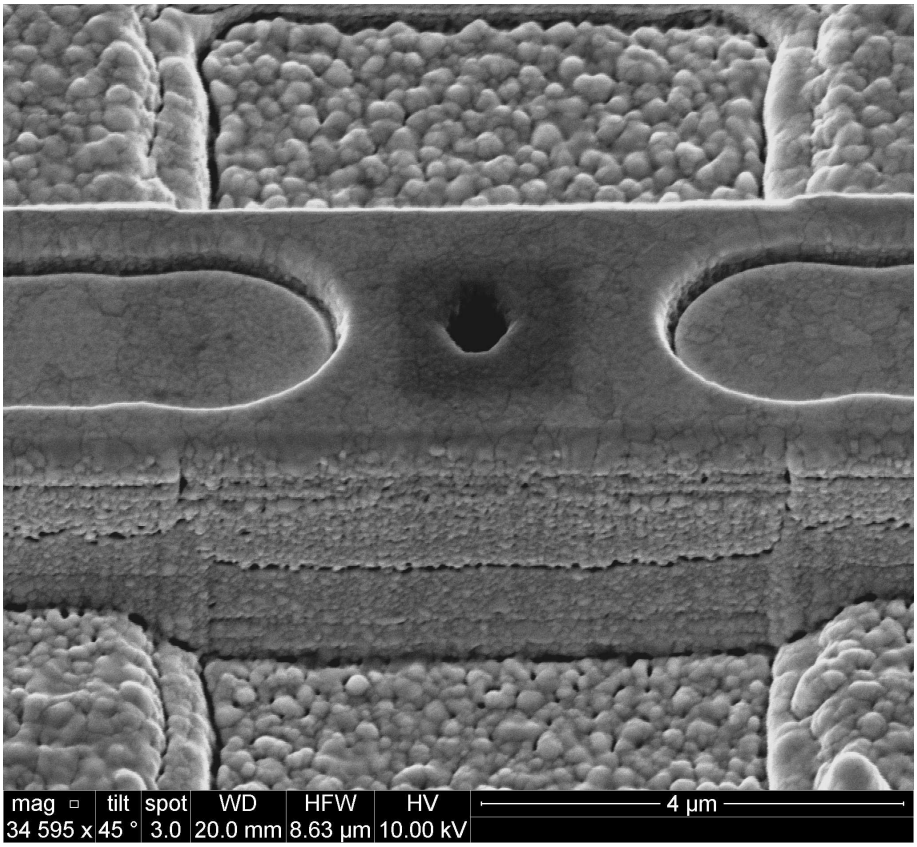

Figure 7.1: SEM image of a deeply etched pit in a waveguide

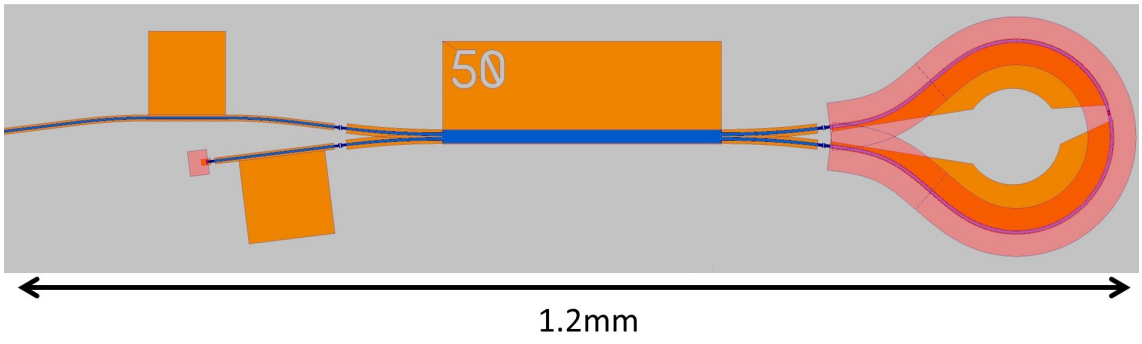

Figure 7.2: Fourth generation 2x2 "Gamma" laser schematic

intra-cavity reflector.

7.2 Device simulation

Prior to fabrication, the devices were simulated in order to predict the effect of the different features of this iteration. The simulation model used was similar

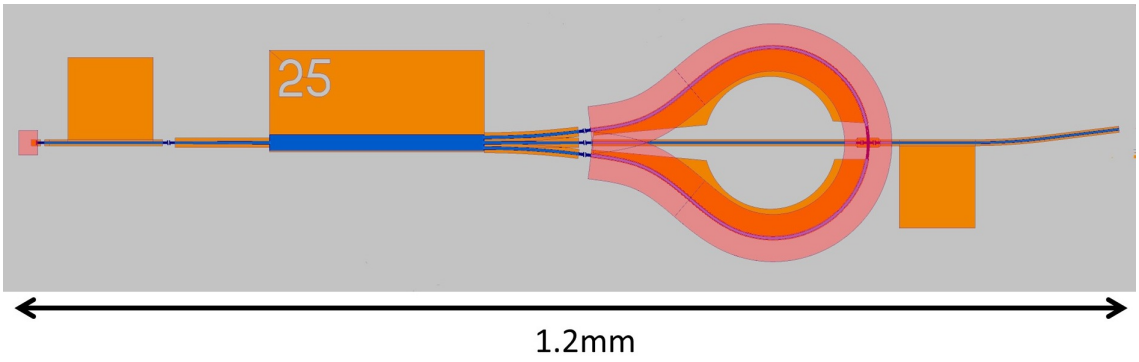

Figure 7.3: Fourth generation 1x3 "Phi" laser schematic

to that used for the previous generations, modified to accommodate the looped geometry. The main impact of the loop was the reinjection of the previously lost signal into a different port, an operation made trivial thanks to the capacity of the SMM to provide transfer functions for reflection and transmission through a section.

The 2-by-2 "Gamma" geometry was simulated with a pit positioned asymmetrically on the loop. The resulting reflection profile, shown in Figure 7.4, shows a dual cavity modulation of the spectrum. However, one can note that the modulation amplitude is small, as can be expected from a pit that has a small reflectivity. One can also observe that compared to previous generations, the general amplitude of reflection is higher, up to 0.8 where the 2x2 MMI laser without loop showed a reflection amplitude up to 0.4. This is coherent with the fact that the light is reinjected into the system, instead of being lost, at the reflection points.

In the case of the "Phi" laser, the focus was on the influence of the crossing of the loop and the output coupler. Such a crossing causes a localised refractive index change, that is likely to result in a reflection. A simulation model was developed to take this aspect into account, where a reflective feature is positioned on the loop, and also on the output coupler, to represent the effect of the crossing. The reflectivity of this element was arbitrarily set at 25%, as little information was available at this stage to predict the actual reflectivity of the crossing.

Because the loop is split into sections of equal length on each side of the crossing, it is a triple-cavity structure in which two cavities have the same length. Practically, it is a two-cavity structure, which can be observed in Figure 7.5, where the simple super-mode envelope corresponds to a dual-cavity structure.

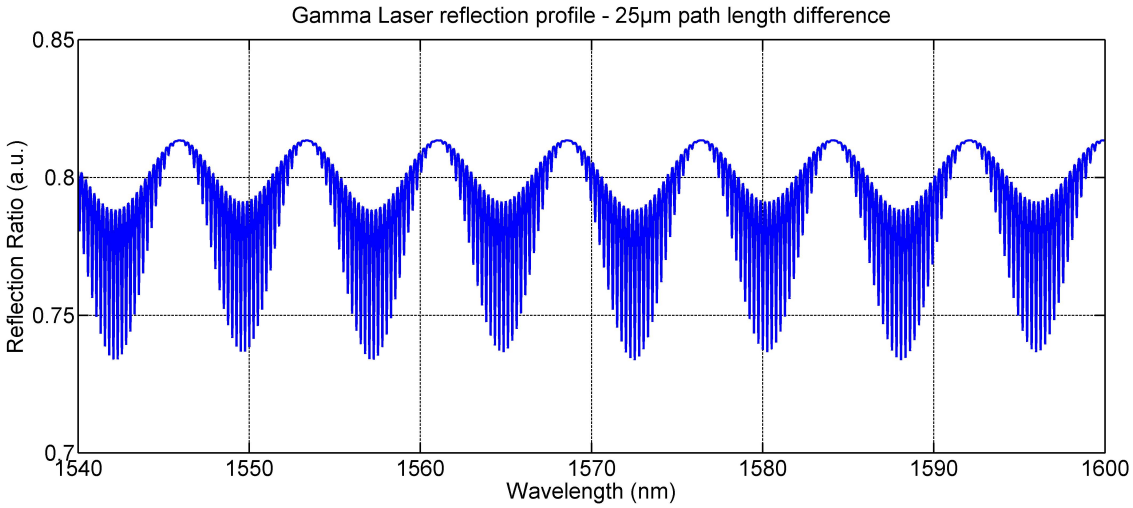

Figure 7.4: Gamma laser SMM-simulated reflection profile predicting an approximately 3nm super mode spacing

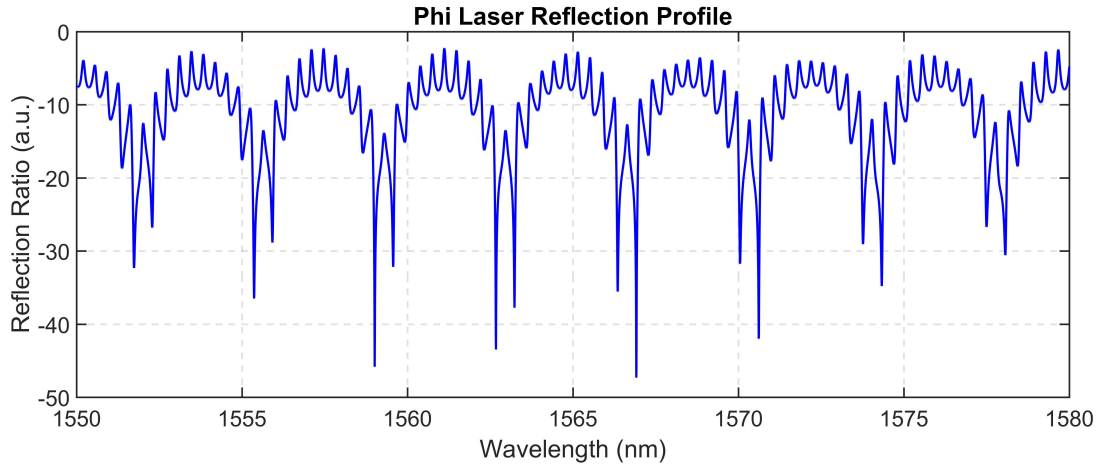

Figure 7.5: Phi laser SMM-simulated reflection profile predicting an approximately 3nm super mode spacing

7.3 Characterisation results

After fabrication, the "Gamma" laser (Figure 7.6) was tested. However, it appeared impossible to collect any laser spectrum despite the injection of currents up to 160mA for the MMI section and up to 50mA for the waveguide sections. The collected spectra corresponded to an emission below threshold (Figure 7.7). The dual-cavity behaviour, with a 2nm super-mode spacing, corresponds to a 50μm cavity length difference in a ring configuration, as caused here by the loop with pits creating a 50 μm length difference.

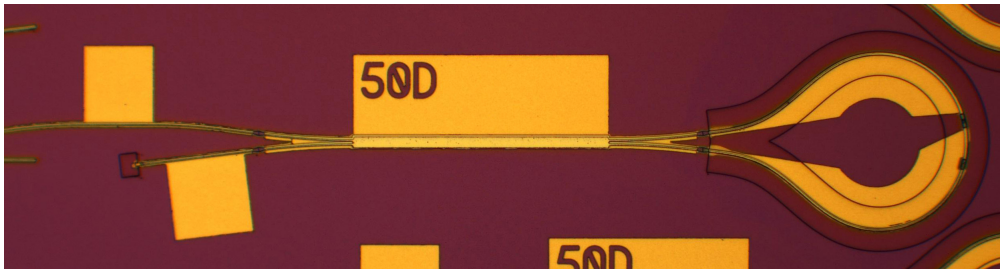

Figure 7.6: Microscope image of a fabricated Gamma laser

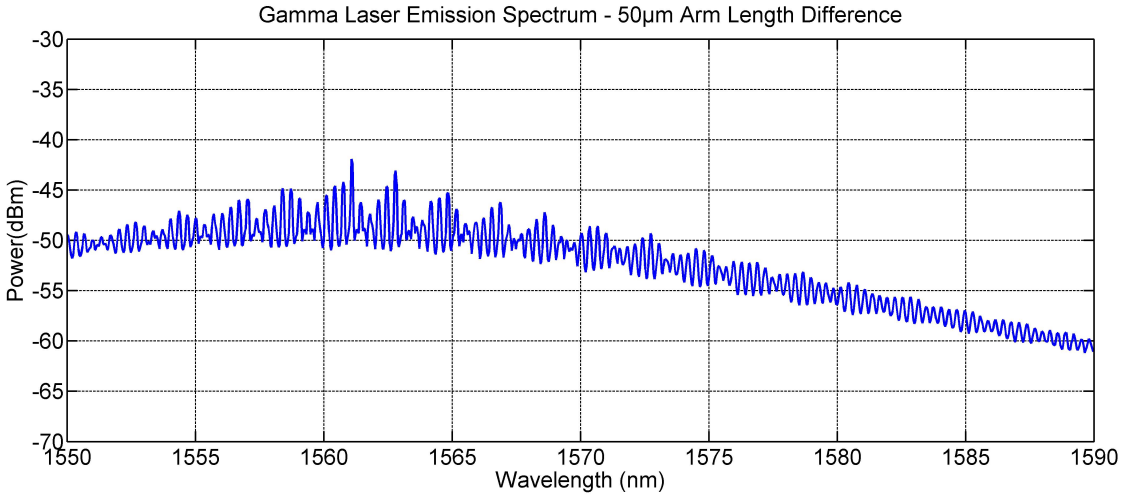

Figure 7.7: Emission spectrum of a Gamma laser showing dual-cavity behavior but no evidence of lasing

One of the possible causes of the "Gamma" device not showing any laser output, is in the MMI: due to the asymmetric geometry, the output port receives signals from the two opposite ports. However, the paths of the light coming from these ports results in a π phase difference between the two signals, caused by the MMI coupler that applies a $\pi/2$ phase shift to the signal reaching one port, compared to the signal reaching the other. The light paths from the MEF to the output port cause this relative phase shift to be applied twice to the same signal, resulting in a π phase shift. At recombination, the signals are thus in opposed phase and can interfere destructively. It is possible that the device was indeed lasing, but that the signal was contained within the cavity, while the spontaneous emission, constrained by the geometry, was the only signal leaving the device through the output coupler.

The absence of measurable lasing can also suggest that the pits used to create intra-cavity reflections and favor single mode operation, provide only a marginal reflection, insufficient to provide enought feedback to enable lasing.

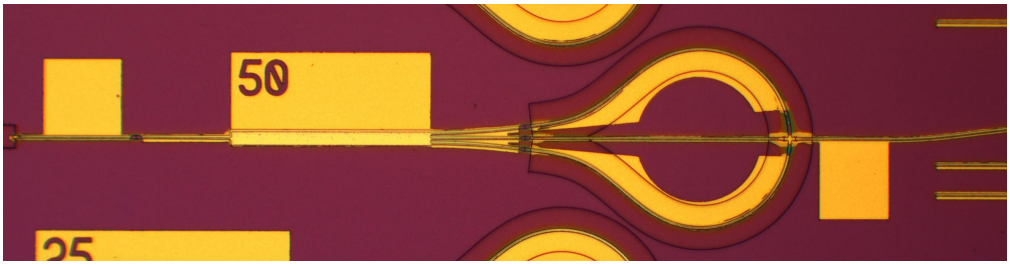

Figure 7.8: Microscope image of a fabricated Phi laser

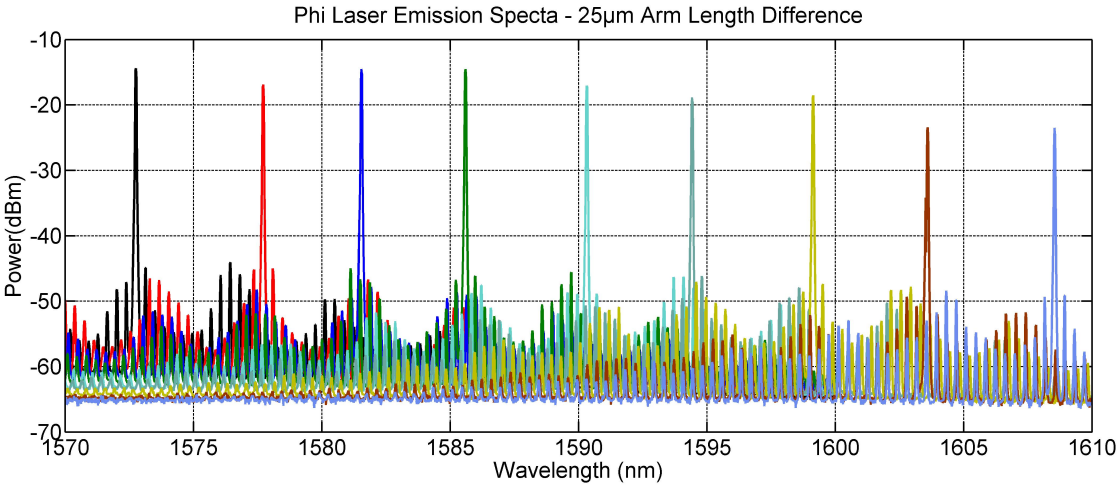

Figure 7.9: Superimposed emission spectra of a Phi laser showing a 36nm discrete tuning range and SMSR levels up to 30dB

This observation was to be confirmed by that of other members of the group who observed that a large number of pits (above 10) was necessary to provide significant reflection.

The symmetrical "Phi" structure (Figure 7.8) showed more encouraging results, and single mode lasing was successfully achieved with SMSR values of up to 30dB and approximately -10dBm total output power. The devices showed a tuning range extending from 1573nm to 1609nm (Figure 7.9); a 36nm range with a super-mode spacing corresponding to a cavity length difference of approximately 100μm in the previous generations of devices. While this length does not correspond to the position of the pits, it is close to the path length difference between the central arm and a half of the loop, until they intersect at the crossing. For the "Phi" devices, the injected currents varied from 80mA to 250mA for the MMI section, and 13mA to 71mA for the waveguide sections.

The Fourier analysis of the emission spectra confirmed this interpretation of the spectra, and agreed with the geometry of the device, as illustrated in Figure

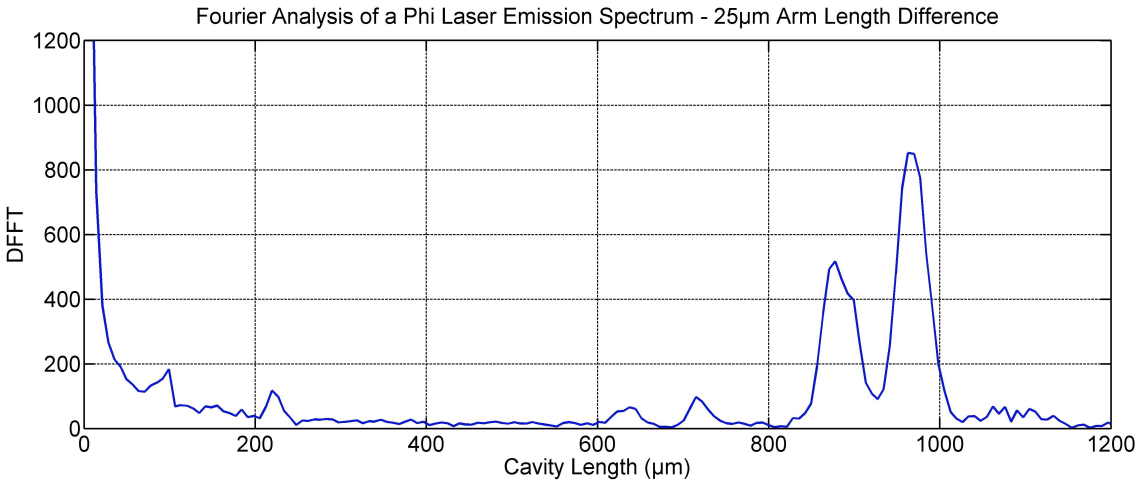

Figure 7.10: Fourier analysis of a Phi laser emission spectrum showing two main cavities but no evidence of an effect from the pit positioned at 25μm

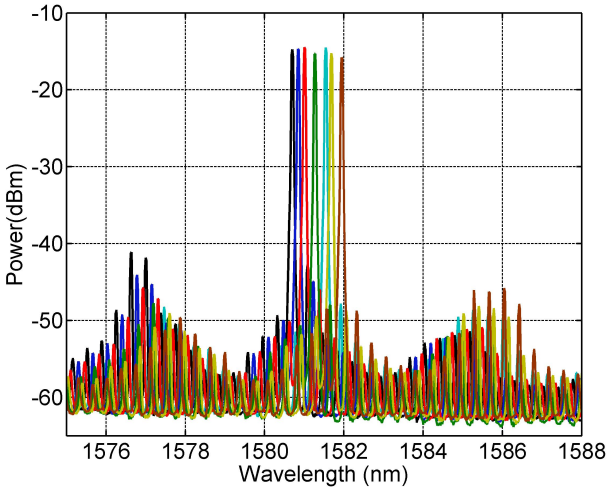

Figure 7.11: Superimposed emission spectra showing thermal tuning of a Phi laser over a 3nm range

7.10. The two large peaks separated by approximately 100μm do correspond to the two lengths indicated before, and the lower peaks are caused by the super-mode envelope of the spectrum. However, one can observe that the pit positioned to generate a 25μm length difference has no visible effect on the Fourier analysis, confirming the hypothesis that a single pit is insufficient to generate any significant reflection.

Fine tuning was also achieved by adjusting the current injected into the MMI section, with tuning ranges of up to 3nm as shown in Figure 7.11.

The comparison of the collected spectra with simulated profiles confirmed the

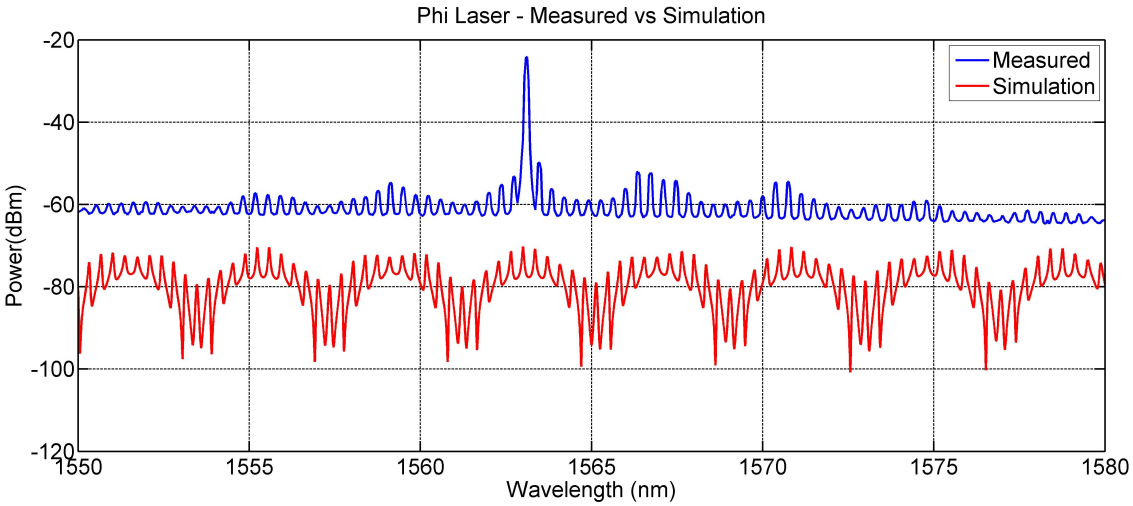

Figure 7.12: Superimposed emission spectrum of a Phi laser and corresponding SMM-simulated reflection profile showing a match in terms of super-mode spacing

validity of the simulation model prepared for this geometry, as illustrated in Figure 7.12. Indeed, it can be observed that the super-mode spacing of the simulated and collected spectra match, which is the main feature of this simulation tool: to predict the super-mode spacing. The wavelength of each maximum cannot be easily predicted, as discussed for the third generation of devices.

Despite the unconvincing results for the "Gamma" geometry, the "Phi" geometry showed encouraging results with a large tuning range and SMSR levels matching the golden standard of 30dB in use in the group, making it a design worth investigating, with an optimised loop shape to minimise the scattering losses in this part of the device.

Considering the reflection observed at the crossing in the "Phi" laser, the investigation would be oriented towards using such crossings in a similar fashion to slots, to create local reflections and achieve single mode. In addition, the particularly encouraging results of the 1x3 MMI laser from the third generation of devices made it a suitable candidate to investigate the compatibility of this design with monolithic integration. Indeed, this design matched the constraints of a cleave-free, regrowth-free and easy to fabricate device, and the following step in process optimisation was to investigate the monolithic integration of this device with other components fabricated at the same time.

Chapter 8

Fifth generation of lasers

8.1 Design and purpose

The fifth generation of devices consisted of variants of previous designs, along with test structures to investigate intra-cavity reflectors. As a consequence, the simulation of the new structures was not deemed necessary.

One of the variants that was designed for this generation was the result of a new type of curve that was developed for PICDraw, the layout design software used by the group to design lithography masks. The proposed curves had a variable radius of curvature, in an attempt to optimise the guiding of the signal and minimise bend losses in curved waveguide sections. The "Gamma" and "Phi" designs were modified to use this new type of bend instead of constant-curvature sections. The new geometries are shown in Figures 8.1 and 8.2.

Observing that the crossing in the Phi laser of the previous generation also acted

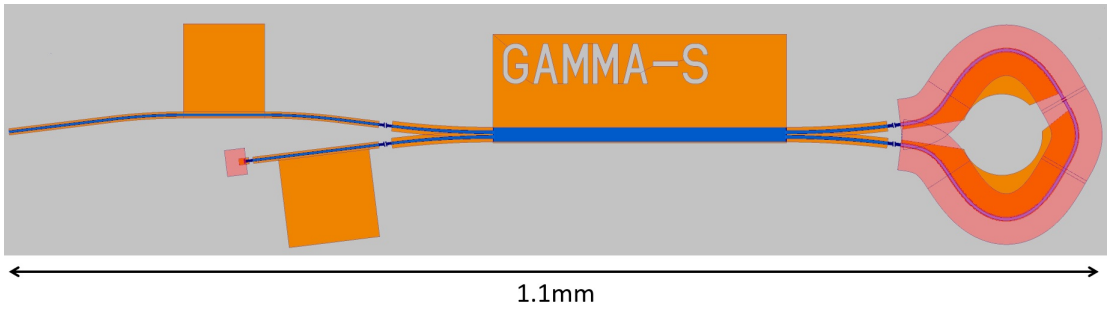

Figure 8.1: Schematic of the Gamma geometry with a variant of the curve optimised to reduce bend loss

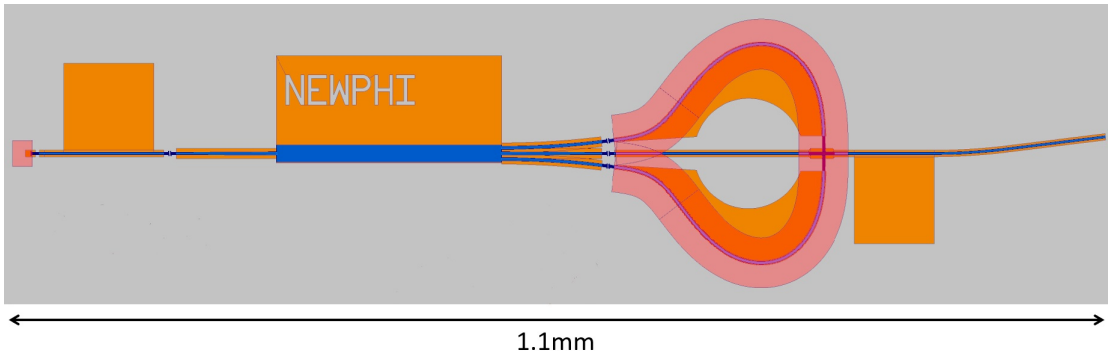

Figure 8.2: Schematic of the Phi geometry with a variant of the curve optimised to reduce bend loss

as a reflective feature, the use of localised wider waveguide sections as intra-cavity reflectors was considered. The proposed design, dubbed "T-Bar", consists of a line, perpendicular to the waveguide, etched at the same time of the ridge. The result is similar to a waveguide perpendicularly crossing the section where it is built. While the extensively used slots are a local reduction of the waveguide effective index by removal of semiconductor material, the "T-Bar" is a local increase of the index by effectively widening the waveguide. A series of Fabry-Perot lasers was included to the lithography mask, including slots for the control group, and "T-Bars" for the test group. The size of the "T-Bars" in the direction of the waveguide was 1.1μm for some of the test structures, which corresponds to 2.5 times the wavelength in the material, of the 1550nm wavelength in vacuum. The other test structures used a 1.35μm size, corresponding to 3 times the wavelength in the material. These two variants were included in case the two localised index changes, at the beginning and end of the reflector, could interfere constructively or destructively. In order to increase the effective index contrast between the reflector and the rest of the waveguide and to maintain similarity with the initial "Phi" design, the Fabry-Perot section was deeply etched. A schematic of such a "T-Bar" is shown in Figure 8.3.

Finally, in an attempt to determine if the 1x3 MMI laser presented in Chapter 7 was indeed compatible with monolithic integration of other components, a pseudo-EAM section was added to the design to form an electro-absorption modulated laser (EML). The laser being a source of heat that could potentially disturb the function of the EAM section, a set of deeply etched trenches were added to the design in an attempt to increase the thermal isolation between the EAM and the laser; especially the MMI section where the highest currents are injected. In addition to this isolation, some metal pads were extended with the

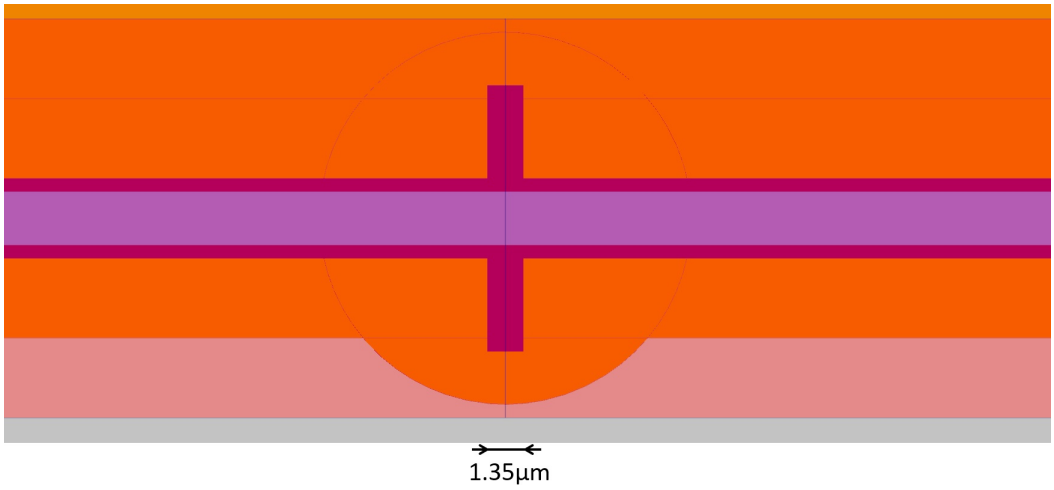

Figure 8.3: Schematic of a proposed intra-cavity reflector of width 1.35μm

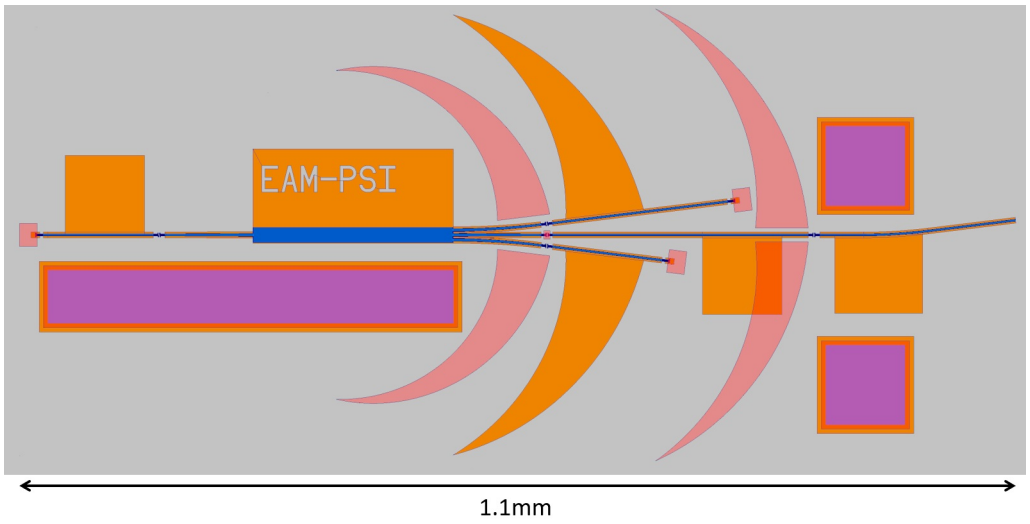

Figure 8.4: Schematic of a 1x3 MMI EML

aim of guiding the heat away from the waveguide and to favor its dissipation. The resulting proposed geometry is shown in Figure 8.4. The EAM section was completed by two top-side N-contact pads to accommodate RF probes in case the opportunity of RF testing would arise. Given that those designs were based on a laser that was previously studied, no particular simulation was deemed necessary at this stage.

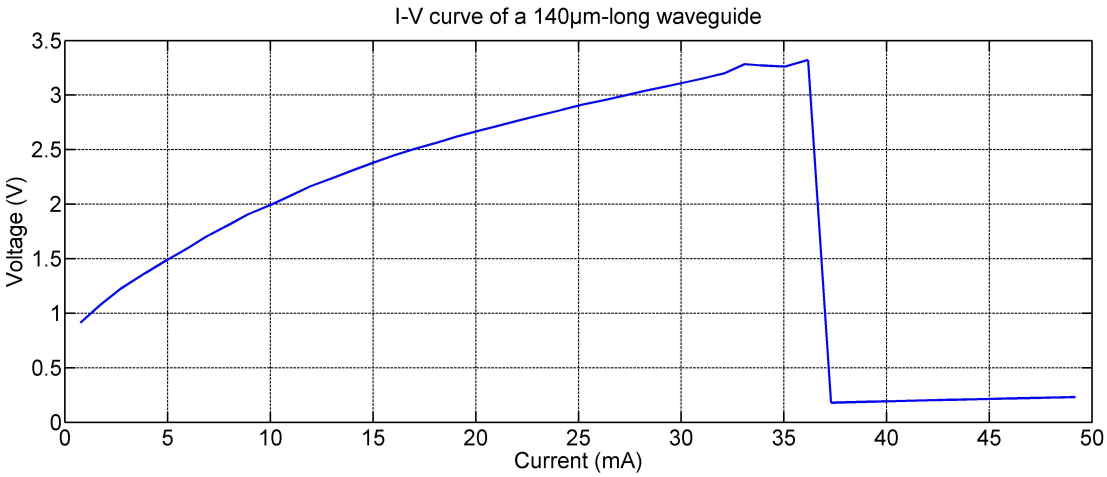

Figure 8.5: I-V scan of a waveguide section showing high resistivity and failure at 36mA while it should have sustained at least 50mA before failure

8.2 Difficulties during fabrication procedure

The fabrication of this generation of devices, along with the other devices from this standard shared run, proved difficult and eventually took more than half of the year 2017 with the multiple re-runs that were done. Indeed, a number of technical difficulties occurred, as summarised here.

During the first attempt at fabricating the devices, no incident was noticed during the fabrication itself. However, upon testing the devices, it was observed by all the people who had samples made in this run that the devices were prone to burning. The initial I-V testing of any section of the devices showed extremely high resistivity, reaching voltages higher than 3V at currents where between 1.2V and 1.5V would be expected, given the length of the section tested. This is illustrated in Figure 8.5 where a 140μm long section of waveguide showed alarmingly high voltages during an I-V scan, and eventually failing at approximately 36mA injected current. In normal conditions, a section of this length would have been expected to sustain at least 50mA before reaching the usual compliance voltage of 2.5V set for the current sources used in the characterisation procedure. Indeed, from practical experience it is considered in the group that voltages above 3V are dangerous for the section that can overheat and fail. This is why a compliance voltage is used in the current sources, diverting any current that would bring the section above the selected voltage limit.

A standard testing procedure used during the fabrication consisted of applying a voltage between large contact structures at different distances from each

other to determine the contact resistance of the metal layer. The current flows through the P-doped top of the wafer, from one large contact area to the next. During this test, the desired contact resistance was between 1E-8 and 1E-6 Ω/cm. Any higher value suggests a high contact resistance that can usually be mitigated by annealing the chip. During this run, the values recorded were within the normal range. As this is a quick verification test, the exact values were usually not recorded unless they were abnormal.

However, the damage appeared obvious when the chips were inspected under a microscope, as illustrated in Figure 8.6. It can be noted that the damage is localised to specific points along the waveguide, rather than over extended areas. This observation, along with the high contact resistance that was recorded during the characterisation procedure, led to the hypothesis that some form of insulating layer was present between the semiconductor surface and the contact metal. Cross-sectional SEM imaging showed no visible evidence of such a layer, indicating that if there was any, it was too thin to be visible using the SEM. Independently from the cause, the electrical isolation between the semiconductor and the metal was not complete, as suggested by the tests performed during fabrication. Instead, it was supposed that contact was possible in local spots, sufficient to perform tests during the fabrication run, but too small and not frequent enough to evenly spread the injected current into a section of the waveguide. This could result in a concentration of the current in specific positions, causing a localised overheating and eventually failure of the section, such as the one observed under the microscope.

The most likely explanation at this stage was that polymer from the lithography procedure was still present on the ridges, creating a thin insulating layer. A second run was thus started, where stronger cleaning procedures would be used at this stage of the process in order to ensure no photoresist would be left in areas that should be clear.

During the second run, the annealing revealed a fault of the PECVD oxide deposition. Indeed, after extracting the chips from the annealing oven, it was observed that the oxide layer was blistered, with blisters that cracked when manipulating the chip, as illustrated on Figure 8.7. The function of this layer was to protect the semiconductor and to electrically isolate the contact pads from the substrate to prevent leakage.

Initial testing of the devices from this run showed that considerable amounts of current (hundreds of mA) were necessary to achieve voltages typical of lasing

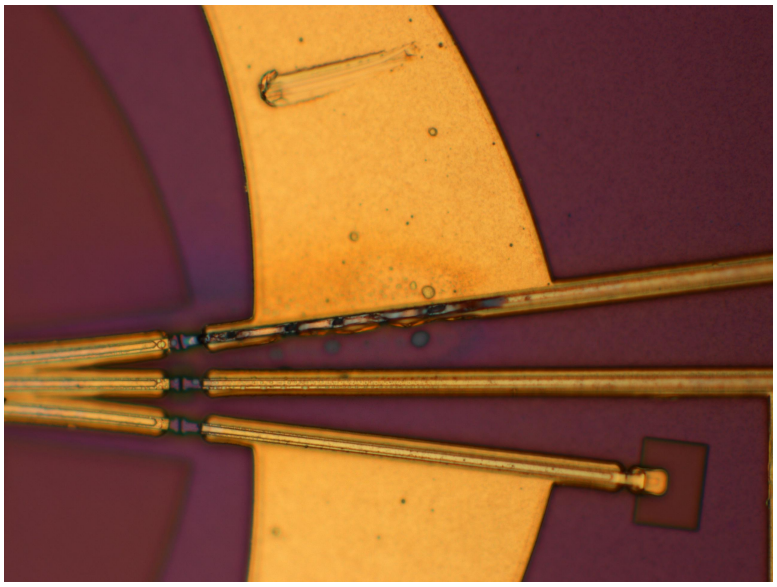

Figure 8.6: Microscope image of a waveguide showing damage at specific points along the section suggesting a local high current density heating up the device to the point of damaging it

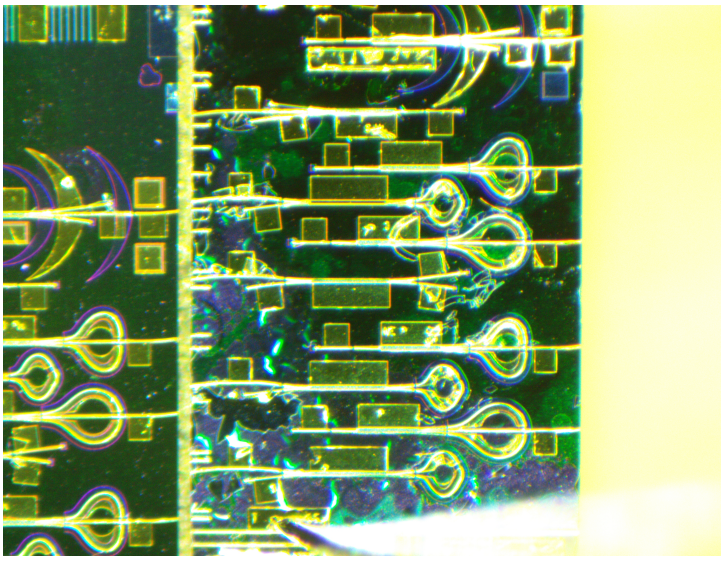

Figure 8.7: Microscope image of a chip with blistered oxide - those cracks in the passivation layer can compromise the isolation and cause leaks, reducing the current reaching the ridge

condition (1.2 to 1.5V). However, this was insufficient to get past threshold, suggesting that the broken isolation layer resulted in leakage of the current from the contact pads directly into the chip, while only a fraction of the current was flowing through the ridge; insufficient to result in a working device.

The most likely explanation was that the PECVD equipment, a very old machine, was not reliable and it was decided to proceed to a new run, this time using sputtering rather than PECVD to deposit the oxide and nitride layers. This third run did not result in any blisters at the surface of the chips, but the different deposition technique resulted in a porous isolation layer. Consequently, leakage was observed upon testing the devices.

In the meantime, the PECVD machine had been under maintenance, so a re-run was performed. However, a malfunction of the metal evaporator used until then forced the use of an alternative machine. But, this machine was not able to achieve the same deposition quality, and the 360° rotation tool used to guarantee metal coverage of the side walls, was not available. As a result, as shown in Figure 8.8, the ridges caused a shadow in the metal evaporation, preventing metal from depositing directly on the side walls of certain sections. This break in the connection between the contact pads and the ridges meant that it was not possible to power sections of the devices, effectively disabling them.

After repair of the metal evaporation tool, it was decided to make another attempt, using the experience gathered from the failed runs to mitigate the risks of encountering these failure modes again. This was the first trial of the metal-first fabrication technique described in Chapter 3. By depositing a layer of metal on the chip before any other processing, a conductive layer was created. Beyond the protective aspect, this conductive layer was used to ensure that, in the case of imperfect contact between the contact metal layer and the metal-covered semiconductor, this thin layer would help spread the current along the waveguide before reaching the semiconductor, reducing the risk of catastrophic overheating. Before proceeding with the active material, test runs were performed with InP wafers, resulting in the alternative fabrication process detailed in Chapter 2. The resulting chips were examined in the SEM, and it could be observed that despite a slight wall roughness that could result in scattering losses, metal redeposition was practically nonexistent, as shown in Figure 8.9. An hypothesis on the origin of this side wall roughness is that because the ICP oxide etch is not rigorously isotropic, the metal layer could have been partially undercut, resulting in the semiconductor being exposed at the time of the

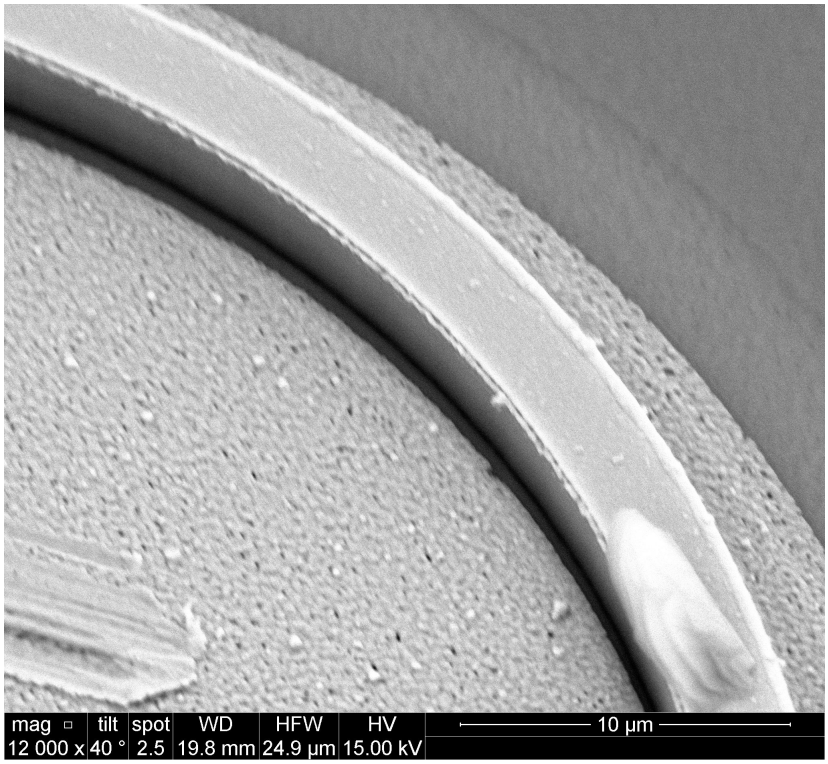

Figure 8.8: SEM image of a processed chip with shadowing of the metal along the wall and damage to the ridge after an attempt at probing it directly. One can also observe that the metal layer does not appear as smooth and thick as would be expected, suggesting a general malfunction of the metal evaporator

semiconductor etch despite the oxide cap layer used to shape the ridge level.

The metal recipe selected for this fabrication was that used during the initial testing of the method: Ti:Au:Ti (25:50:25nm). In addition, a stronger cleaning procedure was used to remove any remaining photoresist from the ridge, to further reduce the risk of having poor contact quality. At this stage, the focus was less on finding the exact cause of the multiple failure modes encountered so far, and more on having a successful fabrication to provide much needed samples for the group. As a result, no "intermediate" samples were processed to separately validate one or the other of the workarounds put in place.

It is noteworthy that because of the geometry used for the contact test performed before annealing, the presence of the initial metal layer prevented the measurements of significant data from the test. Indeed, the current would flow through this layer instead of flowing through the semiconductor itself, preventing the acquisition of any information on the metal/semiconductor interface resistivity.

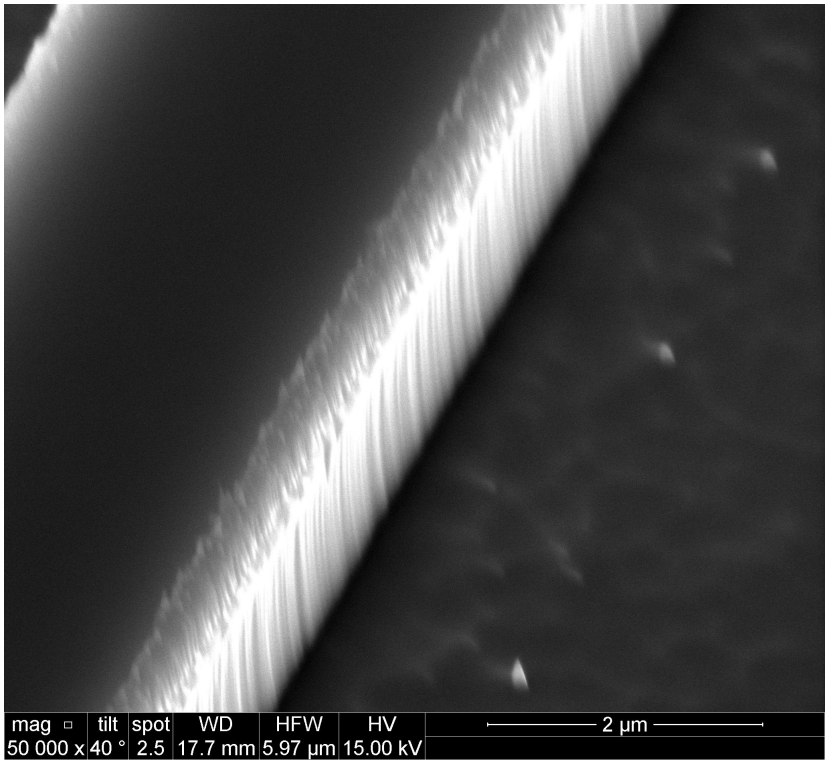

Figure 8.9: SEM image of a metal-first process test chip showing slight wall roughness and negligible metal redeposition

Due to this choice, the fabrication did not bring detailed answers on the exact cause of the failures, but the run proved successful, and most of the delivered devices functioned enough to undergo proper characterisation. Throughout this succession of fabrication runs, the accumulated experience and desire to get results in time led to a streamlining of the fabrication procedure. By optimising the work in terms of planning as well as fabrication methods, a record fabrication time of 4 days was achieved.

8.3 Characterisation results

Due to the side wall roughness observed during the fabrication procedure, the scattering losses limited the performance of the devices from this run. In order to achieve lasing, the characterisation had to be performed at 10°C instead of the 20°C used so far.

Similarly to the previous run, the "Gamma" structures showed no significant output, and no lasing was achieved with either the standard or the optimised

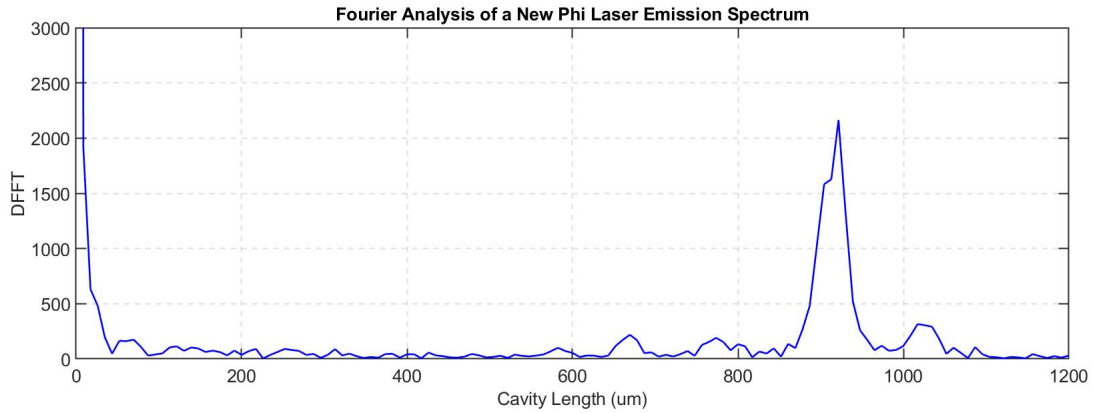

Figure 8.10: FFT analysis of a new Phi laser emission showing one main cavity and residual additional reflections

curvature versions.

Lasing was achieved with the initial "Phi" structure, with significantly degraded performance compared to the previous run: total output powers below -30dBm were obtained, only three super-modes could be reached by tuning the device, and the SMSR was under 20dB, evidence of the poor performance of the laser during this fabrication run. The new "Phi" structure with optimised curves was not able to lase, but the emission spectrum showed the envelope typical of dual-cavity behavior. The Fourier analysis of the emission spectrum, shown in Figure 8.10, shows a main cavity corresponding to the central arm of the structure, and a faint reflection corresponding to a length matching the path following the curve to the crossing. Other members of the group had confirmed that the new optimised bends showed indeed a performance similar to or better than standard bends, so a possible explanation could be that the curve was too sharp, resulting in excessive scattering losses and preventing lasing. Similarly to the previous generation, currents up to 160mA were injected into the MMI sections, and up to 60mA for the waveguide sections. For the absoprtion section of the EML, the applied bias ranged from 0V to -1.5V.

The Fabry-Perot test structures were characterised to determine the effect of the "T-Bar" reflector. Starting with the slotted control devices, the Fourier analysis (Figure 8.11) of the lasers showed a 700μm cavity matching the length of the full laser, as well as two peaks at 260 and 440μm corresponding to the cavity lengths on each side of the separation slot. This was used as a point of comparison for the analysis of the two "T-Bar" variants.

Both the 1.1 and 1.35μm variants of the "T-Bar" lasers had typical Fabry-Perot

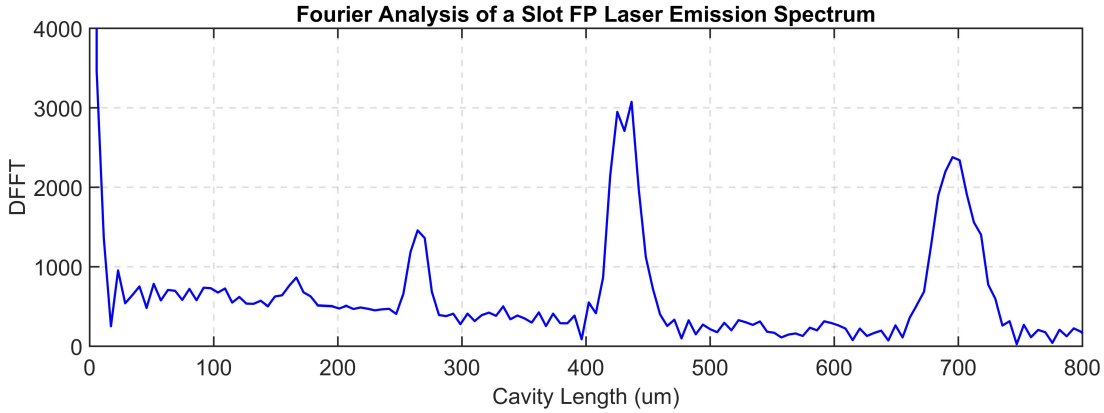

Figure 8.11: Fourier analysis of a Fabry-Perot laser with a slot showing the full cavity length and the two subcavities

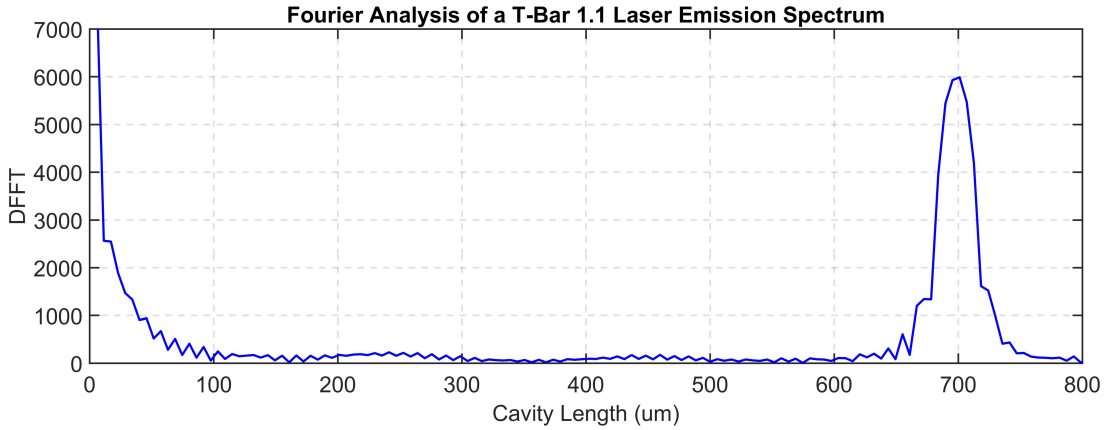

Figure 8.12: Fourier analysis of a Fabry-Perot laser with a 1.1μm T-bar showing the main cavity and no reflection from the T-bar

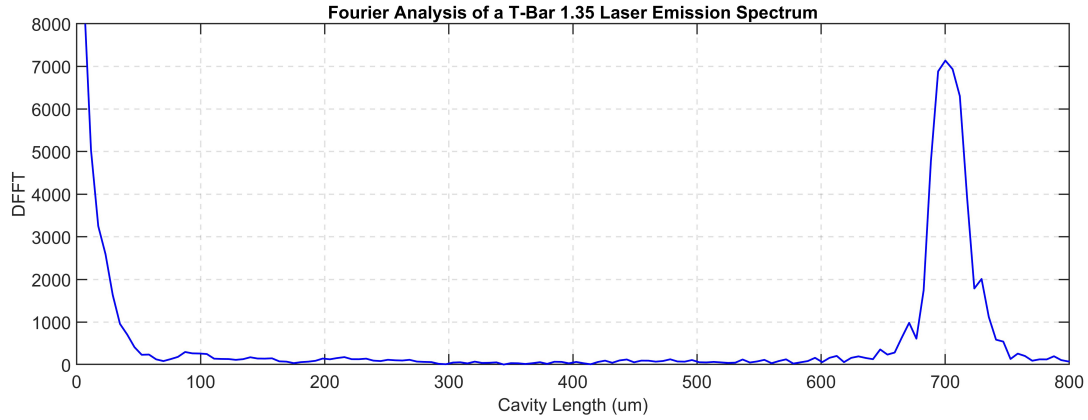

Figure 8.13: Fourier analysis of a Fabry-Perot laser with a 1.35μm T-bar showing the main cavity and no reflection from the T-bar

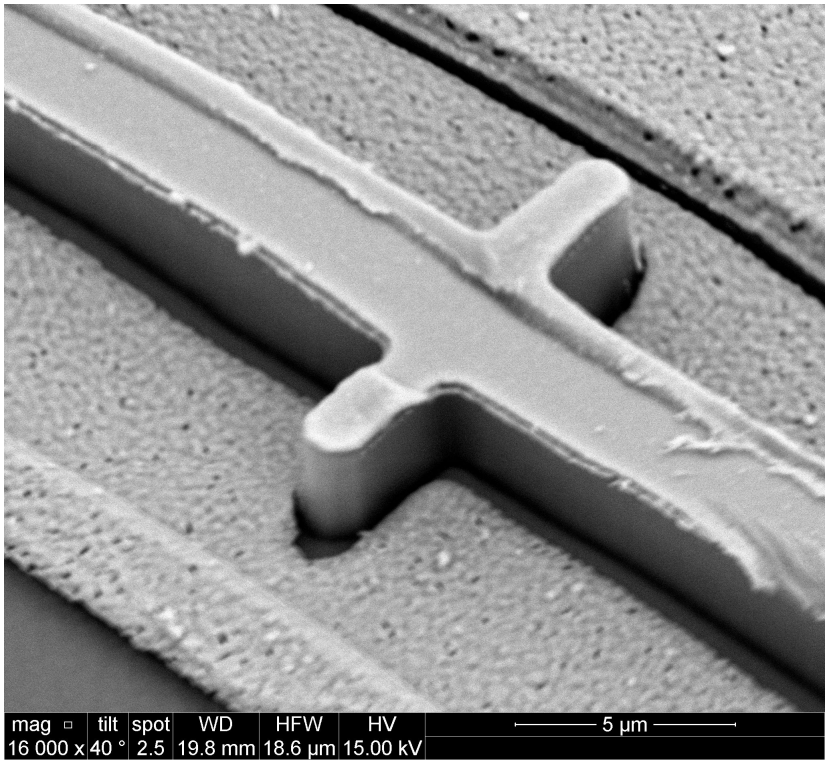

Figure 8.14: SEM image of a "T-Bar" showing an offset of the oxide opening and a shadowing effect caused by the ridge during metal deposition, compromising electrical connection

laser emissions. The Fourier analysis of the emission spectra showed no evidence of an effect of the reflector, as can be seen in Figures 8.12 and 8.13.

The study of the "T-Bar", although not fruitful in the attempt at designing a reflector variant, yielded another finding. Indeed, upon SEM observation of the structure, it could be observed (Figure 8.14) that an offset in the oxide opening was clearly visible, the transverse ridge making it possible to see by how much the oxide opening was misaligned. This finding was put to use in the following generation, as will be described in the next chapter.

The 1x3 MMI EML, however, showed encouraging behavior. The tuning range of the laser was limited to two super-modes, similarly to the "Phi" laser that showed significantly less tunability than in the previous fabrication run. But the negative biasing of the EAM section showed encouraging performance, with an absorption of 10dB measured between 0V and -1.5V biases, as illustrated in Figure 8.15.

In summary, this generation brought encouraging results for the integration of an EAM section with MMI lasers, despite the generally poor performance of

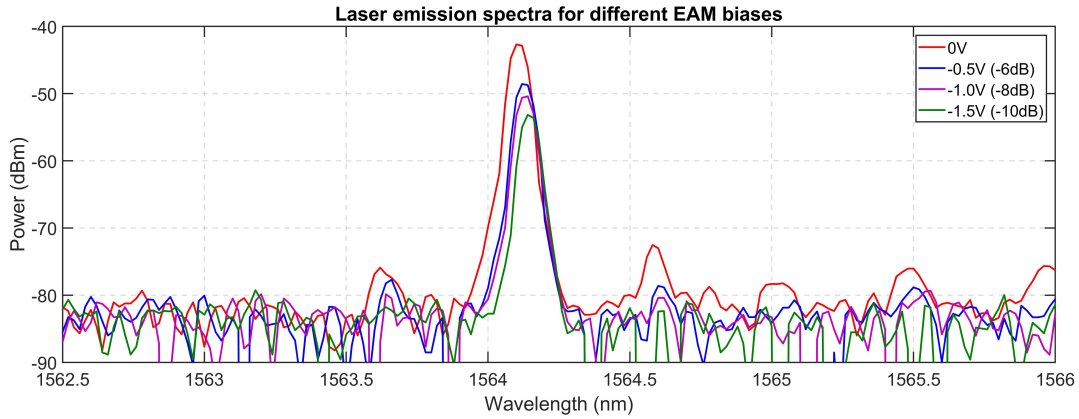

Figure 8.15: Superimposed laser emission spectra of a 1x3 MMI EML for different EAM biases showing an extinction of 10dB at -1.5V bias, relatively to the 0V bias

the devices during this run. The "T-Bar" reflector showed no significant effect, and it was decided to not pursue the investigation of this feature at this stage. However, the fabrication difficulties were the opportunity to further improve the fabrication methods, and to develop the metal-first fabrication variant.

Considering the general poor performance of these devices but the encouraging results of the new fabrication process, the effort was then oriented towards validating existing structures when monolithically integrated with other components, and towards refining the fabrication procedure for more repeatability and process result stability.

Chapter 9

Sixth generation of lasers

9.1 Design and purpose

The sixth and final generation of devices presented in this work consisted primarily in selecting the most promising design identified, and to integrate it with additional components and thus determine if the proposed design can indeed be monolithically integrated, such that a functional PIC can be fabricated as one unit rather than discrete components assembled afterwards. The 1x3 MMI laser developed with the third generation of devices was deemed the most promising geometry, and was selected for this part of the work. The two additional components that were selected to be integrated with the laser are an absorbing section to be used as an EAM, and a gain-switched Fabry-Perot slave laser to be used as a comb generation device. The two PICs would thus form monolithically integrated EMLs and comb sources that can be tuned in wavelength, and fabricated using a simplified, industry-friendly process. The two proposed geometries are shown in Figures 9.1 and 9.2.

Additional variants of the 1x3 MMI laser and of the corresponding EML were also designed, with the aim of creating a packaging-friendly geometry. Following the PixApp [53] guidelines, a photonics packaging pilot line project developed in the same laboratory, an asymmetric version of the 1x3 MMI laser was designed, so that all the contact pads could be positioned on the same side of the laser. Not only does it make it compatible with the use of a multi-contact probe (MCP), but it also complies with the PixApp design rules for packaged PICs, where all the electrical connections need to be on the same side of the semiconductor chip, for easy connection with the package. The resulting ge-

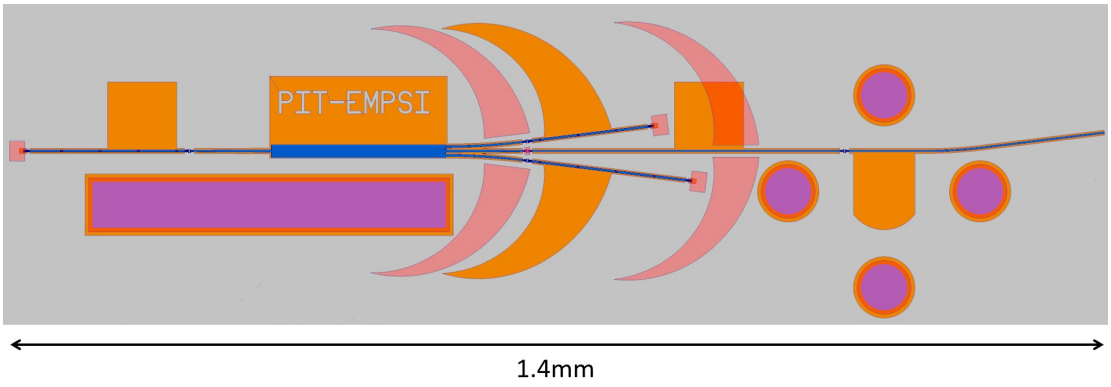

Figure 9.1: Schematic of a 1x3 MMI laser integrated with an EAM section - the multiple circular top-side N contact are here to accommodate high-speed probes coming from different directions to facilitate the probing of the pads

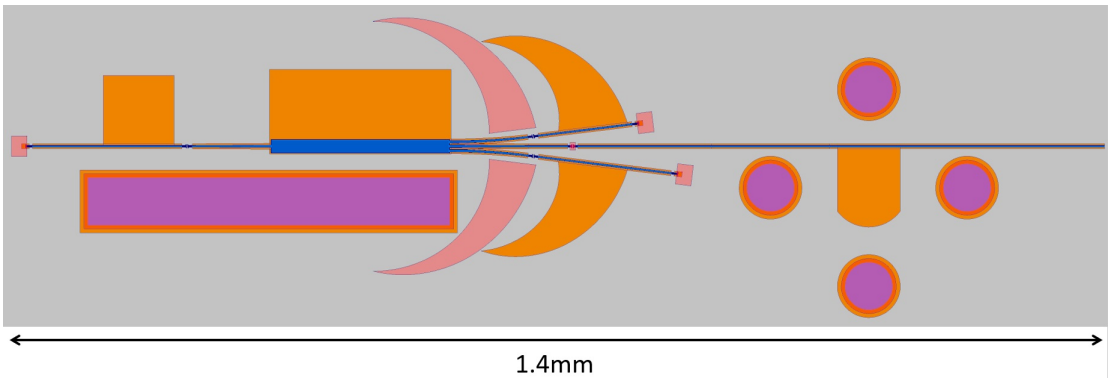

Figure 9.2: Schematic of a 1x3 MMI laser integrated with a comb generation section

ometries are shown in Figures 9.3 and 9.4.

Finally, variants of both the symmetric and asymmetric structures described above were designed, where multiple pits were etched in the different arms of the structure, separated by a distance equal to the main cavity length difference. The objective of this variant was to determine if several pits could form a high-order grating and improve the mode selectivity, where a single pit showed no meaningful effect. The comparison of the SMSR and the Fourier analysis of the emission spectra with and without pits would be used as the test to validate this variant.

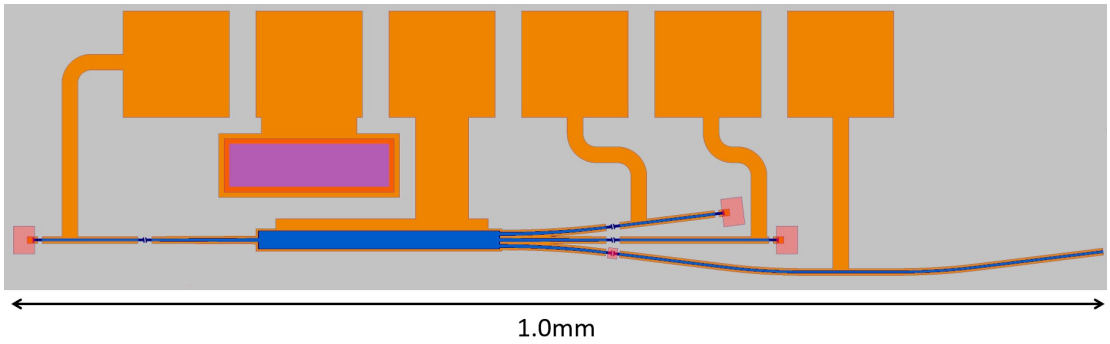

Figure 9.3: Schematic of a 1x3 MMI laser - MCP variant

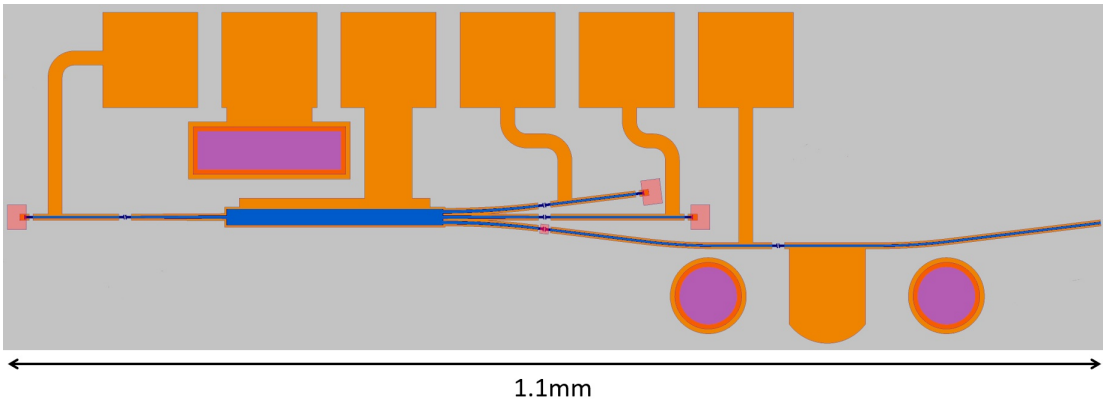

Figure 9.4: Schematic of a 1x3 MMI EML - MCP variant

9.2 Further improvements to the fabrication procedure

As indicated in the previous chapter, the "T-Bar" structures, despite not being validated as intra-cavity reflectors, led to the addition of a structure used to support the fabrication procedure. This structure can be used as a visual aid by the operators, at the oxide opening lithography step, to verify the correct alignment after resist development, but before etching the silicon oxide. The structure takes the form of several crosses where two ridges are crossing, followed by an oxide opening on one of the two ridges. The ridges are defined at the same step as the waveguides, and the oxide opening at the same step as the oxide opening on the devices, so no additional step is necessary in the process. By using a set of those crosses where the oxide opening is oriented in different directions, the operator can control the correct alignment of the oxide opening in X and Y directions. A number of such structures were scattered over the samples so that the alignment can be verified at different places of the sample.

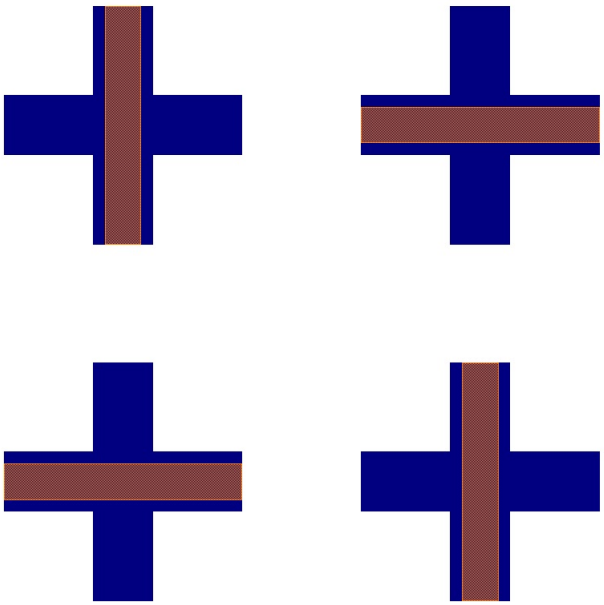

Figure 9.5: Oxide opening alignment verification structure schematic for visual inspection after lithography

The schematic of the proposed structures can be seen in Figure 9.5.

After lithography and development, and at any point later in the process, the oxide open alignment can be verified by using an optical microscope, as illustrated in Figure 9.6. This replaces advantageously the previous verification that consisted in using SEM imaging after oxide ICP etch and resist removal (photoresist is damaged by the electron beam). With this method, the verification can be performed immediately after lithography, reducing the number of steps required to correct the problem in case of misalignment: if the problem was identified using SEM imaging, the oxide layer would have to be removed (with the risk of damaging the wafer surface), a new one deposited and the lithography would need to be done again. On the other hand, this test is done earlier and only the lithography needs to be re-done if the verification shows a misalignment.

For this fabrication run, the initial layer of metal was made thinner than before. This decision was made in an attempt to reduce scattering losses, in case the metal layer was indeed the cause of the side wall roughness observed previously. The recipe used this time was Ti:Au:Ti (15:30:15nm).

Once the deep and shallow regions were etched, the remaining oxide was removed before a fresh layer was deposited. At this stage, SEM imaging of the

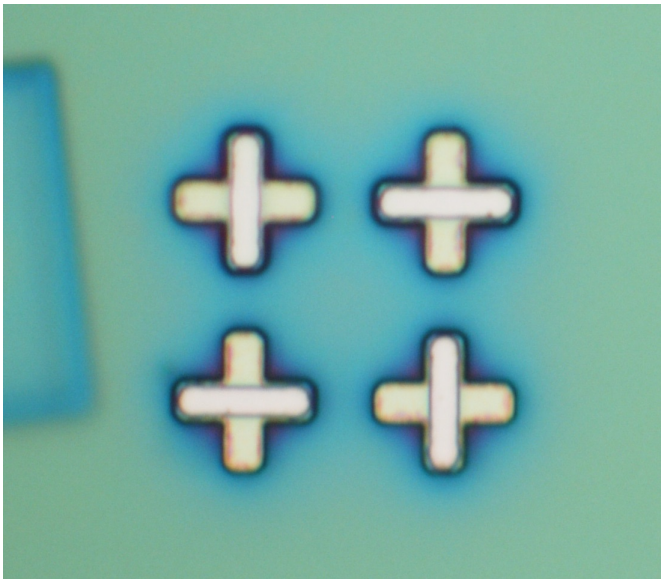

Figure 9.6: Microscope image of oxide open alignment verification structures after complete fabrication, here showing satisfying alignment in both X and Y directions

sample was performed, to examine the side walls and if there was any evidence of meta re-deposition. The SEM images such as Figure 9.7 showed that the side walls were smooth, and no evidence of redeposition was found. It was noticed, however, that the metal layer had been partially etched in the deep regions of the sample. This is due to the oxide thickness difference between the shallow and deep regions. Indeed, the deep semiconductor etch recipe also etches oxide, thinning the ridge definition oxide layer in deep areas, while the shallow areas are protected by nitride. After the shallow etch, the oxide is etched using ICP until it is all removed. However, because it is thinner in deep areas, the oxide is etched away and the underlying metal is being etched until the remainder of the oxide in shallow areas is fully removed. Such a phenomenon was not noticed before the usage of the metal first recipe, because the oxide removal was performed by a selective wet etch. But the oxide etchant is also extremely agressive in etching titanium, making it incompatible with this new variant of the process. Despite this phenomenon that had not been accounted for, a layer of metal was still present even in deeply etched areas, so the process was continued.

In the previous fabrication runs, the control of the etch depth for shallow regions was performed by etching for a small duration, then measuring the etch depth, and repeating until the desired depth was reached. However, the etch

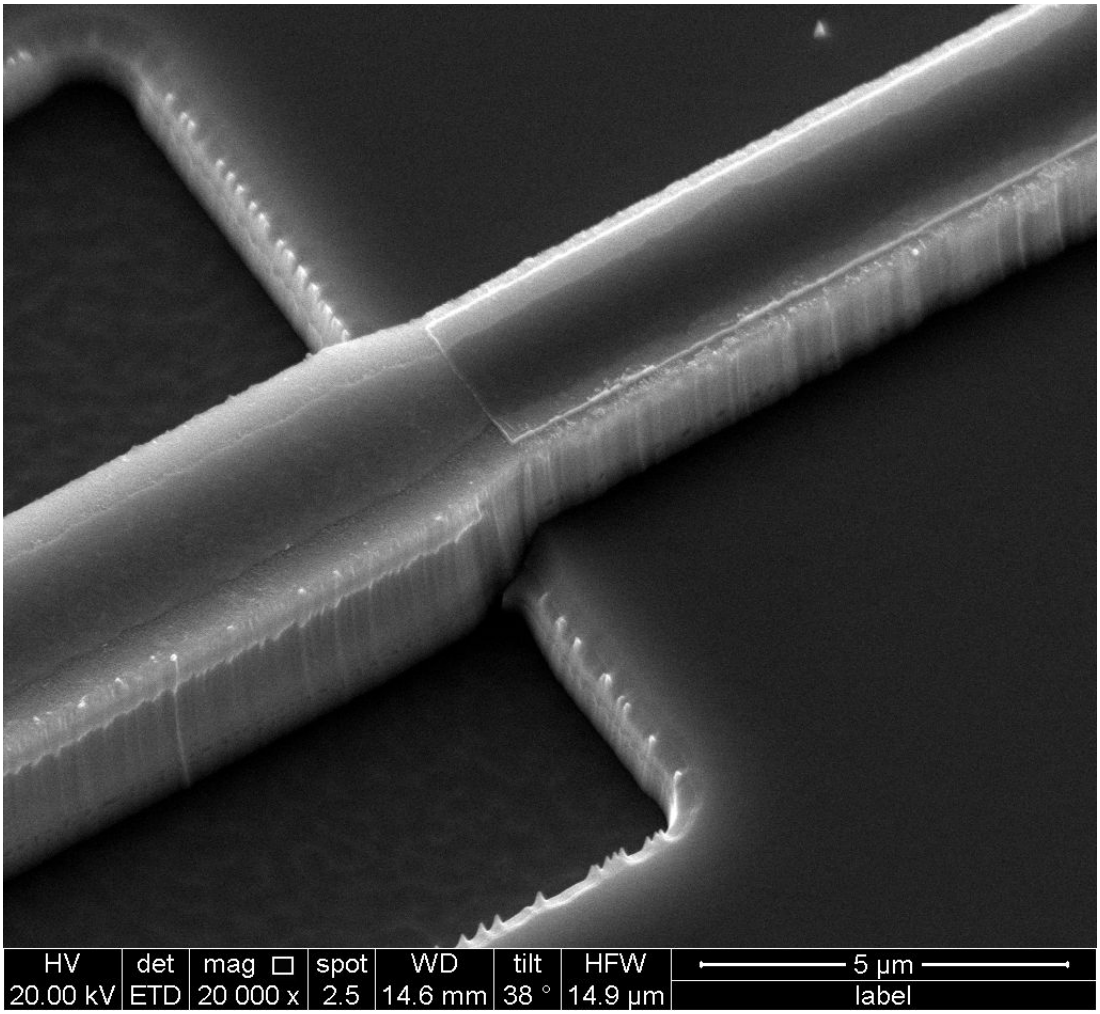

Figure 9.7: SEM image of a ridge with shallow and deep etch depths showing smooth side walls, no noticeable metal redeposition, and partial etch of the metal cap on the ridge in the deeply etched area

rate being variable, it appeared difficult to have fine control of the etch depth. This is why initially, the shallow etch was finished with a wet etch that would be limited by an etch-stop layer in the epitaxial structure. However, with the removal of the wet etch step, the precision of the shallow etch degraded, with an uncertainty of several hundreds of nanometers.

For this run, another approach was used. The semiconductor etching tool was equipped with an endpoint detection system that uses the reflection of a laser directed at the sample to monitor etch depth using interference from the different layers of the sample. At the time of the deep etch, the monitoring system was activated, and the etch continued until the quantum wells were fully etched, leading to the reflection profile shown in Figure 9.8. From this graph,

it was possible to have a record of the reflection profile that could be used to determine when to stop the etch at the shallow step, so that the right depth is reached. After experimenting with other samples to determine how fast the etch stopped after the interrupt command was sent to the machine, it was possible to determine at which interference fringe the interruption command should be sent so that the etch would stop at the level of the etch-stop layer, with a precision of approximately 50nm after some practice. In the case of this run, the measured etch depth was 1830nm for a target of 1800nm.

Due to the uncertainty in the exact layer thickness of the epitaxial structure from one wafer to another, it was decided to systematically use the endpoint detection and an initial deep etch past the quantum wells. By doing so, in the case of a thickness variation leading to a different number of fringes for a different wafer, the initial profile can be used to target the right fringe and not interrupt the etch too early or too late. Indeed, once the profile is known by monitoring the deep etch, it is possible to use the freshly acquired data to more accurately reach the target depth for the shallow etch. Using this technique to reduce the variability of the etch depth is particularly beneficial to the process result stability and repeatability, a crucial point in industry.

9.3 Characterisation results

The initial testing of this generation of devices showed improved performance compared to the previous generation, in terms of SMSR and tunability. A record discrete tuning range of 51nm was achieved for an MCP variant of the 1x3 MMI laser, as illustrated in Figure 9.9. The devices tested all showed SMSR levels between 30 and 35dB, meeting the golden standard of 30dB of use in the group, despite relatively low total output powers with under -25dBm being collected with the lensed fibre. The testing of multiple iterations of the devices showed no evidence of any significant impact of the pits on SMSR or tuning range. For this set of lasers, currents up to 160mA were injected into the MMI sections, and up to 60mA for the waveguide sections. For the absoprtion section of the EML, the applied bias ranged from 0V to -3V.

Beyond the verification of tunability and SMSR, the focus of this generation was on integrating the laser that had been extensively studied on its own, with EAM and comb generation sections. For the comb generation, a gain-switched

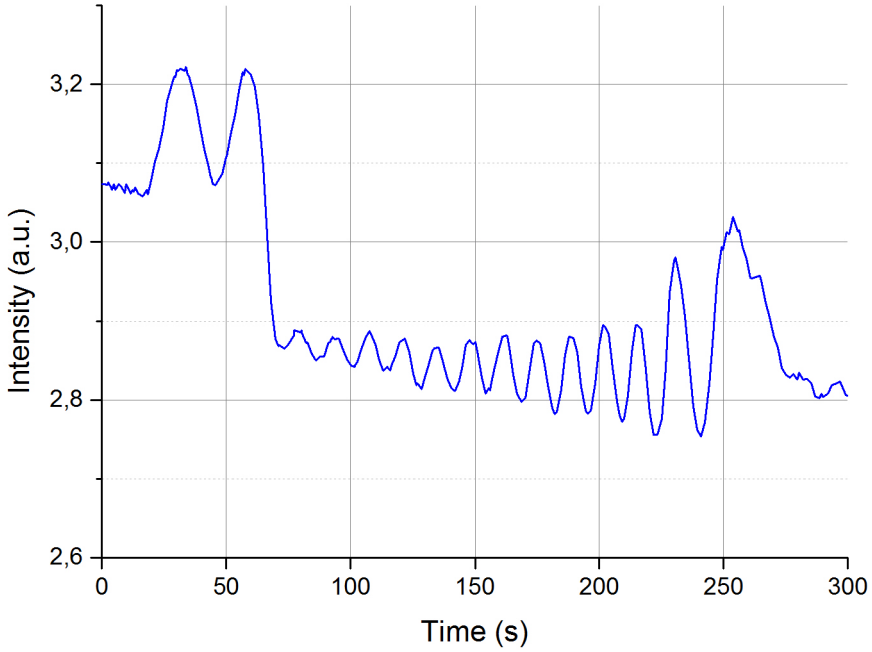

Figure 9.8: EPD reflection profile of the sample over time for a semiconductor etch past the quantum wells, obtained by recording the reflected power of a laser aimed at the surface of the sample

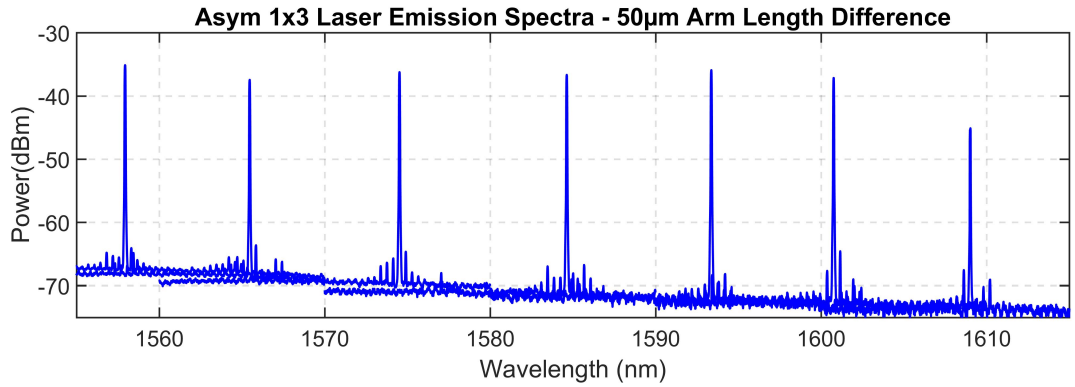

Figure 9.9: Emission spectra showing SMSR levels of up to 35dB and 51nm tuning range for a 1x3 MMI laser with pits - MCP variant

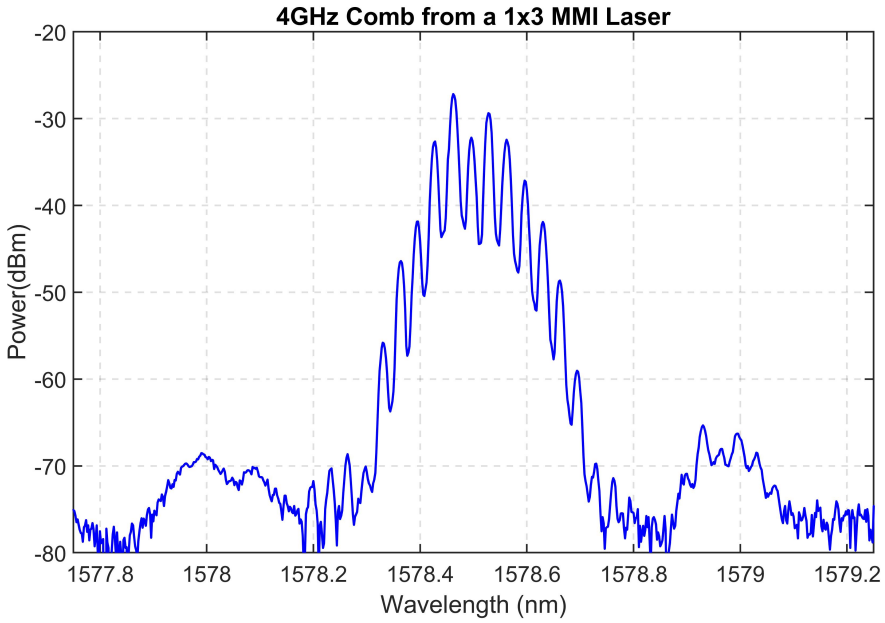

Figure 9.10: Detail of a 4GHz comb generated with a 1x3 MMI laser integrated with a gain-switched comb generation section

Fabry-Perot section was used, defined on the MMI laser side by a deeply etched reflective slot, and on the output side by the cleaved facet of the chip. A 4GHz 23dBm sinusoidal electrical signal, combined with a DC signal by the means of a bias tee, was applied to the gain-switched laser, following the procedure used in [54]. Combs such as that shown in Figure 9.10 were successfully generated and larger scans of the emission spectra (Figure 9.11) confirmed that the SMSR reached 30dB..

After confirming a single comb was achievable, the tuning of the laser was tested while the comb section was in operation. A discrete tuning range of 28nm was achieved, while maintaining SMSR levels of approximately 30dB. The superimposed combs from a 1x3 MMI laser and its integrated comb section can be seen in Figure 9.11. This set of measurements confirmed the successful monolithic integration of the 1x3 MMI laser design with a gain-switched section, forming a comb source of tunable wavelength, with SMSR levels of 30dB.

With the validation of the proposed design for monolithically integrated comb sources, the work was focused on the EML version. The static absorption of the EAM section was tested by applying a negative bias and recording the emission spectrum of the PIC. Static absorption levels of up to 19.5dB were recorded, as show in Figure 9.12. In addition to this, the tuning of the PIC was verified.

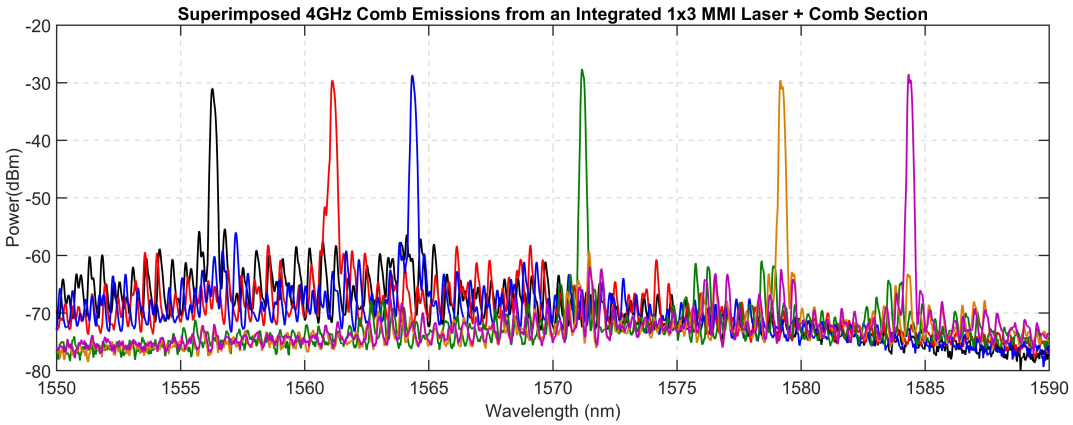

Figure 9.11: Emission spectra of a 4GHz comb source integrated with a 1x3 MMI tunable laser showing a 28nm discrete tuning range and SMSR levels from 25dB to above 30dB

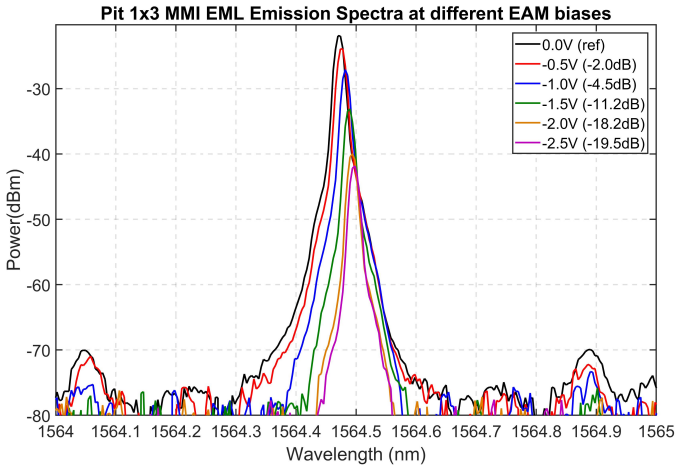

Figure 9.12: Laser emission spectra of a 1x3 MMI EML with pits, for different EAM biases showing a static absorption of up to 19.5dB at -2.5V bias

Figure 9.13 shows the superimposed emission spectra of a 1x3 MMI EML (MCP variant) at different wavelengths and EAM biases. While the scale of the plot is incompatible with the clear viewing of the absorption level, this specific device showed static absorption levels ranging from 6.4dB to 15.6dB for -2.5V biases, relatively to the peak emission power at the wavelength for a 0V EAM bias. This observation confirmed that the proposed 1x3 MMI laser geometry appears compatible with monolithic integration of an EAM section, forming a monolithic EML.

With the validation of both the comb source and the EML, the proposed 1x3 MMI laser geometry was confirmed as a valid candidate as a cleave-free light

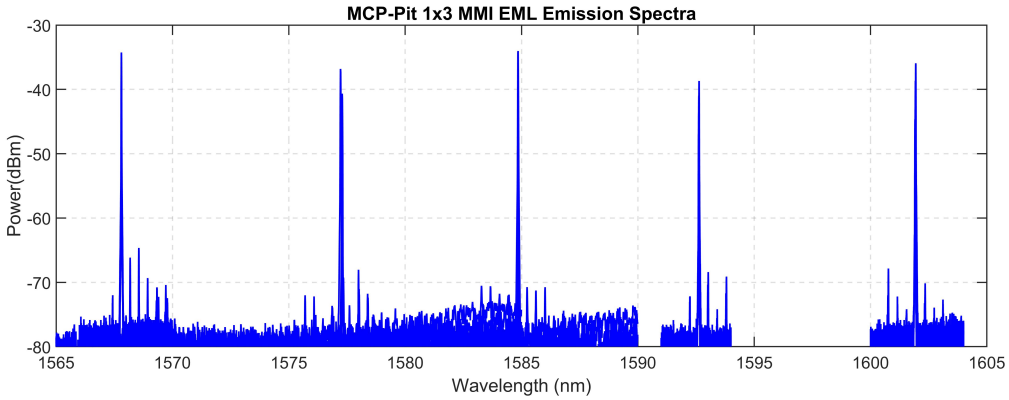

Figure 9.13: Laser emission spectra of a 1x3 MMI EML with pits for different wavelengths and EAM biases

source for the development of monolithically integrated PICs. The fabrication complexity was limited by the exclusive usage of UV lithography rather than advanced (and more expensive) lithography techniques such as e-beam or holographic lithography. With the absence of regrowth and of wet etch, the fabrication process of the proposed PICs was simplified with the aim of proposing an industry-friendly approach where the fabrication time and cost are reduced to make the process compatible with large-scale production.

Chapter 10

Conclusion and further works

10.1 Summary of the work done

Over the duration of this work, not only was a portfolio of lasers developed, but significant effort was put into improving the fabrication procedures. Within a set of fabrication constraints, the fabrication process itself was improved in several aspects. This was done while following an iterative design process leading to the design of a series of lasers. For the most promising design, the work was pushed further with the integration of the laser with additional components to form a monolithic PIC.

10.1.1 Simple fabrication methods

In order to pursue the goal of developing industry-friendly lasers, a number of constraints were applied to the fabrication procedure:

- the lithography was done using exclusively standard UV contact lithography rather than advanced methods such as e-beam or holographic lithography;
- the material used for this work was a regrowth-free epitaxial structure and no regrowth steps were used at any point of the process;
- cleaved facets could not be used for the laser, in order to ensure flexibility of the device and its positioning anywhere on the chip, instead of relying on a cleaved facet;

By using this set of constraints, the proposed structures would be easy to fabricate for time and cost reduction, and the facetless aspect would facilitate the development of complex PICs.

10.1.2 Improved fabrication practices

Lessons were learned from the difficulties encountered while fabricating the different generations of devices. The delicate step of oxide opening, where the alignment is critical led to the development of visual aids for early self-checking and correction of misalignment. Without adding any fabrication complexity, this visual aid made it possible to verify alignment immediately after lithography, while the previous method required the etching of the oxide layer. In case of misalignment, it was necessary to remove the oxide, deposit a fresh layer, and proceed with lithography again while with this aid, mistakes can be corrected before the oxide layer is etched, therefore reducing the number of steps to be repeated after observing a misalignment.

The fifth generation run and the multiple fabrication failures that occurred led to the development of the metal-first fabrication variant, where a thin layer of metal is evaporated before any other processing is performed on the wafer. Not only does this layer act as a protection that preserves the surface in pristine condition, but it also facilitates the spreading of the electrical current over the sections of waveguide, and reduces the risk of local overheating caused by spotty contact between the metal lines and the semiconductor. After some experimenting, a satisfying initial metal recipe was found, and workarounds were developed to accommodate the new constraints brought by this variant.

Finally, studying the abilities of the endpoint detection system for the semiconductor etch steps led to significant improvement of the precision for the etch depth. Initially, the monitoring was done a posteriori, making the semiconductor etch a succession of short etches separated by depth measurements. With the real-time monitoring, combined with the systematic a priori verification of the target instant for etch interruption, the etch depth precision was narrowed down to a 50nm uncertainty where it previously was several hundreds of nanometers.

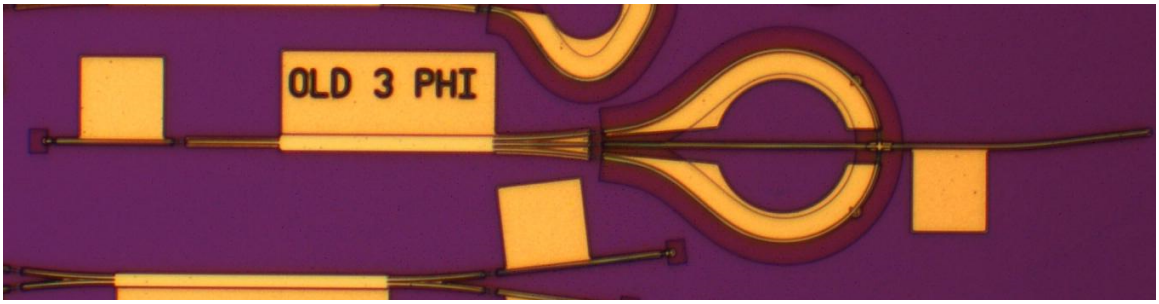

Figure 10.1: Microscope image of a "Phi" laser

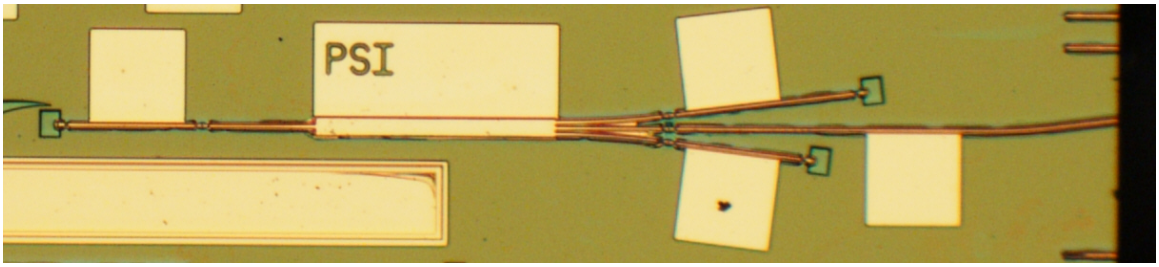

Figure 10.2: Microscope image of a 1x3 MMI Laser

10.1.3 Single-mode tunable facetless lasers

Through the iterative development process of MMI-based laser structures, a number of geometries were proposed. While some did not perform as well as expected, some geometries proved extremely encouraging, with discrete tuning ranges of tens of nanometers, fine tuning ranges of up to several nanometers around each main wavelength, while the SMSR levels reached the target of 30dB in use in the group. Among the studied geometries, two showed particularly encouraging performance. The looped 1x3 MMI "Phi" laser that can be seen in Figure 10.1 showed SMSR levels of up to 30dB and a tuning range of 36nm, from 1573nm to 1609nm. Another notable geometry, finalised at the third generation of devices, is the 1x3 MMI laser without loop, shown in Figure 10.2. This geometry showed a tuning range of 47nm, from 1564nm to 1611nm, and SMSR levels above 30dB.

For both these geometries, the reflective features when they were needed were not cleaved facets, but metal-coated etched facets achieving equivalent reflectivity while permitting the laser to be positioned anywhere on the chip, and not necessarily next to a cleaved facet.

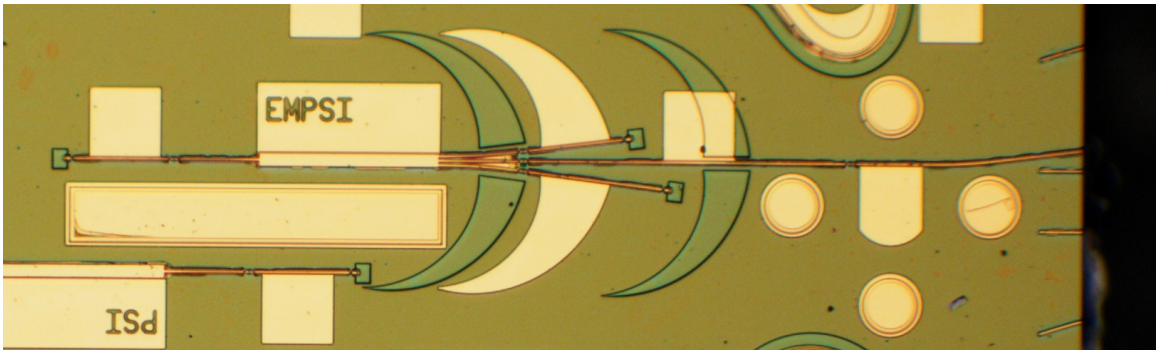

Figure 10.3: Microscope image of a 1x3 MMI Laser integrated with an EML section

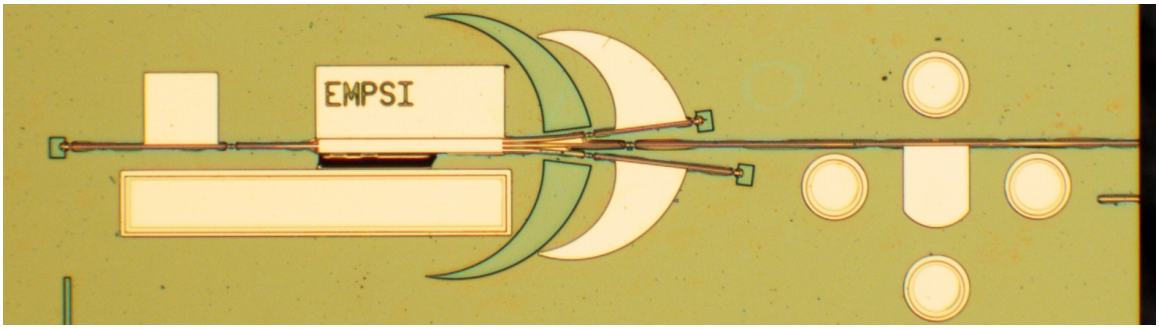

Figure 10.4: Microscope image of a 1x3 MMI laser integrated with a comb generation section

10.1.4 Integrated EMLs and comb sources

Of the different devices developed in this work, the most promising one was integrated with additional components to form EMLs and comb sources. Similarly to electronic integrated circuits, the entire structures were fabricated as one block and did not require any additional processing steps, keeping the fabrication complexity minimal. The resulting PICs, shown in Figures 10.3 and 10.4, were fabricated and tested. The generation of a tunable wavelength 4GHz comb was successful, and the tunable EML showed static absorption levels of up to 19.5dB for a -2.5V bias. These results confirmed the validity of the laser as a good candidate for the development of monolithically integrated PICs.

With the validation of this laser, the original goal of developing single-mode, tunable lasers compatible with monolithic integration and made without the need for advanced fabrication techniques, was reached.

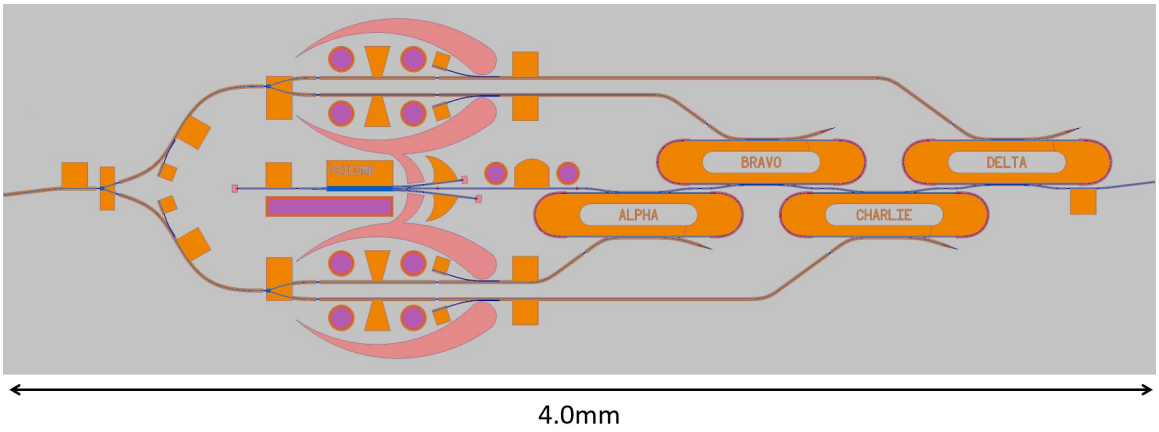

Figure 10.5: Schematic of a monolithically integrated regrowth-free photonic circuit including a tunable laser source, a comb generation section, and ring filters for 4 channels that are then equalised, modulated and recombined

10.2 Proposals for further development

In a short term perspective, the development of packaging-friendly structures based on the geometries developed in this work could be considered. This would allow for more detailed characterisation of the PIC performance, and the fine thermal control and isolation formed by the package could have a positive impact on the laser linewidth. Such a study could result in developing low-linewidth lasers compatible with advanced modulation formats. Another aspect that can be considered, is the study of epitaxial structures showing suitable performance for lasers and EAMs, leading to the development of tunable high-speed EMLs.

In a longer term perspective, the validation of the 1x3 MMI-based geometry as a good candidate for integration, and the proof of concept for comb sources and EMLs, suggest that further development of monolithic PICs can be considered. A potential approach could be the combining of the facetless tunable laser source with a comb generation section, followed by filters to extract different wavelengths from the comb. The separate signals could then be individually modulated and then recombined together, to form a coherent multi-channel transmission unit. A proposal for a 4-channel PIC combining this elements is shown in Figure 10.5 where a comb is generated, four lines are filtered, modulated and recombined, and photodiodes inspired by [55] are used in combination with amplifier sections to enable power equalisation between the channels. This next step in PIC complexity would come with its own challenges, especially

for the thermal management of such a highly complex structure, but other work done in the group on comb filtering shows encouraging results and the exploration of this direction can be considered for future development.

References

[1] Cisco, "The Zettabyte Era: Trends and Analysis," June 2017.

[2] H. Nyquist, "Certain Topics in Telegraph Transmission Theory," *Transactions of the A.I.E.E.*, pp. 617–644, Feb. 1928.

[3] "The History and Future of Internet Traffic." `https://blogs.cisco.com/sp/the-history-and-future-of-internet-traffic`. Accessed: 2019-03-28.

[4] L. Gasca, "From O to L: The Future of Optical-Wavelength Bands," June 2008.

[5] J. A. Jay, "An Overview of Macrobending and Microbending of Optical Fibers," *White Paper of Corning*, 2010.

[6] M. Smit, J. van der Tol, and M. Hill, "Moore's law in photonics," *Laser & Photonics Reviews*, vol. 6, no. 1, pp. 1–13, 2012.

[7] L. A. Coldren, S. W. Corzine, and M. L. Mašanović, *Diode Lasers and Photonic Integrated Circuits*. John Wiley & Sons, Inc., 2012.

[8] C. H. Henry, *Quantum Well Lasers*, ch. The Origin of Quantum Wells and the Quantum Well Laser, pp. 1–13. Academic Press, 1993.

[9] W. Tsang, R. Logan, L. Johnson, R. Hartman, and L. Koszi, "Strip Buried Heterostructure Lasers with Passive Distributed Bragg Reflectors," *IEEE Journal of Quantum Electronics*, vol. 15, pp. 1091–1093, October 1979.

[10] J. Johnson, L.-P. Ketelsen, D. Ackerman, L. Zhang, M. Hybertsen, K. Glogovsky, C. Lentz, W. Asous, C. Reynolds, J. Geary, K. Kamath, C. Ebert, M. Park, G. Przybylek, R. Leibenguth, S. Broutin, J. Stayt, J.W., K. Dreyer, L. Peticolas, R. Hartman, and T. Koch, "Fully Stabilized Electroabsorption-modulated Tunable DBR Laser Transmitter for Long-haul Optical Commu-

nications," *IEEE Journal of Selected Topics in Quantum Electronics*, vol. 7, pp. 168–177, Mar 2001.

[11] K. Utaka, K. Kobayashi, and Y. Suematsu, "Lasing Characteristics of 1.5 - 1.6 μm GaInAsP/InP Integrated Twin-guide Lasers with First-order Distributed Bragg Reflectors," *IEEE Journal of Quantum Electronics*, vol. 17, pp. 651–658, May 1981.

[12] N. Fujiwara, T. Kakitsuka, F. Kano, H. Okamoto, Y. Kawaguchi, Y. Kondo, Y. Yoshikuni, and Y. Tohmori, "Mode-hop-free Wavelength-tunable Distributed Bragg Reflector Laser," *Electronics Letters*, vol. 39, no. 7, p. 614, 2003.

[13] A. Ward, D. Robbins, G. Busico, E. Barton, L. Ponnampalam, J. Duck, N. Whitbread, P. Williams, D. Reid, A. Carter, and M. Wale, "Widely Tunable DS-DBR Laser with Monolithically Integrated SOA: Design and Performance," *IEEE Journal of Selected Topics in Quantum Electronics*, vol. 11, pp. 149–156, Jan 2005.

[14] L. Yu, D. Lu, L. Zhao, Y. Li, C. Ji, J. Pan, H. Zhu, and W. Wang, "Wavelength and Mode-Spacing Tunable Dual-Mode Distributed Bragg Reflector Laser," *IEEE Photonics Technology Letters*, vol. 25, no. 6, pp. 576–579, 2013.

[15] J. Buus, M. Amann, and D. Blumenthal, *Tunable Laser Diodes and Related Optical Sources*. Wiley-IEEE Press, 2005.

[16] J. Wang, J.-B. Tian, P.-F. Cai, B. Xiong, C.-Z. Sun, and Y. Luo, "1.55-μm AlGaInAs-InP Laterally Coupled Distributed Feedback Laser," *IEEE Photonics Technology Letters*, vol. 17, pp. 1372–1374, July 2005.

[17] S. J. Jang, C. I. Yeo, J. S. Yu, and Y. T. Lee, "1.55-μm DFB Lasers with Narrow Ridge Stripe and Second-Order Metal Surface Gratings by Holographic Lithography," *physica status solidi (a)*, vol. 207, no. 8, pp. 1982–1987, 2010.

[18] V. Jayaraman, Z.-M. Chuang, and L. Coldren, "Theory, Design, and Performance of Extended Tuning Range Semiconductor Lasers with Sampled Gratings," *IEEE Journal of Quantum Electronics*, vol. 29, pp. 1824–1834, Jun 1993.

[19] S. Lee, I. Jang, C. Wang, C. Pien, and T. Shih, "Monolithically Integrated Multiwavelength Sampled Grating DBR Lasers for Dense WDM Appli-

cations," *IEEE Journal of Selected Topics in Quantum Electronics*, vol. 6, pp. 197–206, Jan 2000.

[20] Y. Akulova, G. Fish, P.-C. Koh, C. Schow, P. Kozodoy, A. Dahl, S. Nakagawa, M. Larson, M. Mack, T. Strand, C. Coldren, E. Hegblom, S. Penniman, T. Wipiejewski, and L. Coldren, "Widely Tunable Electroabsorption-Modulated Sampled-Grating DBR Laser Transmitter," *IEEE Journal of Selected Topics in Quantum Electronics*, vol. 8, pp. 1349–1357, Nov 2002.

[21] I. Jang, S. Lee, C. Wang, L. Lai, W. Ho, and Y. Jan, "Realization and Performance of As-Fabricated SGDBR Multiwavelength Laser Arrays," *IEEE Photonics Technology Letters*, vol. 13, pp. 933–935, Sept 2001.

[22] C.-L. Yao, S.-L. Lee, I.-F. Jang, and W.-J. Ho, "Wavelength-Selectable Llasers with Bragg-Wavelength-Detuned Sampled Grating Reflectors," *Journal of Lightwave Technology*, vol. 24, pp. 3480–3489, Sept 2006.

[23] H. Wang, J. Zhao, and Y. Yu, "A Novel Tunable Semiconductor Laser Based on a Sampled Grating Reflector and an Interleaved Sampled Grating Reflector," in *Communications and Photonics Conference and Exhibition, 2011. ACP. Asia*, pp. 1–7, Nov 2011.

[24] M. Nakamura, H. W. Yen, A. Yariv, E. Garmire, S. Somekh, and H. L. Garvin, "Laser Oscillation in Epitaxial GaAs Waveguides with Corrugation Feedback," *Applied Physics Letters*, vol. 23, no. 5, pp. 224–225, 1973.

[25] D. Scifres, R. Burnham, and W. Streifer, "A Distributed Feedback Single Heterojunction Diode Laser," *IEEE Journal of Quantum Electronics*, vol. 10, pp. 790–791, September 1974.

[26] P. Vankwikelberge, G. Morthier, and R. Baets, "CLADISS - a Longitudinal Multimode Model for the Analysis of the Static, Dynamic, and Stochastic Behavior of Diode Lasers with Distributed Feedback," *IEEE Journal of Quantum Electronics*, vol. 26, pp. 1728–1741, Oct 1990.

[27] B. Pezeshki, E. Vail, J. Kubicky, G. Yoffe, S. Zou, J. Heanue, P. Epp, S. Rishton, D. Ton, B. Faraji, M. Emanuel, X. Hong, M. Sherback, V. Agrawal, C. Chipman, and T. Razazan, "20-mW Widely Tunable Laser Module Using DFB Array and MEMS Selection," *IEEE Photonics Technology Letters*, vol. 14, pp. 1457–1459, Oct 2002.

[28] L. Soldano and E. Pennings, "Optical Multi-Mode Interference Devices Based on Self-Imaging: Principles and Applications," *Journal of Lightwave Technology*, vol. 13, pp. 615–627, Apr 1995.

[29] K. Kudo, K. Yashiki, T. Sasaki, Y. Yokoyama, K. Hamamoto, T. Morimoto, and M. Yamaguchi, "1.55μm Wavelength-Selectable Microarray DFB-LD's with Monolithically Integrated MMI Combiner, SOA, and EA-Modulator," *IEEE Photonics Technology Letters*, vol. 12, pp. 242–244, March 2000.

[30] C. Zah, M. Amersfoort, B. Pathak, F. Favire, P. Lin, A. Rajhel, N. Andreadakis, R. Bhat, C. Caneau, and M. Koza, "Wavelength Accuracy and Output Power of Multiwavelength DFB Laser Arrays with Integrated Star Couplers and Optical Amplifiers," *IEEE Photonics Technology Letters*, vol. 8, pp. 864–866, July 1996.

[31] H. Ishii, K. Kasaya, H. Oohashi, Y. Shibata, H. Yasaka, and K. Okamoto, "Widely Wavelength-Tunable DFB Laser Array Integrated With Funnel Combiner," *Selected Topics in Quantum Electronics, IEEE Journal of*, vol. 13, pp. 1089–1094, Sept 2007.

[32] B. Corbett and D. McDonald, "Single Longitudinal Mode Ridge Waveguide 1.3 μm Fabry-Perot Laser by Modal Perturbation," *Electronics Letters*, vol. 31, pp. 2181–2182, Dec 1995.

[33] B. Corbett, C. Percival, and P. Lambkin, "Multiwavelength Array of Single-Frequency Stabilized Fabry-Perot Lasers," *Quantum Electronics, IEEE Journal of*, vol. 41, pp. 490–494, April 2005.

[34] R. Phelan, W. Guo, Q. Lu, D. Byrne, B. Roycroft, P. Lambkin, B. Corbett, and J. Donegan, "A Novel Two-Section Tunable Slotted Fabry-Perot Laser Exhibiting ns Wavelength Switching," *2007 9th International Conference on Transparent Optical Networks*, vol. 2, no. 1, pp. 124–127, 2007.

[35] K. Shi, F. Smyth, D. Reid, B. Roycroft, B. Corbett, F. H. Peters, and L. P. Barry, "Characterization of a Tunable Three-Section Slotted Fabry-Perot Laser for Advanced Modulation Format Optical Transmission," *Optics Communications*, vol. 284, no. 6, pp. 1616–1621, 2011.

[36] P. Ramaswamy, B. Roycroft, J. O'Callaghan, C. Janer, F. Peters, and B. Corbett, "Wavelength Agile Slotted Fabry-Perot Lasers," in *2014 International Semiconductor Laser Conference (ISLC)*, pp. 102–103, Sept 2014.

[37] S. O'Brien and E. P. O'Reilly, "Theory of Improved Spectral Purity in Index Patterned Fabry-Perot Lasers," *Applied Physics Letters*, vol. 86, no. 20, 2005.

[38] Q. Lu, W. Guo, R. Phelan, D. Byrne, J. Donegan, P. Lambkin, and B. Corbett, "Analysis of Slot Characteristics in Slotted Single-Mode Semiconductor Lasers Using the 2-D Scattering Matrix Method," *Photonics Technology Letters, IEEE*, vol. 18, pp. 2605–2607, Dec 2006.

[39] D. Byrne, Q. Lu, W. Guo, J. Donegan, B. Corbett, B. Roycroft, P. Lambkin, J. Engelstaedter, and F. Peters, "A Facetless Laser Suitable for Monolithic Integration," in *Conference on Lasers and Electro-Optics and Conference on Quantum Electronics and Laser Science 2008*, pp. 1–2, May 2008.

[40] D. Byrne, J. Engelstaedter, W.-H. Guo, Q. Y. Lu, B. Corbett, B. Roycroft, J. O'Callaghan, F. Peters, and J. Donegan, "Discretely Tunable Semiconductor Lasers Suitable for Photonic Integration," *IEEE Journal of Selected Topics in Quantum Electronics*, vol. 15, pp. 482–487, May 2009.

[41] B. Roycroft, J. O'Callaghan, K. Thomas, E. Pelucchi, F. Peters, and B. Corbett, "Facetless Tunable Lasers Coupled to Passive Waveguides," in *Lasers and Electro-Optics (CLEO), 2012 Conference on*, pp. 1–2, May 2012.

[42] M. Dernaika, L. Caro, N. P. Kelly, J. K. Alexander, F. Dubois, P. E. Morrissey, and F. H. Peters, "Deeply Etched Inner-Cavity Pit Reflector," *IEEE Photonics Journal*, vol. 9, pp. 1–8, Feb 2017.

[43] Y. H. Kwak and F. T. Anbari, "Benefits, Obstacles, and Future of Six Sigma Approach," *Technovation*, vol. 26, no. 5, pp. 708 – 715, 2006.

[44] F. T. O'Neill and J. T. Sheridan, "Photoresist Reflow Method of Microlens Production Part I: Background and Experiments," *Optik - International Journal for Light and Electron Optics*, vol. 113, no. 9, pp. 391 – 404, 2002.

[45] A. L. Schawlow and C. H. Townes, "Infrared and Optical Masers," *Phys. Rev.*, vol. 112, pp. 1940–1949, Dec 1958.

[46] C. Henry, "Theory of the linewidth of semiconductor lasers," *IEEE Journal of Quantum Electronics*, vol. 18, pp. 259–264, February 1982.

[47] H. Tsuchida, "Simple Technique for Improving the Resolution of the Delayed Self-Heterodyne Method," *Opt. Lett.*, vol. 15, pp. 640–642, Jun 1990.

[48] K. Cooney and F. H. Peters, "Analysis of Multimode Interferometers," *Opt. Express*, vol. 24, pp. 22481–22515, Oct 2016.

[49] E. Kleijn, M. Smit, and X. Leijtens, "Multimode Interference Reflectors: A New Class of Components for Photonic Integrated Circuits," *Journal of Lightwave Technology*, vol. 31, pp. 3055–3063, Sept 2013.

[50] H. Talbot, "Facts Relating to Optical Science," *The London, Edinburgh, and Dublin Philosophical Magazine and Journal of Science*, vol. 9, no. 56, pp. 401–407, 1836.

[51] J. T. Winthrop and C. R. Worthington, "Theory of Fresnel Images. I. Plane Periodic Objects in Monochromatic Light," *J. Opt. Soc. Am.*, vol. 55, pp. 373–381, Apr 1965.

[52] O. Bryngdahl, "Image Formation Using Self-Imaging Techniques," *J. Opt. Soc. Am.*, vol. 63, pp. 416–419, Apr 1973.

[53] "PixApp Presentation Webpage." `https://pixapp.eu/`. Accessed: 2018-08-10.

[54] J. K. Alexander, P. E. Morrissey, H. Yang, M. Yang, P. J. Marraccini, B. Corbett, and F. H. Peters, "Monolithically Integrated Low Linewidth Comb Source Using Gain Switched Slotted Fabry-Perot Lasers," *Opt. Express*, vol. 24, pp. 7960–7965, Apr 2016.

[55] A. Verdier, A. Garreau, K. Mekhazni, C. Gomez, H. Debregeas, H. Carrere, and R. Brenot, "Integrated Photodiodes for On-chip Semiconductor Optical Amplifier Gain Measurement," in *Conference on Lasers and Electro-Optics*, p. JW2A.55, Optical Society of America, 2018.

Appendix A

Epitaxial structure of the laser material used for this work

A.1 section

Figure A.1 shows the epitaxial structure used for all the devices presented in this work.

Layer	Material	Fraction (x)	Fraction (y)	Strain (%)	PL (nm)	Thickness (µm)	Dopant	Type	Doping (cm -3)
16	GaIn(x)As	0.530		0		0.2000	Zn	P	>1.50e19
15	GaIn(x)As(y)P	0.710	0.620	0	1300 +/- 50	0.0500	Zn	P	>3.00e18
14	InP					0.1000	Zn	P	>1.50e18
13	InP					1.5000	Zn	P	=1.00e18
12	GaIn(x)As(y)P	0.850	0.330	0	1100 +/- 20	0.0200	Zn	P	=1.00e18
11	InP					0.0500	Zn	P	=7.00e17
10	[Al(x)Ga]In(y)As	0.900	0.530	0		0.0600	Zn	P	=4.00e17
9	[Al(x)Ga]In(y)As	0.720 to 0.900	0.530	0		0.0600		U/D	
8	[Al(x)Ga]In(y)As	0.440	0.490	-0.3	1100 +/- 20	0.0100		U/D	
7*5	[Al(x)Ga]In(y)As	0.240	0.710	1.2	1530	0.0060		U/D	
6*5	[Al(x)Ga]In(y)As	0.440	0.490	-0.3	1100 +/- 20	0.0100		U/D	
5	[Al(x)Ga]In(y)As	0.900 to 0.720	0.530	0		0.0600		U/D	
4	[Al(x)Ga]In(y)As	0.900	0.530	0		0.0600	Si	N	=1.00e18
3	[Al(x)Ga]In(y)As	0.860 to 0.900	0.530	0		0.0100	Si	N	=1.00e18
2	InP					0.5000	Si	N	=1.00e18
1	InP					0.3000	Si	N	=3.00e18

Figure A.1: Epitaxial structure of the laser material used for this work